The behaviour of nitrogen during subduction of oceanic crust: insights from *in situ* SIMS analyses of high-pressure rocks

B.J.R. Harris[a,*], J.C.M. de Hoog[a], R. Halama[b]

[a] *Grant Institute, University of Edinburgh, James Hutton Road, Edinburgh, United Kingdom, EH9 3FE*
[b] *School of Geography, Geology and the Environment, Keele University, Keele, Staffordshire, United Kingdom, ST5 5BG*

[*] Corresponding author: b.j.r.harris@sms.ed.ac.uk

Abstract

Understanding the Earth's geological nitrogen (N) cycle requires an understanding of how N behaves during dehydration of subducted crust. We present the first *in situ* measurements of N in silicate minerals by secondary ion mass spectrometry, focusing on high pressure rocks representing subducted oceanic crust. We investigate the distribution of N between mineral phases, and combine analyses of N with other trace and major elements in order to constrain the behaviour of N during fluid-rock interaction. The data confirm that white mica (phengite, paragonite) is the primary host for N, containing up to 320 µg/g, whereas minerals including clinopyroxene, amphibole and epidote contain < 5 µg/g N. Chlorite can also contain N (up to 83 µg/g) and may play a previously unrecognised role in subduction zone N cycling. Bulk rock N concentrations estimated from mineral N concentrations and mineral modes are consistent with N concentrations measured by bulk combustion, which confirms that most N is hosted within silicate minerals and not along grain boundaries or in fluid inclusions. Bulk rock N contents correlate with K_2O ($N/K_2O = 19.3 \pm 2.0$). Using N/K_2O ratios and the average K_2O of altered oceanic crust, the flux of N subducted in oceanic crust is estimated to be $0.6 - 2.4 \times 10^{11}$ g/yr, which is consistent with but at the lower end of previous estimates. The data were also used to investigate the behaviour of N during fluid-rock interaction. Open system fluid-rock interaction modelling was used to model the evolution of N, B and Li contents during fluid-rock interaction in phengite from a garnet-phengite quartzite. By comparison to data for B and Li, the phengite-fluid partition coefficient for N was estimated to be 0.1–1.5. Separately, the growth of paragonite during fluid-rock interaction in a blueschist was shown to sequester N from phengite and limit bulk N loss to the fluid. The stability of white mica during fluid-rock interaction is therefore critical in controlling the behaviour of N. Nitrogen addition from sediment-derived fluids appears to be an important process in subduction zone rocks. Mafic crust can act as a sink for this N if white mica is stable. This work provides the first natural constraints on the fluid-mineral partitioning behaviour of N at subduction zone conditions and emphasises the complexity of N mobility within subduction zones, with redistribution between different phases and lithologies being important.

1. Introduction

The Earth's atmosphere is presently composed of 78% nitrogen and is essential for the habitability of the planet. There is considerable debate over the long-term evolution of the mass of N in the atmosphere (e.g. Mallik et al., 2018; Som et al., 2016; Wordsworth, 2016; Barry and Hilton, 2016; Busigny et al., 2011; Marty et al., 2013; Som et al., 2012; Berner, 2006; Avice et al., 2018) and it is therefore necessary to quantify the flux of N between the surface and deep-seated reservoirs, primarily the mantle. Subduction zones are the primary locations where N from the Earth's surface is returned to the mantle, and therefore studies which explore the behaviour of N during subduction are of importance to resolving the long-term N cycle. Previous studies of N in subduction-related rocks have focused on whole rock analyses, with a particular focus on N isotopic work (e.g. Epstein et al., 2021; Halama et al., 2010, 2014; Bebout et al., 2013; Busigny et al., 2011, 2003a; Halama et al., 2017). Suites of subducted metasediments have shown little N loss up to 90 km depth in cold subduction zones (Busigny et al., 2003a; Bebout et al., 2013), but substantial losses in warm subduction zones (Bebout and Fogel, 1992; Haendel et al., 1986; Mingram and Bräuer, 2001), with differing implications for the recycling of N over Earth's history. Basalts and gabbros representing oceanic crust (~1–30 µg/g N) have lower N contents than sediments (~100–2000 µg/g N) but the mass of subducted oceanic crust is an order of magnitude higher than of sediments. Considering average values for oceanic crust and sediment N concentrations, their contributions to the subducted N flux are comparable, although oceanic crust is less well constrained (Halama et al., 2010; Busigny et al., 2011; Li et al., 2007). Overall uncertainty in the global N recycling flux is on the order of 50–100% (Johnson and Goldblatt, 2015) due to the variable N contents of subducted lithologies and the lack of understanding of the processes controlling N recycling.

Nitrogen in rocks is primarily hosted as ammonium (NH_4^+), which substitutes for potassium and, to a lesser extent, sodium and calcium (Honma and Itihara, 1981). Micas are the dominant host of K in metasediments, and correlations between bulk K and N contents have been used to confirm that white micas are the main host for N (e.g. Bebout et al., 2013; Busigny et al., 2003a). High N contents of up to 1700 µg/g have been measured in micas from metasediments (Busigny et al., 2003b, 2004; Sadofsky and Bebout, 2000). For metabasic rocks that contain white mica,

correlated bulk N, Cs and Ba concentrations also suggested that N resides in the mica (Halama et al., 2010). However, a weak correlation of N with CaO + Na_2O in mica-free metabasic rocks may suggest that in these lithologies, N is hosted in Ca- and Na-bearing minerals (Busigny et al., 2011).

Nitrogen is regarded as a moderately fluid-mobile element. Several studies on rocks that have undergone extensive fluid-rock interaction have shown up to 60% loss of bulk N in metasomatised rocks compared to the country rock, in response to white mica dissolution or recrystallization during fluid-rock interaction (Halama et al., 2017; Epstein et al., 2021). Experimental data on fluid-mineral partition coefficients for N at subduction zone pressure-temperature conditions are sparse and values are not consistent between studies (Table 3, Pöter et al. (2004); Förster et al. (2019); Jackson et al. (2021); Li et al. (2015)). There is agreement between these studies that increasing pressure leads to NH_4^+ becoming more compatible in both phengite and biotite, compared to an aqueous fluid, because NH_4^+ is thermodynamically favoured over N_2 at higher pressures (Förster et al., 2019; Pöter et al., 2004; Jackson et al., 2021). The effect of temperature is smaller but increasing temperature leads to NH_4^+ becoming more compatible in phengite, compared to an aqueous fluid (Förster et al., 2019; Pöter et al., 2004). and less compatible in biotite (Förster et al., 2019; Jackson et al., 2021). The reasons for this are not fully understood. NH_4^+ is overall more compatible in biotite than muscovite over a wide range of P-T conditions, with values for $D_{NH_4^+}^{biotite-muscovite}$ from 1.5–4.2 (Sadofsky and Bebout, 2000; Busigny et al., 2004; Duit et al., 1986; Honma and Itihara, 1981; Pöter et al., 2004; Förster et al., 2019).

In situ data can provide new constraints on the partitioning of N between different minerals, reveal heterogeneities or zoning, and can be combined with thermodynamic and geochemical modelling to understand the behaviour of N during metamorphism and fluid-rock interaction. Previous *in situ* analyses of N contents were limited to a small number measurements of large white mica and biotite grains in metasediments by Fourier transform infrared spectroscopy with a 100 µm beam size (Busigny et al., 2003b,a, 2004). Few studies have compared N contents of minerals to other major or trace elements, or to textural features of the samples. *In situ* analyses of other fluid-mobile elements (e.g. B, F, Cl, LILE) in subduction-related samples have been successful in

constraining the inter-mineral partitioning behaviour of these elements, understanding their behaviour during metamorphic reactions and fluid-rock interaction, and constraining the amount of recycling of these elements into the mantle during subduction (e.g. Marschall et al., 2006; Urann et al., 2020; Halama et al., 2020; Debret et al., 2016; Bebout et al., 2007; De Hoog et al., 2014; Clarke et al., 2020). In this study we aim to: 1) explore the residency of N in different minerals in a suite of high pressure rocks representing formerly subducted oceanic crust; 2) combine *in situ* measurements of N concentrations with other trace and major elements to explore the behaviour of N during metamorphic fluid-rock interaction. Improved D values and mineral residency of N will allow more detailed modeling of N behaviour during subduction and eventually more accurate models of the long-term global N cycle in deep time.

2. Geological background and sample descriptions

2.1. Lago di Cignana, Italy

At Lago di Cignana, NW Italy, meta-ophiolites of the Zermatt-Saas Zone (ZSZ) are tectonically juxtaposed with a coesite- and diamond-bearing UHP metamorphic unit, the Lago di Cignana Unit (LCU) (Groppo et al., 2009). The LCU comprises eclogites, alongside metasediments including impure marbles and quartzites, and calcschists. Peak metamorphism of the LCU ocurred at ~600 °C, 2.7–3.2 GPa (Groppo et al., 2009; Reinecke, 1998), and was dated to 44 Ma by zircon U-Pb (Rubatto et al., 1998). The ZSZ comprises mantle serpentinites and eclogitic gabbros, which experienced a similar P-T-t history to the LCU (Groppo et al., 2009). REE patterns of eclogites from both the LCU and ZSZ indicate a MORB protolith (Halama et al., 2010; Dal Piaz et al., 1981).

The samples from Lago di Cignana have been described previously (Halama et al., 2020) but a brief description is reproduced here.

LC-3 is a garnet-phengite-quartzite (metachert) containing garnet, phengite and quartz as major phases, and accessory amphibole, biotite, rutile and opaques (Figure 1b). Garnet is euhedral, 100–500 μm in diameter and zoned, with Mn and Mg-enriched cores and Fe and Ca-enriched rims. Phengite occurs as 300–1500 μm flakes, which are preferentially aligned to define a weak foliation.

LC-1b is an eclogite containing garnet, omphacite, blue amphibole, epidote, paragonite and quartz. Paragonite occurs as needles, which are sometimes associated with rhombic pseudomorphs after lawsonite, formed during early retrograde decompression (Groppo et al., 2009).

LC-2a is a metagabbro. Omphacite, phengite, epidote, albite and chlorite are major phases, with accessory amphibole, titanite and rutile. This sample has been interpreted as showing pervasive retrogression into the greenschist-facies from a former high-pressure assemblage.

2.2. Raspas Complex, Ecuador

The Raspas Complex in southwest Ecuador exposes an high pressure terrane representing formerly subducted oceanic lithosphere (Arculus et al., 1999; Feininger, 1980). It includes eclogites and blueschists of the Raspas Formation, which occur alongside garnet-chloritoid-kyanite metapelites. All three lithologies record similar peak pressure-temperature conditions of 550–600 °C, 1.5–2 GPa (John et al., 2010; Gabriele et al., 2003). The age of metamorphism was dated to ~130 Ma, using Lu-Hf methods (John et al., 2010). Lithological differences between the blueschists and eclogites are ascribed to differences in bulk composition, with the blueschists being enriched in K_2O and Al_2O_3, and depleted in CaO, MgO and FeO. Geochemical analysis of the eclogites suggests that their protoliths were typical mid-ocean-ridge-basalts (MORB), with LREE-depleted REE patterns. Blueschists show LREE-enrichment, which has been interpreted as evidence of a seamount-type protolith (John et al., 2010).The samples from the Raspas Complex have not been described individually, but descriptions of each lithology are given in (John et al., 2010).

SEC16-1 is a blueschist containing garnet, Na-amphibole, phengite, paragonite, epidote, apatite, and calcium carbonate, with accessory chlorite (Figure 1a). Garnets (500–1500 μm) preserve an original euhedral outline but are sometimes corroded at the rims. A strong foliation is defined by preferential alignment of Na-amphibole, epidote, phengite and paragonite in the matrix. Epidote occurs also as elongate inclusions in garnet, which are aligned with the external foliation. Some apatite grains are elongate and aligned with the foliation. Chlorite occurs along fractures in garnet and at corroded rims.

SEC44-1 is an eclogite containing garnet, omphacite, phengite and quartz as major phases, and

accessory Na-amphibole, rutile and apatite. Subhedral to euhedral garnets (100–600 μm) cluster in garnet-rich (up to 50 %) layers up to 3 mm thick. The matrix consists of subhedral omphacite and rutile, randomly oriented phengite flakes, which are often rectangular, and interstitial quartz. Intergrowths of lobate quartz with Na-amphibole occur in low abundance, usually in proximity to garnet.

SEC47-1 is an eclogite containing garnet, omphacite, phengite, quartz, Na-amphibole and epidote as major phases, with accessory rutile (Figure 1c). Subhedral to euhedral garnet (50–400 μm) occurs in garnet-rich (up to 80 %) layers up to 4 mm thick. Preferential alignment of epidote, Na-amphibole, omphacite and phengite define a weak foliation, which is sub-parallel to the garnet layering. Quartz and rutile also occur in the matrix.

2.3. Jenner, California

Eclogite and blueschist blocks at Jenner, California, occur as part of the Franciscan Complex, a subducted-related melange complex in NW California. Samples were collected just north of the mouth of the Russian River about 1.5 km west of Jenner. These blocks occur loose on the beach, or within a sandstone-shale-rich matrix, which is interpreted a a recent landslide deposit (Raymond, 2017). The presence of Mg-rich metasomatic rinds, and geochemical signatures within the blocks, have been used to infer a former serpentinite melange host (Errico et al., 2013). Enrichment in large ion lithophile elements (LILE) and low ϵ_{Nd} and δ^7Li values in some blocks has been used to infer an additional sediment-derived fluid source (Sorensen et al., 1997; Penniston-Dorland et al., 2010). Peak metamorphic assemblages in eclogite and blueschist facies are identified in the least retrograded samples and record conditions of ~450–500 °C, 1–1.5 GPa (Krogh et al., 1994). Prograde to peak garnet growth was dated to c. 158 Ma using Lu-Hf methods (Anczkiewicz et al., 2004). Many samples are retrograded to a lower temperature assemblage (~400 °C, 1 GPa), along a counterclockwise P-T path, which is attributed to secular cooling of the subduction zone. Whole rock major element and immobile trace element compositions are similar to MORB (Penniston-Dorland et al., 2010; Sorensen et al., 1997).

JEN12-03 is a blueschist containing garnet, Na-amphibole, omphacite, phengite, titanite, chlo-

rite and quartz, with accessory iron oxides (Figure 1d). Three textural domains are identified. Rare omphacite-rich domains suggest a former eclogite facies assemblage. Large domains comprise a matrix of glaucophane, titanite, phengite, quartz and minor chlorite, with garnet occurring as porphyroblasts (up to 700 μm diameter). Garnets preserve an original euhedral outline but are corroded around the rims. A third domain is dominated by phengite flakes and fine grained chlorite. In all domains phengite occurs mostly as randomly oriented laths. Around 5 % of the phengite comprises rectangular to rhomboid grains, which are zoned in back scattered electron images.

JEN12-07 is a blueschist containing garnet, Na-amphibole, phengite, epidote and titanite, with accessory Fe-sulphides, apatite, quartz and chlorite. The matrix consists of aligned Na-amphibole, epidote, titanite and phengite, which define a foliation. Phengite also occurs as large (up to 500 µm) randomly oriented laths. Garnet occurs as 1–2.5 mm porphyroblasts with inclusions of Na-amphibole, epidote, titanite, quartz and chlorite, which preserve a foliation that is rotated relative to the external foliation.

JEN12-09 is an eclogite containing garnet, omphacite, phengite, epidote and titanite, with accessory chlorite, rutile, and quartz. The matrix consists of omphacite, phengite, epidote and titanite. Garnet occurs as 0.5–3 mm subhedral to euhedral porphyroblasts, containing inlcusions of omphacite, phengite, quartz and rutile. Chlorite occurs only on the rims of garnets. Phengite also occurs as up to 500 µm long grains in a 2 mm thick vein.

[Figure 1 about here.]

3. Analytical methods

3.1. Major element contents

Mineral compositions of some samples (see supplementary material) were determined using a Cameca SX100 electron microprobe equipped with 5 wavelength dispersive spectrometers (WDS) at the Department of Earth Sciences, University of Cambridge, UK. Acceleration voltage was 20 kV, beam current was 20 nA and beam diameter was 5 μm. On-peak counting times (seconds) for elements were as follows (background time in brackets): K 10 (5), Na 10 (5), Mg 30 (15), Si 10

(5), Al 30 (15), Fe 40 (20), Ca 20 (10), Ti 60 (30), Mn 90 (45). A variety of synthetic and natural standards were used for calibration and a PAP matrix correction was applied. Other samples were analysed using a JEOL JXA 8900R electron microprobe at the University of Kiel, Germany. Elements were measured 15 s on peak and 7 s on background with an acceleration voltage of 15 kV, beam current of 15 na and beam diameter of 5 μm. Natural standards were used for calibration and a CITZAF matrix correction was applied. EPMA spots were located as close as possible to the corresponding SIMS spots.

3.2. Nitrogen, volatile and trace element contents

Nitrogen contents of minerals were determined *in situ* by Secondary Ion Mass Spectroscopy (SIMS) at the Edinburgh Ion Microprobe Facility using a Cameca 7f-GEO with Hyperion source. Standard polished thin sections were cut to 25 mm rounds and gold-coated prior to loading into high vacuum (ca. 3×10^{-9} mbar). The sample surface was sputtered with a focused $^{16}O^-$ beam with a 18 nA beam current and an impact energy of 13.5 keV. Spot size was about 15 µm. One spot was analysed per grain, except where core and rim spots were analysed and reported separately. Prior to each analysis the analytical area was pre-sputtered for 120 s using a 15 µm beam raster to avoid background contamination. An effective field aperture of 20 µm was used to further reduce N backgrounds to <0.4 µg/g. Positive secondary ions sputtered from the sample were accelerated into a mass spectrometer and counted with an electron multiplier. An energy window of 50±20 V was applied to the secondary ion beam to reduce potential matrix effects. A mass resolution of 2000 (M/ΔM) was used to avoid interferences of $^{28}Si^{2+}$ and $^{12}CH_2{}^+$ on the $^{14}N^+$ signal, as well as $^7Li^{28}Si$ and $^{19}F^{16}O$ on ^{35}Cl. The mass calibration was updated at the start of each analysis using an automated peak centering routine on the ^{30}Si peak. The following isotopes were measured (total counting times per analysis in seconds in brackets): ^7Li (18), ^{11}B (30), $^{28}Si^{2+}$ (12), ^{14}N (60), ^{19}F (30), ^{26}Mg (12), ^{30}Si (12), ^{35}Cl (60). The ^{30}Si signal was used for internal standardisation using known SiO_2 contents measured by EPMA. As the wrong peak for ^{35}Cl was selected during the initial run, all analytical spots were repeated in a separate routine measuring ^{26}Mg, ^{30}Si and ^{35}Cl only, with other analytical parameters kept identical to the original run. Phengite mica 80-3

(71±19 µg/g N) and muscovite LMMN (186±11 µg/g N) were used for calibration of the N contents (Busigny et al., 2003b, 2004), St8.1.A9 basaltic glass for Cl (Lesne et al., 2011), Fba-5 basaltic glass for F (Guggino and Hervig, 2011), and GSD1-G basaltic glass for remaining elements (Jochum et al., 2005), the results of which are presented in the electronic supplement. ^{14}N count rates were low, equalling to a relative ion yield (RIY) compared to Si of ca. 0.002, which is why this element is not commonly measured, but signals were high enough to give acceptable counting statistics with the analytical conditions used. For example, for standard LMMN#2 (186 µg/g N), the ^{14}N count rate was ca. 35 count per second, for a total of 2100 counts for the whole analysis (60s for ^{14}N) and a standard deviation of 2.2% based on counting statistics. This is nearly identical to the 1s uncertainty based on the 6 repeat cycles for each analyses (internal precision), which was 2.4%, indicating that analytical uncertainty was dominated by counting statistics. Repeatability (external precision) of this standard was 4.3% (n=16, see Supplementary Table), so about double the internal precision, which is probably mostly related to slight heterogeneity of the standard and/or instrumental factors. 1s uncertainties presented in the figures is based on the propagated uncertainty of the measurements (internal precision) and the uncertainty of the slope of the calibration line (Figure 2). The measurement of molecular species such as ^{14}N^{16}O or ^{28}Si^{14}N was explored in the course of this study, but did not yield any advantage, as with the positive secondary ion beam used in our setup the yield of these species was lower than the ^{14}N signal. This contrasts results in negative ion mode, where an advantage was observed (Füri et al., 2018), resulting in lower detection limits, but considering our ^{14}N count rates were sufficient for the material under investigation, we preferred to be able to analyse other fluid-mobile elements at the same time as N. The two LMMN grains gave slightly different averages (187±22 and 153±7 µg/g, respectively, with n=20), the first grain containing areas with higher N contents (Figure 2). MgO contents (0.8 wt%) also showed about 10% variation, indicating some heterogeneity in this material (Figure 2). Multiple repeats of the Phe80-3 standard showed 13% variation (1s) in N content, which suggests some heterogeneity in this material as well, as it is much higher than the rsd for individual analyses (3%) and repeatibility of LMMN grain #2 (4%). Thus, the overall added uncertainty due to calibration uncertainty is ca. 15% Furthermore, we obtained a value of 17±0.4 µg/g N (n=2) on muscovite ms98973, for which no

N data has been published. Basaltic glasses GSD1-G and BCR2-G both showed concentrations of about 1.5±0.5 µg/g N, which is only slightly higher than what we measured for quartz (0.4 µg/g). As it is possible that these materials contain small amounts of N, no background correction was applied. Muscovite ms98973 (Dyar et al., 2001) was intended to be used as a secondary standard to detect potential matrix effects between basaltic glass and white mica, but we found that our concentrations for B (23-35 µg/g) and particularly Cl (31±13 µg/g) are very far from published values (180 and 700 µg/g, respectively; Dyar et al. (2001)), as well as highly heterogeneous. Fluorine was more homogeneous and our value of 12840 ± 45 µg/g is in reasonable agreement with the published value of 16800 µg/g Dyar et al. (2001). We also analysed two micas from Martin et al. (2015), namely JJE01-X-3 mica and MVE02-8-5 mica to evaluate their use as potential N standards. However, although N contents were high, unfortunately they were also extremely heterogeneous for N, Li and B (see electronic supplement).

[Figure 2 about here.]

4. Results

4.1. Major element mineral chemistry and N, B, Li concentrations in white mica

4.1.1. Lago di Cignana

Garnet-phengite quartzite sample LC-3 contains phengite with Si contents from 6.85–7.00 p.f.u. and Na/(Na+K) from 0.02–0.06 (Figure 3). There is a strong negative correlation between Si p.f.u. and Na/(Na+K). Nitrogen contents occupy a narrow range from 10–21 µg/g, whilst B contents vary widely (85–329 µg/g). Lithium contents vary from 39–62 µg/g. Despite the wide range in B contents, there is no clear trend in [N] versus [B]. Lithium contents show an overall negative correlation with [B], and positive correlation with [N] (Figure 7).

Metagabbro sample LC-2a contains two populations of phengite with different major element chemistry (Figure 3). Six grains had Si contents from 6.67–6.77 p.f.u. and Na/(Na+K) = 0.10-0.12. Two grains had higher Si contents (6.84–7.03) and Na/(Na+K) = 0.04–0.12. The low Si population

has [N] from 66–123 µg/g, [B] from 25-36 µg/g and [Li] from 55–64 µg/g. The high Si population has lower [N] (20–24 µg/g), higher [B] (48–49 µg/g) and lower [Li] (41–47 µg/g).

Eclogite sample LC-1b contains paragonite with a narrow range of Si contents (6.06–6.10 p.f.u.) and Na/(Na+K) = 0.94–0.97 (Figure 3). There is a negative correlation between Si p.f.u. and Na/(Na+K). Nitrogen contents vary from 15–47 µg/g, [B] from 13-24 µg/g and [Li] from 5-11 µg/g. There are no correlations between major and trace element concentrations.

4.1.2. Raspas

Eclogite sample SEC44-1 contains phengite with Si content ranging from 6.49–6.79 p.f.u., and Na/(Na+K) from 0.11–0.14 (Figure 3). Phengite grains are not zoned in major element chemistry. Nitrogen contents range from 147–244 µg/g and are not correlated with variations in major element chemistry. Boron contents range from 38–81 µg/g and Li contents from 19–48 µg/g. There is a positive correlation between [N] and [B] with average [N]/[B] ~3.2 (Figure 4).

Eclogite sample SEC47-1 contains phengite with a narrow range of Si contents from 6.51–6.60 p.f.u., and Na/(Na+K) from 0.12–0.15 (Figure 3). Phengite grains are not zoned in major element chemistry. Nitrogen contents range from 37–83 µg/g, so are considerably lower than in sample SEC44-1. Boron contents vary from 50–77 µg/g and Li contents from 38–49 µg/g. Phengite grains show no significant intra-grain variation in [Li], [B] or [N]. There are no correlations between major and trace element concentrations.

Blueschist sample SEC16-1 contains phengite as well as paragonite. Phengite has Si contents from 6.64–6.80 p.f.u. and Na/(Na+K) from 0.06–0.14 (Figure 3). There is a negative correlation between Si content and Na/(Na+K). Phengite grains are not zoned in major element chemistry. N contents range from 117–243 µg/g, B contents from 30–92 µg/g and Li contents from 31–43 µg/g. There is a positive correlation between Si p.f.u. and [N], and Si p.f.u. and [B], and a negative correlation between Si p.f.u. and [Li]. Paragonite has Si = 5.98–6.00 p.f.u. and Na/(Na+K) = 0.92–0.96. Paragonite N contents range from 31–78 µg/g, [B] from 112–139 µg/g, and [Li] from 24–28 µg/g. One exceptional grain has higher Si p.f.u. and lower Na/(Na+K) than other paragonites, with Si = 6.11 p.f.u. and Na/(Na+K) = 0.76, but unexceptional trace element contents. There are

no correlations between major and trace element concentrations in paragonite.

4.1.3. Jenner

Sample JEN12-03 contains phengite with a large range of Si contents from 6.61–7.00 p.f.u. Most grains have Na/(Na+K) from 0.01–0.03 and show no correlation between Na/(Na+K) and Si p.f.u. (Figure 3). Three low Si grains have much higher Na/(Na+K) from 0.09–0.11 and show a negative correlation between Na/(Na+K) and Si p.f.u.. Nitrogen contents range from 108–270 µg/g, [B] from 42–96 µg/g and [Li] from 13–33 µg/g. There are no correlations between trace and major element concentrations.

Sample JEN12-07 contains phengite with a large range of Si contents from 6.66–7.06 p.f.u. and Na/(Na+K) = 0.02–0.09 (Figure 3). There is a negative correlation between Si p.f.u. and Na/(Na+K). Nitrogen contents vary from 155–320 µg/g and are uncorrelated with Si p.f.u. Boron contents vary from 33–61 µg/g and [Li] from 6–38 µg/g. There is a positive correlation between [B] and [N] with average [N]/[B] ~4.5 (Figure 4).

Sample JEN12-09 contains phengite with a large range of Si contents from 6.50–6.88 p.f.u., Na/(Na+K) from 0.03–0.11, and a negative correlation between Si p.f.u. and Na/(Na+K) (Figure 3). Nitrogen contents vary from 22–127 µg/g, [B] from 29–64 µg/g, and [Li] from 16–42 µg/g. There are no correlations between trace and major element concentrations.

[Figure 3 about here.]

[Figure 4 about here.]

4.2. N, B, Li concentrations in other minerals

Clinopyroxene, amphibole, epidote, titanite and garnet contain <5 µg/g N and B in all samples (see supplementary data). Garnet, epidote and titanite also contain <5 µg/g Li. Clinopyroxene and amphibole are significant hosts of Li varying from 46–142 µg/g in clinopyroxene, and 6–71 µg/g in amphibole. The N content of chlorite is variable between different samples. Chlorite which occurs in cracks and on the rims of garnet contains no detectable N, K or Na (JEN12-07, JEN12-09, SEC16-1, LC-2a). Chlorite which occurs in the matrix of sample JEN12-03 contains 10-83 µg/g N

and minor amounts of K (up to 0.32 wt%) and Na (up to 0.13 wt%). Coexisting phengite contains 108–270 µg/g N. Chlorite in all samples contains <5 µg/g B, and 29–140 µg/g Li but neither varies systematically with textural setting like N.

4.3. Bulk nitrogen contents

Bulk N contents of each sample were calculated to assess the variability of N contents in different protoliths (Table 1). For each sample, we combine the mean N concentration in each N-bearing phase with the modal abundance of that phase, and use a weighted average to calculate the bulk N concentration. The standard errors on mean mineral N concentrations are larger than the analytical uncertainty for all samples except LC-3, which indicates that variation in N concentrations is due to heterogeneity between grains, rather than analytical uncertainty. Mineral modes were estimated by point counting 500 points on representative back scattered electron or optical photomicrographs of each sample, using the software JMicroVision. Absolute uncertainties on mineral modes are calculated as $\sqrt{x}/x$, where x is the number of points. Bulk N contents range from 1.2–71 µg/g. Standard errors on mineral modes and N concentrations were propagated to calculate the uncertainty in bulk N contents.

[Table 1 about here.]

5. Discussion

5.1. Residency of nitrogen and implications for global N recycling

Nitrogen typically occurs as NH_4^+ in crustal rocks, where it substitutes for K^+ in K-bearing minerals such as micas, and to a lesser extent for Na^+ and Ca^{2+} in minerals such as plagioclase (Honma and Itihara, 1981). White mica is the dominant K-bearing phase in most high pressure metabasaltic and metapelitic rocks up to ~9.5 GPa, 750–1000°C (Poli and Schmidt, 2002; Domanik and Holloway, 1996). Previous studies have used correlations between bulk K_2O and N contents to identify white micas as the main host for N (e.g. Bebout et al., 2013; Busigny et al., 2003a) in these rocks. Halama et al. (2010) reported bulk N concentrations for the three Raspas samples in

this study. These values are consistent with our estimated bulk concentrations based on mineral modes (Table 1), which confirms that most N is hosted within the analysed minerals and not along grain boundaries or in fluid inclusions. Most samples contain a single white mica phase (phengite or paragonite), which is the dominant N-bearing phase in the sample. Sample SEC16-1 contains coexisting phengite (117–243 µg/g N) and paragonite (31–118 µg/g N), where N is preferentially partitioned into phengite. This is consistent with the large ionic radius of NH_4^+ (1.67 Å), which is closer to that of K^+ (1.64 Å) than Na^+ (1.39 Å) (Shannon, 1976; Sidey, 2016), and with previous data on the nitrogen partitioning between Na- and K-bearing minerals (Honma and Itihara, 1981). Nitrogen content of white micas is uncorrelated with Na/(Na+K) in most samples, which suggests that small variations in white mica Na/(Na+K) ratio do not exert a strong control on N partitioning behaviour.

[Table 2 about here.]

Our data suggest that white mica hosts >90% of the total N in all but two samples (LC-1b and JEN12-03). Omphacite, glaucophane/barroisite and epidote contain <5 µg/g N in all samples. Omphacite and/or glaucophane are the next most significant N hosts after mica due to their large modal abundance in most samples. Calculated inter-mineral partition coefficients for B and Li (Table 2) are similar to previously published values (Marschall et al., 2006), which indicates that our values represent equilibrium partitioning and that our samples therefore can be used to investigate N partitioning. Partitioning values for N are variable between samples, due to the high N variability in phengite and the low N concentration in other minerals, but broadly indicate that N partitions strongly into phengite compared to other phases. Bulk K content controls white mica mode in metabasic rocks, and since N strongly partitions into white mica over other phases, the K content will exert a strong control on the N budget of subducted oceanic crust. Figure 5 shows that reconstructed bulk K and N contents for mafic samples fall on a positive trend, with average N (µg/g)/K_2O (wt%) = 19.3 ± 2.0. The metachert sample LC-3 plots as an outlier. N/K_2O for subducted mafic rocks is an order of magnitude lower than for metasedimentary rocks (N/K_2O ~200, Busigny et al. (2003a)). Our samples are representative of the basaltic upper oceanic crust, which

has undergone hydrothermal alteration on the seafloor and subsequently been subducted. Using N/K_2O we can estimate the flux of N subducted in upper oceanic crust from the K_2O content and the mass of crust subducted each year (2×10^{16} g/yr, Peacock (1990)). If we assume all basaltic crust has a MORB-like K_2O content (0.16 wt% K_2O, Gale et al. (2013)), we calculate a flux of $6.2 \pm 0.6 \times 10^{10}$ g/yr using our average N/K_2O value of 19.3 ± 2.0. For average altered oceanic crust (AOC, 0.62 wt% K_2O, Kelley et al. (2018)) we calculate $2.4 \pm 0.2 \times 10^{11}$ g/yr. Busigny et al. (2011) calculated a N flux of 1.3×10^{11} g/yr for upper oceanic crust, based on the average N content of metabasalts, which is similar to our value assuming AOC but larger than our value assuming MORB-like crust. All our estimates are somewhat smaller than the flux attributed to subducted sediments (7.4×10^{11} g/yr, Busigny et al. (2003a)).

[Figure 5 about here.]

The only non-mica mineral with significant N is chlorite, for which N contents vary with textural setting. Chlorite forming rims around garnet contains very low [N] (typically <5 µg/g). This is consistent with it forming from retrograde breakdown of garnet, which contains <1 µg/g N. Chlorite which occurs in the matrix alongside N-rich phengite contains 10-83 µg/g N (sample JEN12-03). Chlorite from JEN12-03 also contains minor amounts of K + Na (Figure 6). Incorporation of minor K and Na in chlorite crystals by interlayering of chlorite and K-bearing phyllosilicates at the nanometre scale has been investigated in diagenesis and sub-greenschist facies metamorphism of mudstones and volcaniclastic sediments (Lee et al., 1984; Ahn et al., 1988). It is possible that this mechanism is partially responsible for incorporation of K, Na and N in our chlorites, but N/K_2O is much higher in chlorite than in co-existing phengite (chl: 370, phe: 18), which suggests excess N in the chlorite structure itself. Chlorite is structurally similar to the K and Na-bearing micas, with both minerals containing large interlayer cation sites. In micas these are filled by K^+ and Na^+ cations, whereas in chlorite they are vacant. A possible substitution reaction for N incorporation into chlorite is $NH_3\,(\text{fluid}) + OH^- \longrightarrow {NH_4}^+ + {O^{2-}}$, where ${NH_4}^+$ is incorporated in the vacant interlayer sites.

[Figure 6 about here.]

Chlorite is common in greenschist facies rocks across a wide range of bulk compositions and therefore could potentially play an important role in subduction zone N cycling. However, it has received little previous attention as a possible host for N. Low-grade pelitic schists from the Erzgebirge massif displayed weak correlations between either chlorite or white mica mode and bulk N content, but a strong correlation between chlorite + white mica mode and bulk N content (Mingram and Bräuer, 2001), which supports chlorite being an important host for N. Chlorite also occurs in chlorite harzburgites, formed during serpentinite dehydration. Serpentinites typically have bulk N concentrations <5 µg/g (Halama et al., 2014; Philippot et al., 2007), but one chlorite harzburgite studied by Halama et al. (2014) has elevated N contents (~20 µg/g), which may be consistent with a role for chlorite as a host of N. More research is required to investigate the importance of chlorite as a host for N in different lithologies and the mechanism of N incorporation in chlorite.

5.2. Fluid rock interaction: a simple system

Sample LC-3 (Lago di Cignana garnet-phengite quartzite) was part of a previous study by Halama et al. (2020), who showed a strong positive correlation of B concentration and B isotopic composition, which was interpreted as resulting from addition of isotopically heavy B during peak metamorphic fluid-rock interaction with a serpentinite-derived fluid. We extend the fluid-rock interaction modelling approach of Halama et al. (2020) to include [Li] and [N] data and estimate the phengite-fluid partition coefficient for N. We modified the equation of Nabelek (1987) for open system fluid-rock interaction to replace the concentration of an element in the rock, with the concentration in phengite, multiplied by the modal abundance of phengite:

$$C^f_{phe} = DC_w - (DC_w - C^i_{phe})\ e^{-n/Dx_{phe}}$$

C^f_{phe} is the final concentration of the trace element in the phengite, C^i_{phe} is the initial concentration in the phengite, C_w is the concentration in the fluid, n is the fluid-rock ratio (by weight), x_{phe} is the modal abundance of phengite (33%), and D is the phengite-fluid partition coefficient. For B we use a partition coefficent of 0.7 (Marschall et al., 2006). We used an initial B concentration in the phengite of 50 µg/g and concentration in the fluid of 1000 µg/g, based on the preferred interpreta-

tion of addition of B from a serpentinite-derived, B-rich fluid (Halama et al., 2020). Marschall et al. (2006) reported a subsolidus partition coefficient for Li of 0.05, although higher values of 1 have been reported for suprasolidus experiments (Adam et al., 2014). We evaluate two different scenarios here to model the Li and B data and will subsequently use these constraints to model the combined [N]-[B] and [N]-[Li] data. For $D_{Li}^{phe-fl} = 0.05$, the [B]-[Li] data can be fitted using a Li concentration in the fluid of 800–1000 µg/g, and initial Li concentration in the phengite of 60–120 µg/g (Figure 7). For larger values of $D_{Li}^{phe-fl} = 0.5 - 1$, the [B]-[Li] data can be fitted with $[Li]_w = 0 - 20$ g/g and $[Li]_{phe}^{i} \approx 65$ g/g. Serpentinites typically contain <10 µg/g Li (Deschamps et al., 2012; Kodolányi et al., 2012; Lafay et al., 2013; Vils et al., 2008), and fluid inclusions representing serpentinite dehydration fluids also have <10 µg/g Li in both experiments and natural samples (Spandler et al., 2014; Scambelluri et al., 2004). Serpentinite-derived fluids are therefore expected to have low Li contents and the second scenario, with a value of $D_{Li}^{phe-fl} = 0.5 - 1$ is preferred. To model the [N]-[Li] data we therefore use $D_{Li}^{phe-fl} = 0.5$, $[Li]_w = 0$ g/g and $[Li]_{phe}^{i} = 65$ g/g, which allows the maximum range of D_{N}^{phe-fl} values that are consistent with the data.

To model the N data we consider a variety of theoretical scenarios and evaluate which are consistent with our data and independent constraints on fluid compositions. The [N]-[Li] data display a positive slope, which can be fitted with $[N]_w = 0$ g/g, $D_{N}^{phe-fl} = 0.5 - 1.5$ and $[N]_{phe}^{i} = 17 - 20$ g/g (Figure 7). These parameters also fit the [N]-[B] data. $D_{N}^{phe-fl} > 1.5$ is not consistent with the slope of the [N]-[Li] array for any range of other parameters. There is a trade-off between D and the concentration in the fluid, such that smaller values of D_{N}^{phe-fl} are consistent with the data if the fluid contains nitrogen (e.g. $D_{N}^{phe-fl} = 0.2$, $[N]_w = 50$ g/g). There are no data available on the N contents of fluids derived from serpentinite breakdown, but bulk serpentinites contain <15 µg/g N, and typically <5 µg/g N (Halama et al., 2014; Philippot et al., 2007). The major pulse of fluid release in serpentinites occurs during antigorite breakdown at 600–650 °C, which coincides with the P-T conditions inferred for fluid-rock interaction in this sample (Halama et al., 2020). The amount of fluid release is 6–13 wt%, depending on the serpentinite composition (Padrón-Navarta et al., 2013; Ulmer and Trommsdorff, 1995). Fluid release occurs over a narrow temperature interval so all fluid is likely to be pooled. Chlorite harzburgites produced from antigorite breakdown show a

similar range of N contents to serpentinites (Halama et al., 2014), which suggests that the amount of N released during antigorite breakdown is relatively small. Based on these constraints we suggest that N contents in serpentinite-derived fluids are likely <100 µg/g, and may be much lower. Using this N concentration in the fluid, a lower bound of $D_N^{phe-fl} = 0.1$ is the minimum value of D_N^{phe-fl} which is consistent with the [N]-[Li] and [N]-[B] data. For a lower value of 10 µg/g N in the fluid, the data are fit by $D_N^{phe-fl} = 0.3$.

With $D_N^{phe-fl} = 0.1 - 1.5$ all the data can be explained by fluid-rock ratios of up to 0.1, which is similar to the values of 0.1–0.13 obtained from B isotope modelling (Halama et al., 2020). Note these values have been rescaled from the Halama paper because the effect of the modal abundance of phengite on modifying the bulk rock equations was not accounted for. A value of $D_N^{phe-fl} = 0.1 - 1.5$ is therefore considered the most consistent with our data and fluid composition constraints.

[Figure 7 about here.]

The reconstructed bulk N content for this garnet-phengite quartzite (sample LC-3) is 5 µg/g (Table 1). Siliceous ooze and chert, which are considered the likely protoliths, contain 18–78 µg/g bulk N in samples from the Western Pacific (Sadofsky and Bebout, 2004). If these values are taken as representative then this suggests that N was lost during subduction, consistent with the conclusions from our fluid-rock interaction modelling.

Reported subsolidus values for D_N^{phe-fl} range from 0.01 to ~10, depending on the experimental conditions (Table 3). Pöter et al. (2004) reported $D_{NH_4^+}^{muscovite-fluid} \approx 0.13$ at 0.4 GPa and $D_{NH_4^+}^{mu-fl} \approx 0.20$ at 1.5 GPa in the temperature range 400–600 °C. More recent experiments have focused on the partitioning behaviour at higher temperatures, during melting, but have produced substantially differing results in different experimental bulk compositions. Förster et al. (2019) report $D_{NH_4^+}^{phengite-fluid} \approx 10$ at 2 GPa, 750 °C (subsolidus) and 0.5–1 at 3 GPa, 800–850 °C (suprasolidus) during reaction of a metapelitic melt with dunite. Jackson et al. (2021) report $D_{NH_4^+}^{biotite-fluid}$=0.01–0.4 at 0.2–2.3 GPa, 725–925 °C during reaction of silicate minerals with hydrous fluids. NH_4^+ has also previously been assumed to behave similarly to Rb^+ (e.g. Mallik et al., 2018; Busigny et al., 2003a), which has a similar ionic radius (NH_4^+: 1.67 Å, Rb^+: 1.72 Å), and a D_{Rb}^{phe-fl} value of ~4–10

(Adam et al., 2014; Melzer and Wunder, 2000).

Our value of $D_N^{phe-fl} = 0.1 - 1.5$ overlaps with the suprasolidus values of Förster et al. (2019). However, it is inconsistent with a single subsolidus value ($D_N^{phe-fl} = 10$) of Förster et al. (2019). and with the values of 4–10, based on the assumption that NH_4^+ behaves like Rb^+. Jackson et al. (2021) provide small values for $D_N^{biotite-fl}$ (0.01–0.4), which are mostly inconsistent with our value for D_N^{phe-fl}, when considering the consistent $D_N^{bi-phe} \approx 3$ reported by all studies. The subsolidus values of Pöter et al. (2004) ($D_N^{phe-fl} = 0.12 - -0.2$) fall at the bottom end of the range of values which are consistent with our data. The experimental data are either from similar temperatures but lower pressures to the Cignana case study (Pöter et al., 2004), or similar pressures but higher temperatures (Förster et al., 2019; Jackson et al., 2021). Extrapolation of the P-T effects reported by the Jackson study does not match our value for D_N^{phe-fl}, and therefore differences in P-T conditions are less likely to be the main factor for the discrepancy between our value and their work. Experimental and natural values for D_N^{phe-bi} are relatively consistent between multiple studies at different P-T conditions, whereas experimental values for D_N^{phe-fl} vary widely (Table 3), which suggests that variation may be a result of fluid-related factors. The difficulty of preserving N contents of experimental fluids during quenching may be a source of variation in the experimental results (e.g. Chen et al., 2019). Nitrogen is present as NH_4^+ in both biotite and phengite, whereas N speciation in fluid varies between N_2, NH_3 and NH_4^+, depending on P, T, pH and fO_2 (Mikhail and Sverjensky, 2014; Mikhail et al., 2017) and therefore differences in fluid pH and fO_2 between experiments, and between experiments and our samples, are also possible reasons for the discrepancy.

[Table 3 about here.]

5.3. Fluid-rock interaction: growth of new phases

Sample SEC16-1 (Raspas blueschist) contains phengite as well as paragonite. As both minerals are significant hosts for N and B, phengite compositions cannot be considered in isolation. Phengites show a decrease in [N] and [B] with decreasing Si p.f.u., an increase in [Li], as well as a increase in Na/(Na+K) (i.e. its paragonite component) whereas paragonite shows unsystematic variation in these elements (Figure 3).

We performed equilibrium phase diagram modelling in order to understand the mineralogical evolution of this sample and link this to the trace element behaviour. Calculations were performed using the Theriak-Domino software (de Capitani and Brown, 1987; de Capitani and Petrakakis, 2010) and the NCKFMASHTO + CO_2 system using an H_2O-CO_2 fluid in excess and the Holland and Powell (2011) thermodynamic database. The solution models used were: amphibole, clinopyroxene, white mica (Green et al., 2016); garnet, biotite, chlorite (White et al., 2014); epidote (Holland and Powell, 2011).

We calculated P-X(CO_2) and T-X(CO_2) equilibrium phase diagrams with variable X(CO_2) from 0 to 0.025, using the bulk composition for this sample reported in John et al. (2010) and an average MORB value of $X_{Fe^{3+}} = 0.16$ (Cottrell and Kelley, 2011). The effect of varying $X_{Fe^{3+}}$ from 0.05–0.25 moved field boundaries by only <1 kbar for all phases except epidote and therefore $X_{Fe^{3+}} = 0.16$ is considered suitable for this sample.

The observed assemblage occupies a field ranging from 1.5–1.9 GPa, 520–570 °C and X(CO_2) from 0.010–0.022 (Figure 8). This field is bounded by the disappearance of paragonite as X(CO_2) decreases, and the disappearance of garnet and epidote as X(CO_2) increases. John et al. (2010) previously calculated peak P-T conditions for the Raspas complex using conventional thermobarometry on garnet-omphacite-phengite assemblages. Peak P-T conditions of eclogites were 1.6–2.0 GPa and 550–650 °C. Garnet-omphacite-phengite domains in blueschists recorded slightly lower peak pressures of 1.4–1.6 GPa and similar temperatures. According to our modelling, omphacite is only stable under these conditions at lower values of X(CO_2) than are required to stabilise the observed blueschist assemblage, which has 16% paragonite. As mentioned above, the sample contains carbonate, and addition of CO_2 to the system stabilises paragonite. As X(CO_2) increases across the observed assemblage field, the paragonite mode increases from 0 to 25%, and glaucophane mode decreases from 40 to 15% due to the (unbalanced) reaction glaucophane + CO_2 $\longrightarrow$ paragonite + (Fe,Mg,Ca) carbonate. The high paragonite mode observed in the sample can therefore be explained as a result of infiltration of a carbonate-bearing fluid.

As X(CO_2) increases across the peak assemblage field, phengite Na/(Na+K) increases and Si content decreases. Phengite mode remains fairly constant, decreasing slightly from 16 to 14%. A

range of phengite Si contents are observed in different phengite grains. These are interpreted as representing partial recrystallisation of phengite during interaction with a carbonate-bearing fluid, with the new domains having lower Si p.f.u. and higher Na p.f.u.. Trace element redistribution from other phases into phengite supports our interpretation. For example, the Li contents in phengite, which correlate with decreasing Si p.f.u., can be interpreted to reflect incorporation of Li from glaucophane breakdown, since glaucophane has high Li contents (132–169 µg/g). Although the preservation of variable phengite Si contents implies that full equilibrium was not reached during fluid-rock interaction (i.e. the reactant phases were not totally consumed), the assemblage, major and trace element data support the conclusion that interaction with a CO_2-bearing fluid occurred, likely during early retrograde metamorphism.

[Figure 8 about here.]

Decrease in phengite N content in SEC16-1 also correlates with decreasing Si content and increasing Na/(Na+K). This can be explained by the phengite recrystallisation discussed above. During paragonite growth, partial re-equilibration of phengite with the growing paragonite results in transfer of N from phengite to paragonite. Taking the phengite with the highest Si content to represent the initial phengite composition prior to fluid-rock interaction, we use the N content of this phengite (232 µg/g) to calculate the initial bulk N concentration of the sample. To calculate the final bulk N concentration we use the average N concentrations of all phengite and paragonite grains measured (190 and 53 µg/g respectively). The observed phengite and paragonite modes are around 16%. Using the method described in Section 4.3 we calculate the bulk N contents before and after fluid-rock interaction. The final bulk N content is 39 µg/g. For the conservative assumption that the phengite mode does not change during fluid-rock interaction, the initial bulk N is 37 µg/g. Accounting for the modelled decrease in phengite mode from 16 to 14%, the initial bulk is 42 µg/g. The decrease in N concentration seen in phengite in this sample can therefore be explained by redistribution of N between growing and dissolving phases during fluid-rock interaction, without any significant external input or loss of N from the rock. The uncertainty on the bulk [N] values was estimated to be ~15–20% by combining uncertainties on the mineral N concentrations and

mineral modes. This conclusion is similar to Halama et al. (2017), who showed that the retention of N during fluid-rock interaction is strongly controlled by the stability or breakdown of white mica. A similar reaction (albite + CO_2 $\longrightarrow$ paragonite + aragonite) observed in calcschists from the Western Alps was associated with 60% loss of N from the bulk rock, with volumetric fluid-rock ratios of 3–4 (Epstein et al., 2021). The difference in N behaviour compared to our study may be explained by a lower fluid-rock ratio, or a different fluid composition. If we assume that the $X(CO_2)$ values which stabilise the observed assemblage (Figure 8) are representative of the fluid, and that all the CO_2 in the fluid was converted to carbonate minerals, we can estimate the minimum amount of fluid required to generate the modal abundance of carbonate observed. Using $X(CO_2)$=0.01–0.022 and a carbonate mode of 3–5 vol% gives a fluid-rock ratio of 0.2–0.9, which is indeed lower than for the Epstein study.

Phengite and paragonite are also the main B-bearing phases, so the same model can be applied to B as with N. The decrease in B contents with decreasing Si contents can be explained by redistribution of B into paragonite. The calculated final bulk B concentration is 28 µg/g, compared to an initial concentration of 15-17 µg/g depending on the estimate of the phengite mode. This suggests that in contrast with N, B has been added to the rock during fluid-rock interaction. This may explain why there is more scatter in the correlation of [B] with Si p.f.u., compared to [N], as individual grains have equilibrated to differing degrees with a B-rich fluid (Konrad-Schmolke and Halama, 2014; Halama et al., 2020).

5.4. Fluid-rock interaction in other samples

Calculated bulk N concentrations in Cignana mafic rocks (samples LC-2a, LC-1b) are very low. Sample LC-1b (1.2 µg/g N) falls within the range of N contents observed in fresh MORB, which is generally <2 µg/g (Li et al., 2007; Busigny et al., 2005; Erzinger et al., 1996). Sample LC-2a has slightly higher N contents (3.6 µg/g), which may reflect a more hydrothermally altered protolith (Busigny et al., 2005; Li et al., 2007), or addition of minor N during subduction.

Sample LC-2a preserves variability in phengite major and trace element chemistry. The main population has constant Si p.f.u. but variable N contents (39–123 µg/g). There are two grains with

higher, variable Si content, lower N (20–24 µg/g) and Li contents, and higher B content. The Si contents of these grains overlap with those from sample LC-3, which were interpreted to record peak metamorphism. Halama et al. (2020) previously interpreted B isotope data from LC-2a to suggest that B was lost during retrograde fluid-rock interaction. The observed lower B contents and lower Si contents in our analyses are consistent with this interpretation, where the low Si grains formed during retrograde recrystallization and the high Si grains preserve peak conditions. The elevated N and Li contents in low Si grains suggest that small amounts of N and Li were added during retrograde fluid-rock interaction.

Previous studies on eclogites and blueschists from Jenner have suggested a complex metamorphic history involving interaction with both sediment-derived (Sorensen et al., 1997; Penniston-Dorland et al., 2010) and serpentinite-derived fluids (Errico et al., 2013). Jenner samples show high bulk N contents (13–71 µg/g) compared to the range of both fresh MORB (< 2 µg/g) and altered oceanic crust (1–30 µg/g, Li et al. (2007); Busigny et al. (2005)). The N concentrations in individual phengite grains are similar to those from Raspas, but the Jenner samples contain higher phengite modes, resulting in higher bulk N contents. High phengite mode is consistent with the bulk enrichment in K and other large ion lithophile elements documented by Sorensen et al. (1997) and attributed to interaction with a sediment-derived fluid. High N contents are also consistent with a sediment-derived fluid, since subducted sediments can have N contents up to 2000 µg/g (e.g. Sadofsky and Bebout, 2004; Li and Bebout, 2005). The positive correlation of N and B contents in phengite in samples JEN12-03 and JEN12-07 is also consistent with a sediment derived fluid, since sediments can also contain high B contents (e.g. Romer et al., 2014; Bebout et al., 2013; De Hoog and Savov, 2018). Negative correlation of [N] and [Li] in JEN12-07 and JEN12-09 suggests that these sediment-derived fluids may be Li-poor.

These samples demonstrate that addition of N during metamorphism appears to be a common process in subduction-related mafic rocks, in agreement with recent work which found that N addition can occur as early as blueschist facies (Li et al., 2021). These fluids are most likely sourced from dehydrating metasediments, as these are rich in N. Addition of N can be associated with either addition or loss of Li and B, which suggests that these fluids can be heterogeneous in their Li and

B contents, possibly reflecting heterogeneity in the sediments themselves. Addition of N is seen in phengite with high Si contents, which implies that it occurred during deep subduction and is not a late-stage retrograde overprint. The presence of N and other fluid-mobile elements in sediment-derived fluids at depths of up to ~90 km (in the case of Cignana, see our modelling in Section 5.2) implies that these elements are at least partially retained to that depth, and can be mobilised and redistributed there, rather than being completely lost during shallow dehydration reactions. This emphasises the importance of understanding volatile element transfer between lithologies during subduction, not just the effects of prograde devolatilisation, and shows that mafic rocks may act as sinks for N and other volatiles during subduction-related metasomatism, if accompanied by growth of mica.

6. Conclusions

This study demonstrates the viability of *in situ* analyses of N in silicate minerals using SIMS. The data collected from a range of formerly subducted rocks show that N is dominantly hosted in white micas, compared to phases such as omphacite or Na-amphibole. Chlorite may have an additional role as a N host but more data are required to explore its role in a wider variety of localities and lithologies. Reconstructed bulk N contents based on mineral modes and N concentrations agree with bulk N contents measured by combustion, which confirms that most N is hosted in the major rock-forming minerals. Using the N/K_2O ratio in white micas, and the K-content of the subducted slab, we estimate the subducted flux of N in oceanic crust to be $0.6 - 2.4 \times 10^{11}$ g/yr, which is similar to or slightly smaller than previous estimates. A case study of fluid-rock interaction in a mineralogically simple garnet-phengite quartzite shows moderate N loss during fluid-rock interaction. Using open system fluid-rock interaction equations we show that N is a moderately fluid-mobile element under the P-T-X conditions experienced by this sample ($D_N^{phe-fl} = 0.1 - 1.5$). A second fluid-rock interaction case study shows the importance of white mica stability in controlling the N budget of rocks. White mica growth during fluid-rock interaction can sequester N and prevent significant bulk N loss. Our work provides constraints on the inter-mineral partitioning of N at subduction zone conditions and provides the first natural constraints on the fluid-mineral

partitioning of N at these conditions. We emphasise the complexity of element mobility within subduction zones, with redistribution between different phases and lithologies being important, in addition to simple loss of volatiles during dehydration.

7. Acknowledgements

We thank M. Konrad-Schmolke for expert guidance at Jenner, T. John for assistance with Raspas samples, D. Wilde for help with sample preparation and I. Buisman for electron probe analyses. We also thank S. Mikhail, L. Li and an anonymous reviewer for comments which improved this manuscript. This work was supported by a NERC Doctoral Training Partnership grant (NE/S007407/1) and a NERC Ion Microprobe Facility grant (IMF709/0520).

References

Adam, J., Locmelis, M., Afonso, J.C., Rushmer, T., Fiorentini, M.L., 2014. The capacity of hydrous fluids to transport and fractionate incompatible elements and metals within the Earth's mantle. Geochemistry, Geophysics, Geosystems 15, 2241–2253. doi:https://doi.org/10.1002/2013GC005199.

Ahn, J.H., Peacor, D.R., Coombs, D.S., 1988. Formation mechanisms of illite, chlorite and mixed-layer illite-chlorite in Triassic volcanogenic sediments from the Southland Syncline, New Zealand. Contributions to Mineralogy and Petrology 99, 82–89. doi:10.1007/BF00399368.

Anczkiewicz, R., Platt, J.P., Thirlwall, M.F., Wakabayashi, J., 2004. Franciscan subduction off to a slow start: evidence from high-precision Lu–Hf garnet ages on high grade-blocks. Earth and Planetary Science Letters 225, 147–161. doi:10.1016/j.epsl.2004.06.003.

Arculus, R.J., Lapierre, H., Jaillard, , 1999. Geochemical window into subduction and accretion processes: Raspas metamorphic complex, Ecuador. Geology 27, 547–550. doi:10.1130/0091-7613(1999)027<0547:GWISAA>2.3.CO;2.

675 Avice, G., Marty, B., Burgess, R., Hofmann, A., Philippot, P., Zahnle, K., Zakharov, D., 2018.
676 Evolution of atmospheric xenon and other noble gases inferred from Archean to Paleoproterozoic
677 rocks. Geochimica et Cosmochimica Acta 232, 82–100. doi:10.1016/j.gca.2018.04.018.

678 Barry, P., Hilton, D.R., 2016. Release of subducted sedimentary nitrogen throughout Earth's
679 mantle. Geochemical Perspectives Letters 2.

680 Bebout, G.E., Agard, P., Kobayashi, K., Moriguti, T., Nakamura, E., 2013. Devolatilization history
681 and trace element mobility in deeply subducted sedimentary rocks: Evidence from Western Alps
682 HP/UHP suites. Chemical Geology 342, 1–20. doi:10.1016/j.chemgeo.2013.01.009.

683 Bebout, G.E., Bebout, A.E., Graham, C.M., 2007. Cycling of B, Li, and LILE (K, Cs, Rb, Ba, Sr)
684 into subduction zones: SIMS evidence from micas in high-P/T metasedimentary rocks. Chemical
685 Geology 239, 284–304. doi:10.1016/j.chemgeo.2006.10.016.

686 Bebout, G.E., Fogel, M.L., 1992. Nitrogen-isotope compositions of metasedimentary rocks in the
687 Catalina Schist, California: Implications for metamorphic devolatilization history. Geochimica
688 et Cosmochimica Acta 56, 2839–2849. doi:10.1016/0016-7037(92)90363-N.

689 Berner, R.A., 2006. Geological nitrogen cycle and atmospheric N2 over Phanerozoic time. Geology
690 34, 413–415. doi:10.1130/G22470.1.

691 Busigny, V., Cartigny, P., Philippot, P., 2011. Nitrogen isotopes in ophiolitic metagabbros: A
692 re-evaluation of modern nitrogen fluxes in subduction zones and implication for the early Earth
693 atmosphere. Geochimica et Cosmochimica Acta 75, 7502–7521. doi:10.1016/j.gca.2011.09.
694 049.

695 Busigny, V., Cartigny, P., Philippot, P., Ader, M., Javoy, M., 2003a. Massive recycling of nitrogen
696 and other fluid-mobile elements (K, Rb, Cs, H) in a cold slab environment: evidence from HP to
697 UHP oceanic metasediments of the Schistes Lustrés nappe (western Alps, Europe). Earth and
698 Planetary Science Letters 215, 27–42. doi:10.1016/S0012-821X(03)00453-9.

699 Busigny, V., Cartigny, P., Philippot, P., Javoy, M., 2003b. Ammonium quantification in muscovite
700 by infrared spectroscopy. Chemical Geology 198, 21–31. doi:10.1016/S0009-2541(02)00420-5.

701 Busigny, V., Cartigny, P., Philippot, P., Javoy, M., 2004. Quantitative analysis of ammonium
702 in biotite using infrared spectroscopy. American Mineralogist 89, 1625–1630. doi:10.2138/
703 am-2004-11-1206.

704 Busigny, V., Laverne, C., Bonifacie, M., 2005. Nitrogen content and isotopic composition of oceanic
705 crust at a superfast spreading ridge: A profile in altered basalts from ODP Site 1256, Leg 206.
706 Geochemistry, Geophysics, Geosystems 6. doi:https://doi.org/10.1029/2005GC001020.

707 de Capitani, C., Brown, T.H., 1987. The computation of chemical equilibrium in complex systems
708 containing non-ideal solutions. Geochimica et Cosmochimica Acta 51, 2639–2652. doi:10.1016/
709 0016-7037(87)90145-1.

710 de Capitani, C., Petrakakis, K., 2010. The computation of equilibrium assemblage diagrams with
711 Theriak/Domino software. American Mineralogist 95, 1006–1016. doi:10.2138/am.2010.3354.

712 Chen, Q., Zhang, Z., Wang, Z., Li, W.C., Gao, X.Y., Ni, H., 2019. In situ Raman spectroscopic
713 study of nitrogen speciation in aqueous fluids under pressure. Chemical Geology 506, 51–57.
714 doi:10.1016/j.chemgeo.2018.12.016.

715 Clarke, E., De Hoog, J.C.M., Kirstein, L., Harvey, J., Debret, B., 2020. Metamorphic olivine records
716 external fluid infiltration during serpentinite dehydration. Geochemical Perspectives Letters 16,
717 25–29. doi:10.7185/geochemlet.2039.

718 Cottrell, E., Kelley, K.A., 2011. The oxidation state of Fe in MORB glasses and the oxygen fugacity
719 of the upper mantle. Earth and Planetary Science Letters 305, 270–282. doi:10.1016/j.epsl.
720 2011.03.014.

721 Dal Piaz, G.V., Venturelli, G., Spadea, P., Di Battistini, G., 1981. Geochemical features of
722 metabasalts and metagabbros from the Piemonte ophiolite nappe, Italian Western Alps. Geo-

chemical features of metabasalts and metagabbros from the Piemonte ophiolite nappe, Italian Western Alps 142, 248–269.

De Hoog, J.C.M., Hattori, K., Jung, H., 2014. Titanium- and water-rich metamorphic olivine in high-pressure serpentinites from the Voltri Massif (Ligurian Alps, Italy): evidence for deep subduction of high-field strength and fluid-mobile elements. Contributions to Mineralogy and Petrology 167. doi:10.1007/s00410-014-0990-x.

De Hoog, J.C.M., Savov, I.P., 2018. Boron Isotopes as a Tracer of Subduction Zone Processes, in: Marschall, H., Foster, G. (Eds.), Boron Isotopes: The Fifth Element, Cham. Advances in Isotope Geochemistry, pp. 217–247. doi:10.1007/978-3-319-64666-4_9.

Debret, B., Koga, K.T., Cattani, F., Nicollet, C., Van den Bleeken, G., Schwartz, S., 2016. Volatile (Li, B, F and Cl) mobility during amphibole breakdown in subduction zones. Lithos 244, 165–181. doi:10.1016/j.lithos.2015.12.004.

Deschamps, F., Godard, M., Guillot, S., Chauvel, C., Andreani, M., Hattori, K., Wunder, B., France, L., 2012. Behavior of fluid-mobile elements in serpentines from abyssal to subduction environments: Examples from Cuba and Dominican Republic. Chemical Geology 312-313, 93–117. doi:10.1016/j.chemgeo.2012.04.009.

Domanik, K.J., Holloway, J.R., 1996. The stability and composition of phengitic muscovite and associated phases from 5.5 to 11 GPa: Implications for deeply subducted sediments. Geochimica et Cosmochimica Acta 60, 4133–4150. doi:10.1016/S0016-7037(96)00241-4.

Duit, W., Jansen, J.B.H., Breemen, A.v., Bos, A., 1986. Ammonium micas in metamorphic rocks as exemplified by Dome de l'Agout (France). American Journal of Science 286, 702–732. doi:10.2475/ajs.286.9.702.

Dyar, M.D., Wiedenbeck, M., Robertson, D., Cross, L.R., Delaney, J.S., Ferguson, K., Francis, C.A., Grew, E.S., Guidotti, C.V., Hervig, R.L., Hughes, J.M., Husler, J., Leeman, W., McGuire, A.V., Rhede, D., Rothe, H., Paul, R.L., Richards, I., Yates, M., 2001. Reference Minerals for

748 the Microanalysis of Light Elements. Geostandards Newsletter 25, 441–463. doi:10.1111/j.
749 1751-908X.2001.tb00616.x.

750 Epstein, G.S., Bebout, G.E., Angiboust, S., 2021. Fluid and mass transfer along transient sub-
751 duction interfaces in a deep paleo-accretionary wedge (Western Alps). Chemical Geology 559,
752 119920. doi:10.1016/j.chemgeo.2020.119920.

753 Errico, J., Barnes, J., Strickland, A., Valley, J., 2013. Oxygen isotope zoning in garnets from
754 Franciscan eclogite blocks: evidence for rock-buffered fluid interaction in the mantle wedge.
755 Contributions to Mineralogy & Petrology 166, 1161–1176. doi:10.1007/s00410-013-0915-0.

756 Erzinger, J., Bach, W., Alt, J.C., Kinoshita, H., Stokking, L.B., Michael, P.J., 1996. Downhole
757 variation of molecular nitrogen in DSDP/ODP Hole 504B: preliminary results. Proceedings of the
758 Ocean Drilling Program : Scientific Results 148, 3–8. doi:10.2973/odp.proc.sr.148.156.1996.

759 Feininger, T., 1980. Eclogite and Related High-Pressure Regional Metamorphic Rocks from the
760 Andes of Ecuador. Journal of Petrology 21, 107–140. doi:10.1093/petrology/21.1.107.

761 Förster, M.W., Foley, S.F., Alard, O., Buhre, S., 2019. Partitioning of nitrogen during melting and
762 recycling in subduction zones and the evolution of atmospheric nitrogen. Chemical Geology 525,
763 334–342. doi:10.1016/j.chemgeo.2019.07.042.

764 Füri, E., Deloule, E., Dalou, C., 2018. Nitrogen abundance and isotope analysis of silicate glasses
765 by secondary ionization mass spectrometry. Chemical Geology 493, 327–337. doi:10.1016/j.
766 chemgeo.2018.06.008.

767 Gabriele, P., Ballèvre, M., Jaillard, E., Hernandez, J., 2003. Garnet-chloritoid-kyanite metapelites
768 from the Raspas Complex (SW Ecuador) a key eclogite-facies assemblage. European Journal of
769 Mineralogy 15, 977–989. doi:10.1127/0935-1221/2003/0015-0977.

770 Gale, A., Dalton, C.A., Langmuir, C.H., Su, Y., Schilling, J.G., 2013. The mean composition of
771 ocean ridge basalts. Geochemistry, Geophysics, Geosystems 14, 489–518. doi:https://doi.org/
772 10.1029/2012GC004334.

773 Green, E.C.R., White, R.W., Diener, J.F.A., Powell, R., Holland, T.J.B., Palin, R.M., 2016. Ac-
774 tivity–composition relations for the calculation of partial melting equilibria in metabasic rocks.
775 Journal of Metamorphic Geology 34, 845–869. doi:10.1111/jmg.12211.

776 Groppo, C., Beltrando, M., Compagnoni, R., 2009. The P–T path of the ultra-high pressure
777 Lago Di Cignana and adjoining high-pressure meta-ophiolitic units: insights into the evolution
778 of the subducting Tethyan slab. Journal of Metamorphic Geology 27, 207–231. doi:10.1111/j.
779 1525-1314.2009.00814.x.

780 Guggino, S.N., Hervig, R.L., 2011. Synthesis and Characterization of Five New F-bearing Basalt
781 Reference Materials (Fba Glasses): Quantifying the Fluorine Content of the Basaltic Glass Stan-
782 dards BCR-2G, BHVO-2G. GSA-1G, GSC-1G, GSD-1G, GSE-1G, ML3B-G, KL2-G, and ALV-
783 519-4. AGU Fall Meeting Abstracts 31, V31C–2535.

784 Haendel, D., Mühle, K., Nitzsche, H.M., Stiehl, G., Wand, U., 1986. Isotopic variations of the fixed
785 nitrogen in metamorphic rocks. Geochimica et Cosmochimica Acta 50, 749–758. doi:10.1016/
786 0016-7037(86)90351-0.

787 Halama, R., Bebout, G.E., John, T., Scambelluri, M., 2014. Nitrogen recycling in subducted mantle
788 rocks and implications for the global nitrogen cycle. International Journal of Earth Sciences 103,
789 2081–2099. doi:10.1007/s00531-012-0782-3.

790 Halama, R., Bebout, G.E., John, T., Schenk, V., 2010. Nitrogen recycling in subducted oceanic
791 lithosphere: The record in high- and ultrahigh-pressure metabasaltic rocks. Geochimica et Cos-
792 mochimica Acta 74, 1636–1652. doi:10.1016/j.gca.2009.12.003.

793 Halama, R., Bebout, G.E., Marschall, H.R., John, T., 2017. Fluid-induced breakdown of white
794 mica controls nitrogen transfer during fluid–rock interaction in subduction zones. International
795 Geology Review 59, 702–720. doi:10.1080/00206814.2016.1233834.

796 Halama, R., Konrad-Schmolke, M., De Hoog, J.C.M., 2020. Boron isotope record of peak meta-
797 morphic ultrahigh-pressure and retrograde fluid–rock interaction in white mica (Lago di Cig-

798 nana, Western Alps). Contributions to Mineralogy and Petrology 175, 20. doi:10.1007/
799 s00410-020-1661-8.

800 Holland, T.J.B., Powell, R., 2011. An improved and extended internally consistent thermodynamic
801 dataset for phases of petrological interest, involving a new equation of state for solids. Journal
802 of Metamorphic Geology 29, 333–383. doi:10.1111/j.1525-1314.2010.00923.x.

803 Honma, H., Itihara, Y., 1981. Distribution of ammonium in minerals of metamorphic and granitic
804 rocks. Geochimica et Cosmochimica Acta 45, 983–988. doi:10.1016/0016-7037(81)90122-8.

805 Jackson, C.R.M., Cottrell, E., Andrews, B., 2021. Warm and oxidizing slabs limit ingassing
806 efficiency of nitrogen to the mantle. Earth and Planetary Science Letters 553, 116615.
807 doi:10.1016/j.epsl.2020.116615.

808 Jochum, K.P., Willbold, M., Raczek, I., Stoll, B., Herwig, K., 2005. Chemical Characterisation
809 of the USGS Reference Glasses GSA-1G, GSC-1G, GSD-1G, GSE-1G, BCR-2G, BHVO-2G and
810 BIR-1G Using EPMA, ID-TIMS, ID-ICP-MS and LA-ICP-MS. Geostandards and Geoanalytical
811 Research 29, 285–302. doi:https://doi.org/10.1111/j.1751-908X.2005.tb00901.x.

812 John, T., Scherer, E.E., Schenk, V., Herms, P., Halama, R., Garbe-Schönberg, D., 2010. Subducted
813 seamounts in an eclogite-facies ophiolite sequence: the Andean Raspas Complex, SW Ecuador.
814 Contributions to Mineralogy and Petrology 159, 265–284. doi:10.1007/s00410-009-0427-0.

815 Johnson, B., Goldblatt, C., 2015. The nitrogen budget of Earth. Earth-Science Reviews 148,
816 150–173. doi:10.1016/j.earscirev.2015.05.006.

817 Kelley, K.A., Plank, T., Ludden, J., Staudigel, H., 2018. Composition of altered oceanic crust at
818 ODP Sites 801 and 1149. Geochemistry, Geophysics, Geosystems doi:10.1029/2002GC000435@
819 10.1002/(ISSN)1525-2027.INPUT1.

820 Kodolányi, J., Pettke, T., Spandler, C., Kamber, B.S., Gméling, K., 2012. Geochemistry of Ocean
821 Floor and Fore-arc Serpentinites: Constraints on the Ultramafic Input to Subduction Zones.
822 Journal of Petrology 53, 235–270. doi:10.1093/petrology/egr058.

Konrad-Schmolke, M., Halama, R., 2014. Combined thermodynamic–geochemical modeling in metamorphic geology: Boron as tracer of fluid–rock interaction. Lithos 208-209, 393–414. doi:10.1016/j.lithos.2014.09.021.

Krogh, E.J., Oh, C.W., Liou, J.C., 1994. Polyphase and anticlockwise P-T evolution for Franciscan eclogites and blueschists from Jenner, California, USA. Journal of Metamorphic Geology 12, 121–134. doi:10.1111/j.1525-1314.1994.tb00008.x.

Lafay, R., Deschamps, F., Schwartz, S., Guillot, S., Godard, M., Debret, B., Nicollet, C., 2013. High-pressure serpentinites, a trap-and-release system controlled by metamorphic conditions: Example from the Piedmont zone of the western Alps. Chemical Geology 343, 38–54. doi:10.1016/j.chemgeo.2013.02.008.

Lee, J.H., Peacor, D.R., Lewis, D.D., Wintsch, R.P., 1984. Chlorite-illite/muscovite interlayered and interstratified crystals: A TEM/STEM study. Contributions to Mineralogy and Petrology 88, 372–385. doi:10.1007/BF00376762.

Lesne, P., Kohn, S.C., Blundy, J., Witham, F., Botcharnikov, R.E., Behrens, H., 2011. Experimental Simulation of Closed-System Degassing in the System Basalt–H2O–CO2–S–Cl. Journal of Petrology 52, 1737–1762. doi:10.1093/petrology/egr027.

Li, K., Li, G.Y., Du, Y.F., Han, W., Zhang, J., Chen, L.H., Zhou, J.B., Li, L., 2021. Intraslab remobilization of nitrogen during early subduction facilitates deep nitrogen recycling: Insights from the blueschists in the Heilongjiang Complex in NE China. Chemical Geology 583, 120474. doi:10.1016/j.chemgeo.2021.120474.

Li, L., Bebout, G.E., 2005. Carbon and nitrogen geochemistry of sediments in the Central American convergent margin: Insights regarding subduction input fluxes, diagenesis, and paleoproductivity. Journal of Geophysical Research: Solid Earth 110. doi:10.1029/2004JB003276.

Li, L., Bebout, G.E., Idleman, B.D., 2007. Nitrogen concentration and 15N of altered oceanic crust obtained on ODP Legs 129 and 185: Insights into alteration-related nitrogen enrichment and the

nitrogen subduction budget. Geochimica et Cosmochimica Acta 71, 2344–2360. doi:10.1016/j.gca.2007.02.001.

Li, Y., Huang, R., Wiedenbeck, M., Keppler, H., 2015. Nitrogen distribution between aqueous fluids and silicate melts. Earth and Planetary Science Letters 411, 218–228. doi:10.1016/j.epsl.2014.11.050.

Mallik, A., Li, Y., Wiedenbeck, M., 2018. Nitrogen evolution within the Earth's atmosphere–mantle system assessed by recycling in subduction zones. Earth and Planetary Science Letters 482, 556–566. doi:10.1016/j.epsl.2017.11.045.

Marschall, H.R., Altherr, R., Ludwig, T., Kalt, A., Gméling, K., Kasztovszky, Z., 2006. Partitioning and budget of Li, Be and B in high-pressure metamorphic rocks. Geochimica et Cosmochimica Acta 70, 4750–4769. doi:10.1016/j.gca.2006.07.006.

Martin, C., Ponzevera, E., Harlow, G., 2015. In situ lithium and boron isotope determinations in mica, pyroxene, and serpentine by LA-MC-ICP-MS. Chemical Geology 412, 107–116. doi:10.1016/j.chemgeo.2015.07.022.

Marty, B., Zimmermann, L., Pujol, M., Burgess, R., Philippot, P., 2013. Nitrogen Isotopic Composition and Density of the Archean Atmosphere. Science 342, 101–104. doi:10.1126/science.1240971.

Melzer, S., Wunder, B., 2000. Island-arc basalt alkali ratios: Constraints from phengite-fluid partitioning experiments. Geology 28, 583–586. doi:10.1130/0091-7613(2000)28<583:IBARCF>2.0.CO;2.

Mikhail, S., Barry, P.H., Sverjensky, D.A., 2017. The relationship between mantle pH and the deep nitrogen cycle. Geochimica et Cosmochimica Acta 209, 149–160. doi:10.1016/j.gca.2017.04.007.

Mikhail, S., Sverjensky, D.A., 2014. Nitrogen speciation in upper mantle fluids and the origin of Earth's nitrogen-rich atmosphere. Nature Geoscience 7, 816–819. doi:10.1038/ngeo2271.

873 Mingram, B., Bräuer, K., 2001. Ammonium concentration and nitrogen isotope composition in
874 metasedimentary rocks from different tectonometamorphic units of the European Variscan Belt.
875 Geochimica et Cosmochimica Acta 65, 273–287. doi:10.1016/S0016-7037(00)00517-2.

876 Moine, B., Guillot, C., Gibert, F., 1994. Controls of the composition of nitrogen-rich fluids origi-
877 nating from reaction with graphite and ammonium-bearing biotite. Geochimica et Cosmochimica
878 Acta 58, 5503–5523. doi:10.1016/0016-7037(94)90246-1.

879 Nabelek, P.I., 1987. General equations for modeling fluid/rock interaction using trace elements
880 and isotopes. Geochimica et Cosmochimica Acta 51, 1765–1769. doi:10.1016/0016-7037(87)
881 90354-1.

882 Padrón-Navarta, J.A., Sánchez-Vizcaíno, V.L., Hermann, J., Connolly, J.A.D., Garrido, C.J.,
883 Gómez-Pugnaire, M.T., Marchesi, C., 2013. Tschermak's substitution in antigorite and conse-
884 quences for phase relations and water liberation in high-grade serpentinites. Lithos 178, 186–196.
885 doi:10.1016/j.lithos.2013.02.001.

886 Peacock, S.A., 1990. Fluid Processes in Subduction Zones. Science 248, 329–337. doi:10.1126/
887 science.248.4953.329.

888 Penniston-Dorland, S.C., Sorensen, S.S., Ash, R.D., Khadke, S.V., 2010. Lithium isotopes as a
889 tracer of fluids in a subduction zone mélange: Franciscan Complex, CA. Earth and Planetary
890 Science Letters 292, 181–190. doi:10.1016/j.epsl.2010.01.034.

891 Philippot, P., Busigny, V., Scambelluri, M., Cartigny, P., 2007. Oxygen and nitrogen isotopes as
892 tracers of fluid activities in serpentinites and metasediments during subduction. Mineralogy and
893 Petrology 91, 11–24. doi:10.1007/s00710-007-0183-7.

894 Poli, S., Schmidt, M.W., 2002. Petrology of Subducted Slabs. Annual Review of Earth and
895 Planetary Sciences 30, 207–235. doi:10.1146/annurev.earth.30.091201.140550.

896 Pöter, B., Gottschalk, M., Heinrich, W., 2004. Experimental determination of the ammonium

partitioning among muscovite, K-feldspar, and aqueous chloride solutions. Lithos 74, 67–90. doi:10.1016/j.lithos.2004.01.002.

Raymond, L.A., 2017. A metasomatic setting, the Russian River Arch, and gravitational emplacement in the history of eclogites at the classic eclogite locality of Jenner, California, USA. International Geology Review 59, 577–598. doi:10.1080/00206814.2016.1213143.

Reinecke, T., 1998. Prograde high- to ultrahigh-pressure metamorphism and exhumation of oceanic sediments at Lago di Cignana, Zermatt-Saas Zone, western Alps. Lithos 42, 147–189. doi:10.1016/S0024-4937(97)00041-8.

Romer, R.L., Meixner, A., Hahne, K., 2014. Lithium and boron isotopic composition of sedimentary rocks — The role of source history and depositional environment: A 250Ma record from the Cadomian orogeny to the Variscan orogeny. Gondwana Research 26, 1093–1110. doi:10.1016/j.gr.2013.08.015.

Rubatto, D., Gebauer, D., Fanning, M., 1998. Jurassic formation and Eocene subduction of the Zermatt–Saas-Fee ophiolites: implications for the geodynamic evolution of the Central and Western Alps. Contributions to Mineralogy and Petrology 132, 269–287. doi:10.1007/s004100050421.

Sadofsky, S.J., Bebout, G.E., 2000. Ammonium partitioning and nitrogen-isotope fractionation among coexisting micas during high-temperature fluid-rock interactions: examples from the New England Appalachians. Geochimica et Cosmochimica Acta 64, 2835–2849. doi:10.1016/S0016-7037(00)00393-8.

Sadofsky, S.J., Bebout, G.E., 2004. Nitrogen geochemistry of subducting sediments: New results from the Izu-Bonin-Mariana margin and insights regarding global nitrogen subduction. Geochemistry, Geophysics, Geosystems 5. doi:10.1029/2003GC000543.

Scambelluri, M., Müntener, O., Ottolini, L., Pettke, T.T., Vannucci, R., 2004. The fate of B, Cl and Li in the subducted oceanic mantle and in the antigorite breakdown fluids. Earth and Planetary Science Letters 222, 217–234. doi:10.1016/j.epsl.2004.02.012.

922 Shannon, R.D., 1976. Revised effective ionic radii and systematic studies of interatomic distances
923 in halides and chalcogenides. Acta Crystallographica Section A: Crystal Physics, Diffraction,
924 Theoretical and General Crystallography 32, 751–767. doi:10.1107/S0567739476001551.

925 Sidey, V., 2016. On the effective ionic radii for ammonium. Acta Crystallographica Section B: Struc-
926 tural Science, Crystal Engineering and Materials 72, 626–633. doi:10.1107/S2052520616008064.

927 Som, S.M., Buick, R., Hagadorn, J.W., Blake, T.S., Perreault, J.M., Harnmeijer, J.P., Catling,
928 D.C., 2016. Earth's air pressure 2.7 billion years ago constrained to less than half of modern
929 levels. Nature Geoscience 9, 448–451. doi:10.1038/ngeo2713.

930 Som, S.M., Catling, D.C., Harnmeijer, J.P., Polivka, P.M., Buick, R., 2012. Air density 2.7 billion
931 years ago limited to less than twice modern levels by fossil raindrop imprints. Nature 484, 359–
932 362. doi:10.1038/nature10890.

933 Sorensen, Grossman, J.N., Perfit, M.R., 1997. Phengite-hosted LILE Enrichment in Eclogite and
934 Related Rocks: Implications for Fluid-Mediated Mass Transfer in Subduction Zones and Arc
935 Magma Genesis. Journal of Petrology 38, 3–34. doi:10.1093/petroj/38.1.3.

936 Spandler, C., Pettke, T., Hermann, J., 2014. Experimental study of trace element release during
937 ultrahigh-pressure serpentinite dehydration. Earth and Planetary Science Letters 391, 296–306.
938 doi:10.1016/j.epsl.2014.02.010.

939 Ulmer, P., Trommsdorff, V., 1995. Serpentine Stability to Mantle Depths and Subduction-Related
940 Magmatism. Science 268, 858–861. doi:10.1126/science.268.5212.858.

941 Urann, B.M., Roux, V.L., John, T., Beaudoin, G.M., Barnes, J.D., 2020. The distribution and abun-
942 dance of halogens in eclogites: An in situ SIMS perspective of the Raspas Complex (Ecuador).
943 American Mineralogist 105, 307–318. doi:10.2138/am-2020-6994.

944 Vils, F., Pelletier, L., Kalt, A., Müntener, O., Ludwig, T., 2008. The Lithium, Boron and Beryllium
945 content of serpentinized peridotites from ODP Leg 209 (Sites 1272A and 1274A): Implications

946 for lithium and boron budgets of oceanic lithosphere. Geochimica et Cosmochimica Acta 72,
947 5475–5504. doi:10.1016/j.gca.2008.08.005.

948 White, R.W., Powell, R., Holland, T.J.B., Johnson, T.E., Green, E.C.R., 2014. New mineral
949 activity–composition relations for thermodynamic calculations in metapelitic systems. Journal
950 of Metamorphic Geology 32, 261–286. doi:10.1111/jmg.12071.

951 Wordsworth, R.D., 2016. Atmospheric nitrogen evolution on Earth and Venus. Earth and Planetary
952 Science Letters 447, 103–111. doi:10.1016/j.epsl.2016.04.002.

List of Figures

1 Sample photomicrographs and BSE images 41
2 SIMS calibration of N contents 42
3 Major and trace element data 43
4 B-N data 44
5 Bulk K_2O and N contents 45
6 N-K-Na data for chlorite 46
7 Fluid rock interaction modelling of phengite N-B-Li data from garnet-phengite quartzite (LC-3) 47
8 Equilibrium phase diagrams for sample SEC16-1 48

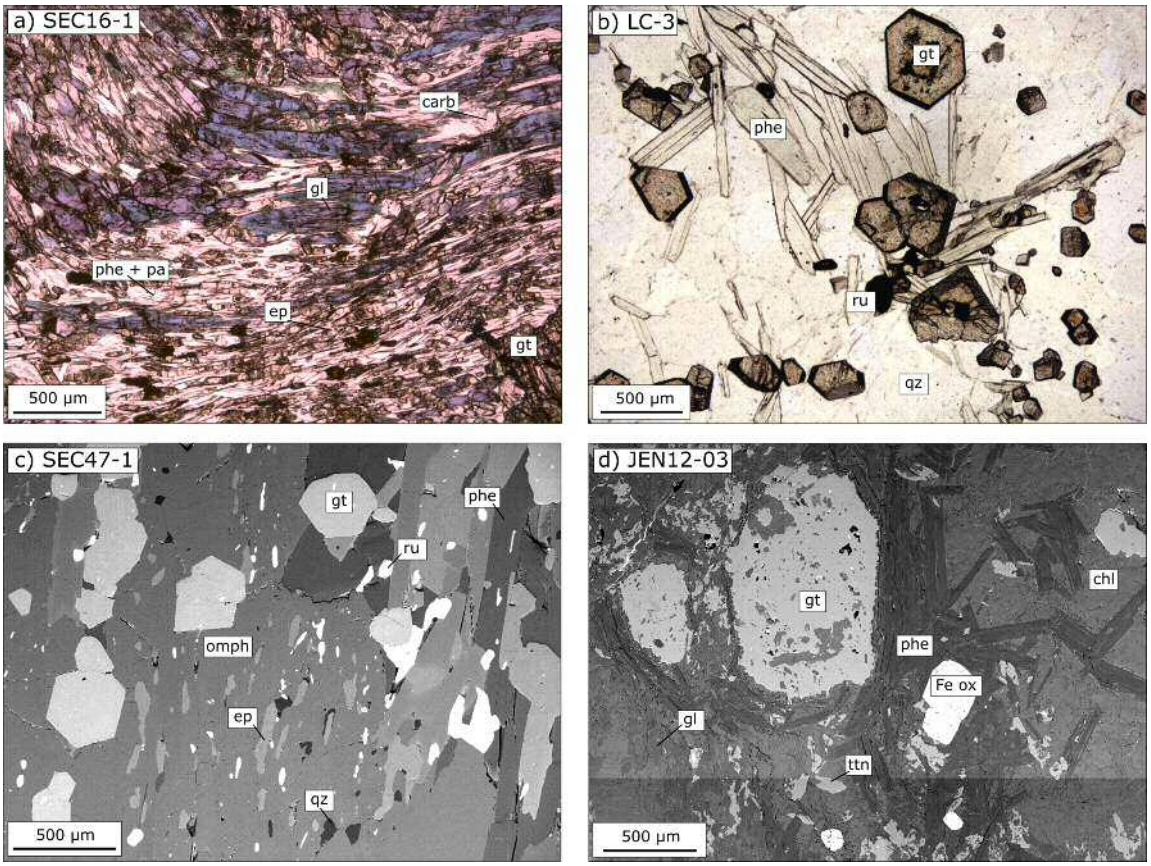

Figure 1: (a) Representative photomicrograph in plane polarised light of blueschist SEC16-1. (b) Representative photomicrograph in plane polarised light of garnet-phengite quartzite LC-3. (c) Representative back scattered electron image of eclogite SEC47-1. (d) Representative back scattered electron image of blueschist JEN12-03. Phe = phengite, pa= paragonite, gt = garnet, gl = glaucophane, ep = epidote, qz = quartz, ttn = titanite, chl = chlorite, omph = omphacite, Fe ox = iron oxide.

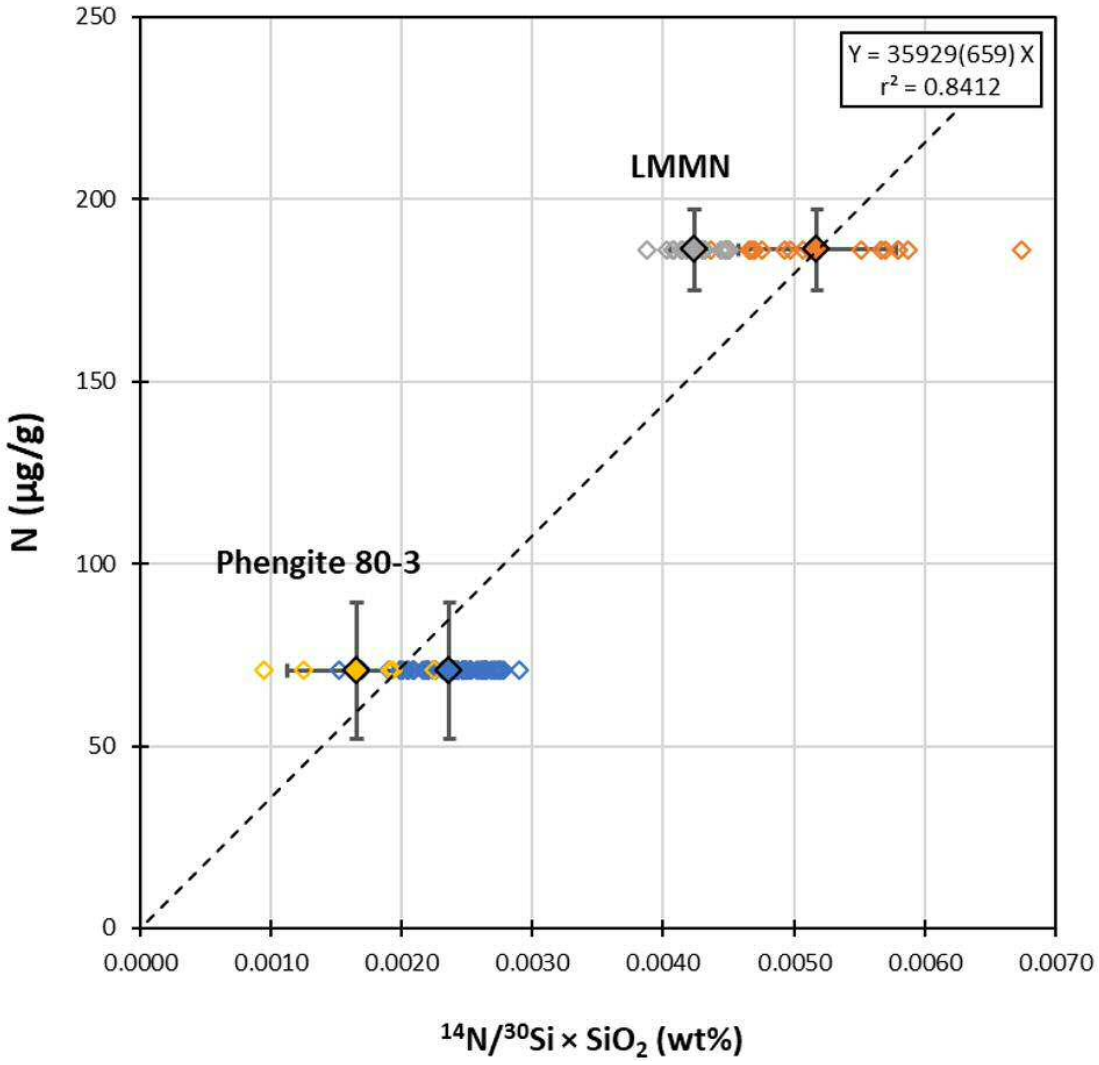

Figure 2: SIMS calibration of N concentrations based on two white mica standards (Phe80-3 and LMMN Busigny et al. (2003b, 2004)). All indiviudal analytical spots (n=70) are indicated as well as averages with 1s uncertainties. The slope of the calibration slope is indicated, along with the 1s uncertainty in brackets.

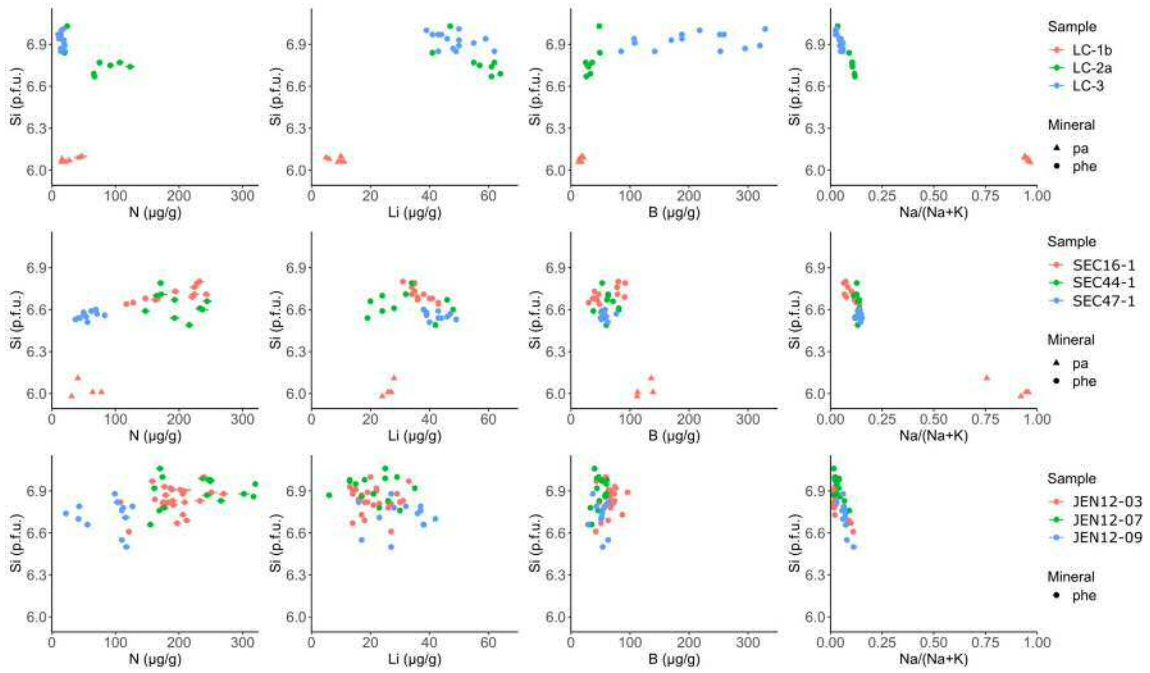

Figure 3: N, Li, B, Na/Na+K data vs Si p.f.u. for phengite and paragonite from each locality (top: Cignana, middle Raspas, bottom Jenner). 1s error bars are plotted. Where error bars are not shown, they are smaller than the size of the symbol.

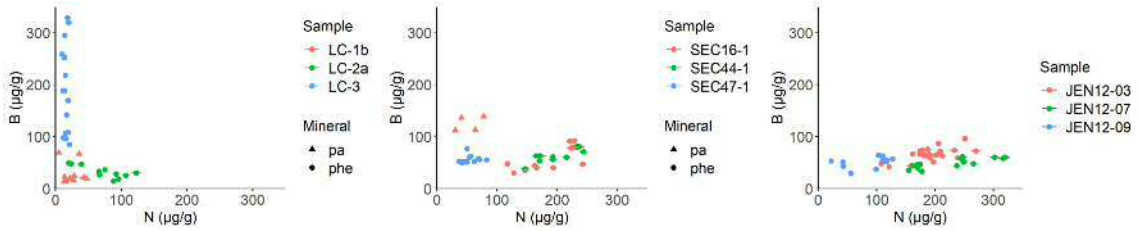

Figure 4: N vs B for phengite and paragonite from each locality (left: Cignana, middle Raspas, right Jenner). 1s error bars are plotted. Where error bars are not shown they are smaller than the size of the symbol.

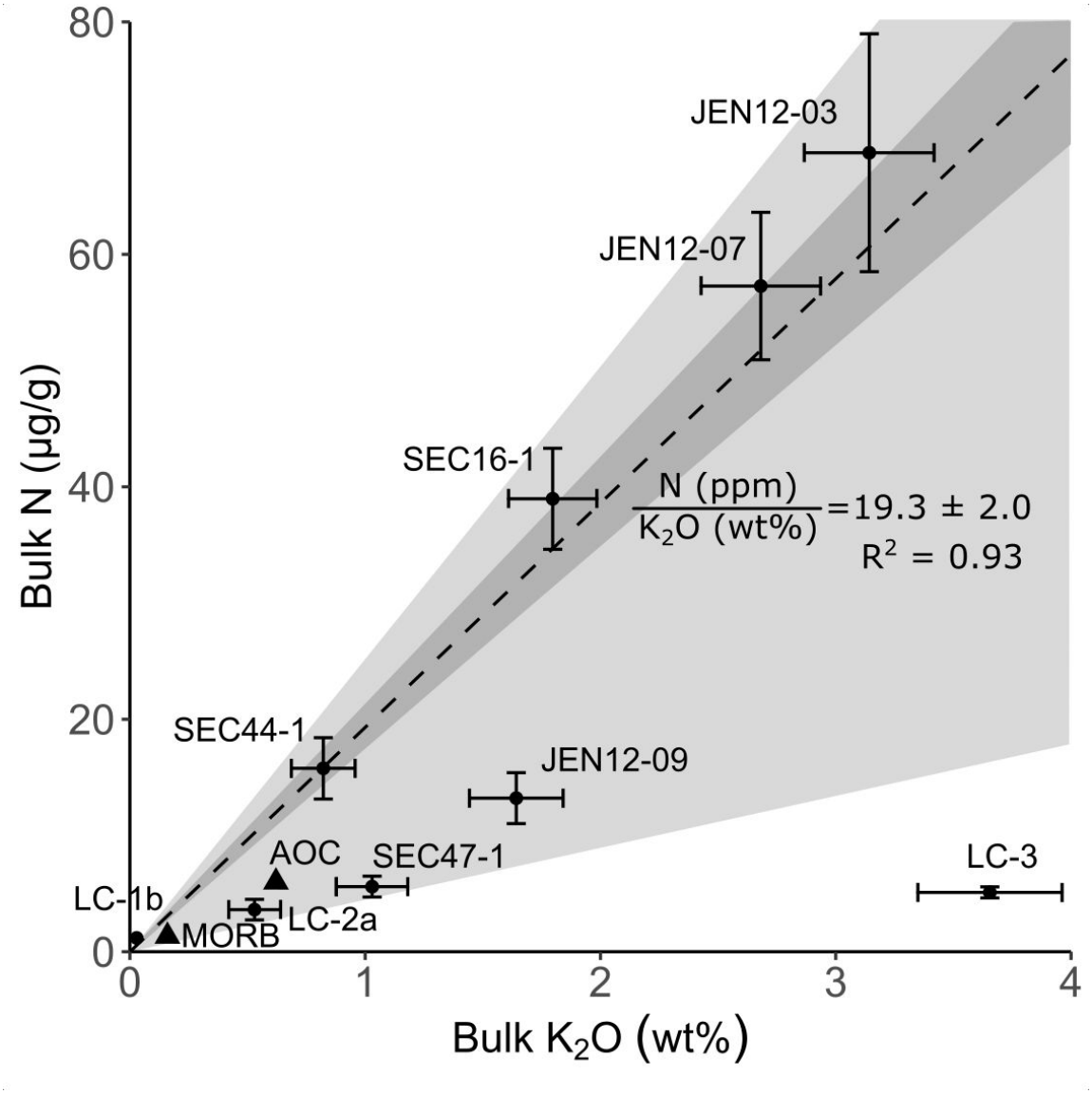

Figure 5: Calculated bulk K_2O and N contents for each sample. Average values for MORB and AOC (black triangles) are shown for comparison (Johnson and Goldblatt, 2015; Gale et al., 2013; Kelley et al., 2018). The average N/K_2O (excluding sample LC-3) is plotted as a dashed line with 1s uncertainty (dark grey). Upper and lower bounds are plotted in light grey.

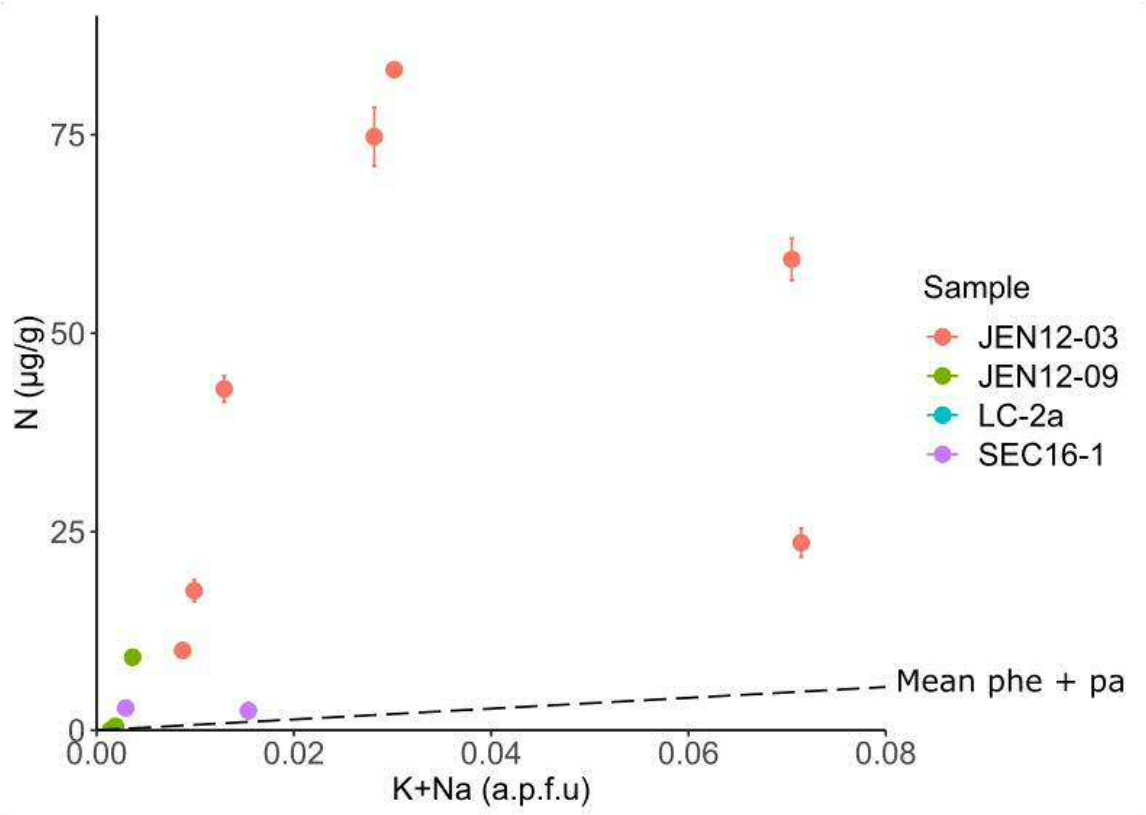

Figure 6: N versus K+Na plot for chlorite. Chlorites from sample JEN12-03 occur in the matrix alongside phengite, and have elevated K+Na and N contents. Chlorites from other samples occur as rims on garnets and contain little N, K or Na. A line showing the mean value for N/(K+Na) in phengite and paragonite is shown for comparison.

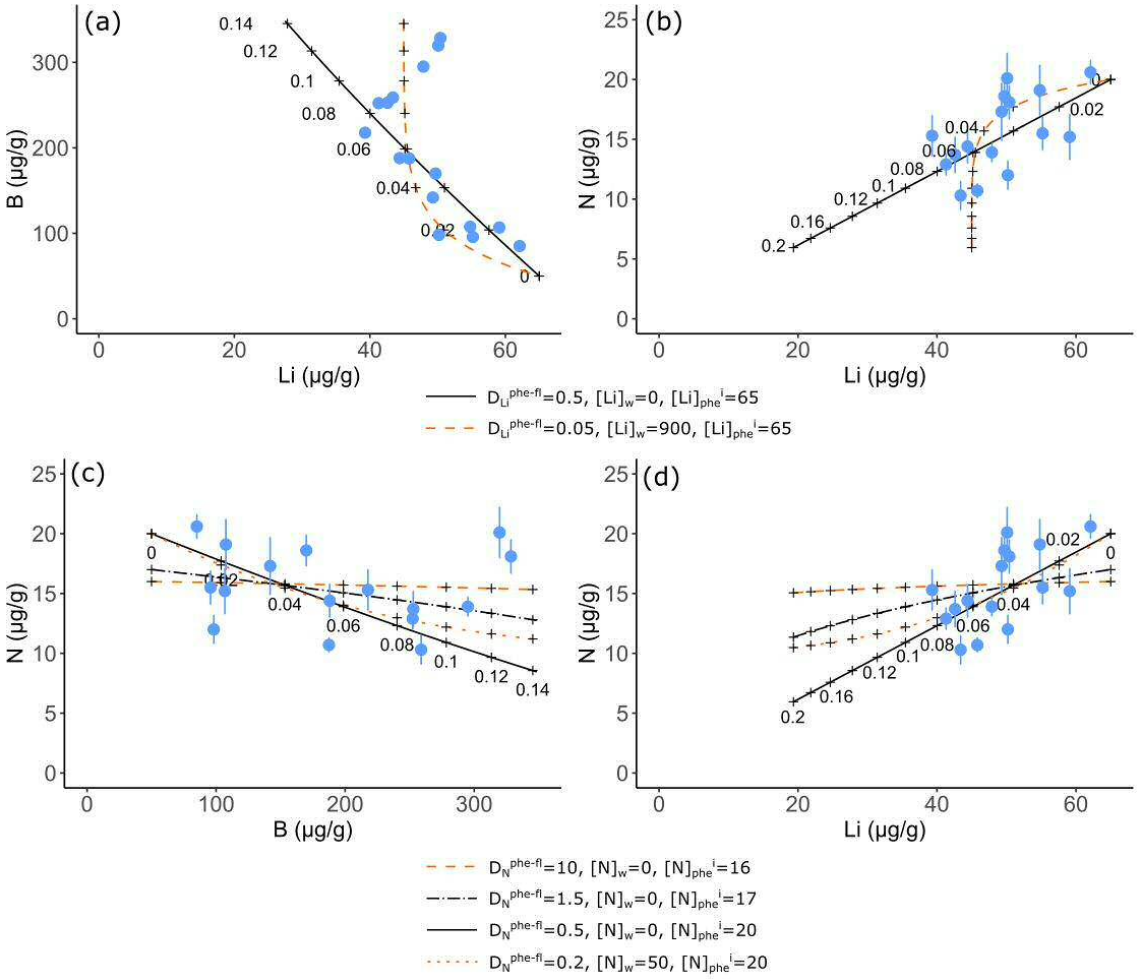

Figure 7: Fluid rock interaction modelling of phengite N-B-Li data from garnet-phengite quartzite (LC-3). Blue points are the measured data, and black lines show model outcomes for a range of different input parameters. 1s error bars are shown for N data. Error bars for B and Li are smaller than the size of the symbols. Boron input parameters were constrained from previous work (Halama et al., 2020). The top panel (a,b) shows two end member scenarios for Li modelling. The bottom panel (c,d) shows endmember scenarios for N modelling ($D_N = 10$ and $D_N = 0.2$) and two intermediate scenarios. See text for detailed explanation of modelling parameters (section 5.2).

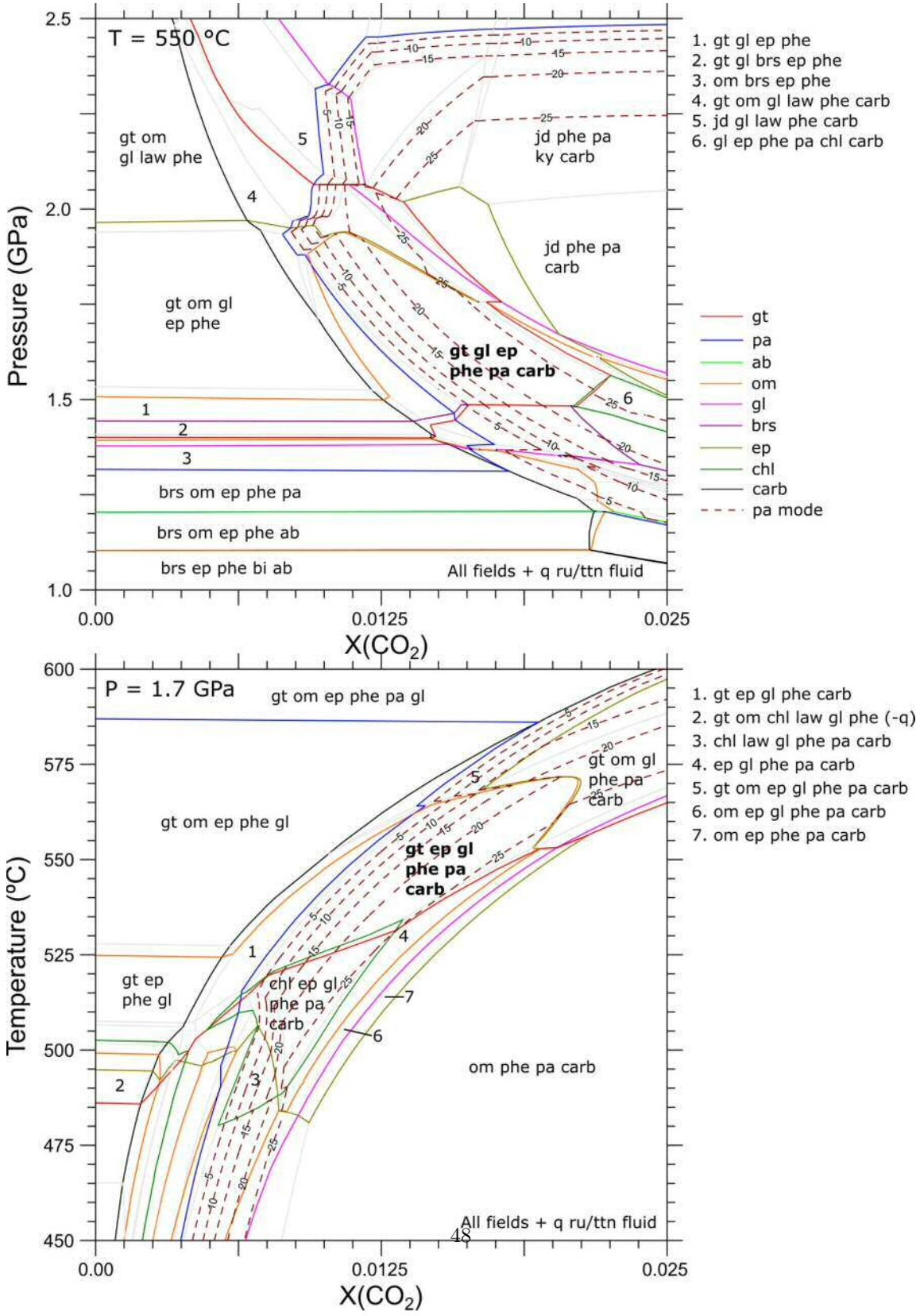

Figure 8: P-X(CO_2) and T-X(CO_2) equilibrium phase diagrams for sample SEC16-1. The observed assemblage is indicated in bold font. Gt = garnet, om = omphacite, jd = jadeite, gl = glaucophane (*sensu lato*), barroisite (*s.l.*), ep = epidote, phe = phengite, pa = paragonite, chl = chlorite, carb = carbonate, ab = albite, bi = biotite, law = lawsonite, ru = rutile, ttn = titanite.

List of Tables

1 Mineral modes and N concentrations, and calculated bulk N concentrations 50
2 Inter-mineral partition coefficients for Li, B and N 51
3 Experimental N partitioning data 52

Sample	LC-3	LC-2a	LC-1b	SEC16-1	SEC44-1
Lithology	Gt-phe quartzite	Metagabbro	Eclogite	Blueschist	Eclogite
Phe mode (vol%)	33	5		16	8
Phe N (µg/g)	10–21 (16)	20–123 (72)		117–243 (190)	147–234 (203)
Pa mode			5	16	
Pa N			5.5–47 (24)	31–78 (54)	
Chl mode		<1		<1	
Chl N		1.2–4.9 (3.6)		1.0–2.8 (2.1)	
Calculated bulk N	5.1	3.6	1.2	39	16
1s	±0.5	±0.9	±0.3	±4	±3
Measured bulk N				46	10
Sample	SEC47-1	JEN12-03	JEN12-07	JEN12-09	
Lithology	Eclogite	Blueschist	Blueschist	Eclogite	
Phe mode (vol%)	10	30	25	15	
Phe N (µg/g)	37–118 (61)	108–270 (193)	155–320 (229)	22–127 (88)	
Pa mode					
Pa N					
Chl mode		30		<1	
Chl N		10–83 (45)		0.0–9.2 (2.9)	
Calculated bulk N	5.6	71	57	13	
1s	±0.9	±10	±6	±2	
Measured bulk N	7.2				

Table 1: Mineral modes and N concentrations, and calculated bulk N contents for the nine samples in this study. N contents are given as a range followed by the mean in brackets. Three samples have measured bulk N contents (Halama et al., 2010), which are consistent with the calculated results. The procedure for calculating 1s uncertainties is described in Section 4.3 and the full data set is provided in the electronic supplement.

	Li	B	N	n
SEC44-1				
Phe	19–48 (32)	38–81 (63)	147–244 (197)	10
Cpx	94–110 (104)	2.3–3.3 (2.9)	1.8–3.0 (2.4)	4
$D^{phe/cpx}$	0.31	22	81	
SEC47-1				
Phe	38–83 (46)	50–100 (61)	37–118 (61)	11
Cpx	142	3.0	3.0	1
Ep			1–2 (1.1)	2
$D^{phe/cpx}$	0.32	18	22	
$D^{phe/ep}$			55	
SEC16-1				
Phe	31–46 (37)	30–92 (59)	117–243 (190)	14
Pa	24–28 (26)	93–139 (119)	31–118 (66)	4
Gl	132–169 (151)	3.9–4.9 (4.4)	3.9–4.4 (4.1)	2
$D^{phe/pa}$	1.5	0.49	2.9	
$D^{phe/gl}$	0.25	13	46	
JEN12-09				
Phe	16–42 (30)	29–64 (51)	22–127 (88)	12
Cpx	46–55 (51)	1.2–1.3 (1.3)	1.5–1.9 (1.7)	2
$D^{phe/cpx}$	0.60	41	52	

Table 2: Inter-mineral partition coefficients for Li, B and N. Mineral compositions are given in µg/g as a range with a mean value in brackets. The number of analyses (n) is also listed. Partition coefficients are calculated from the mean values.

	P (GPa)	T (°C)	$D^{\text{phe}-\text{fl}}$	$D^{\text{bi}-\text{fl}}$	$D^{\text{bi}-\text{phe}}$
Förster et al. (2019)	2	750	10		
Förster et al. (2019) *	3	800–1000	0.5–1.1	0.2–1.6	1.5–3.1
Pöter et al. (2004)	0.4	400–600	0.12–0.15		3.5
Pöter et al. (2004)	1.5	400–600	0.19–0.20		
Jackson et al. (2021) *	0.2–2.3	725–925		0.01–0.4	
Moine et al. (1994)	0.2	550		~0.5	
Honma and Itihara (1981) **	~ 0.4	~ 700			1.5–3.1
Duit et al. (1986) **	~ 0.5	500–700			2.2–4.2
Busigny et al. (2004) **					2.6–3.3

Table 3: Summary of available partitioning data for nitrogen between aqueous fluid and micas (phengite and biotite). Most data are from subsolidus experiments but data indicated with a * are from suprasolidus experiments. Some natural data on biotite-phengite partitioning are also included (**).

The behaviour of nitrogen during subduction of oceanic crust: insights from *in situ* SIMS analyses of high-pressure rocks

B.J.R. Harris[a,*], J.C.M. de Hoog[a], R. Halama[b]

[a] *Grant Institute, University of Edinburgh, James Hutton Road, Edinburgh, United Kingdom, EH9 3FE*
[b] *School of Geography, Geology and the Environment, Keele University, Keele, Staffordshire, United Kingdom, ST5 5BG*

[*] Corresponding author: b.j.r.harris@sms.ed.ac.uk

Abstract

Understanding the Earth's geological nitrogen (N) cycle requires an understanding of how N behaves during dehydration of subducted crust. We present the first *in situ* measurements of N in silicate minerals by secondary ion mass spectrometry, focusing on high pressure rocks representing subducted oceanic crust. We investigate the distribution of N between mineral phases, and combine analyses of N with other trace and major elements in order to constrain the behaviour of N during fluid-rock interaction. The data confirm that white mica (phengite, paragonite) is the primary host for N, containing up to 320 µg/g, whereas minerals including clinopyroxene, amphibole and epidote contain < 5 µg/g N. Chlorite can also contain N (up to 83 µg/g) and may play a previously unrecognised role in subduction zone N cycling. Bulk rock N concentrations estimated from mineral N concentrations and mineral modes are consistent with N concentrations measured by bulk combustion, which confirms that most N is hosted within silicate minerals and not along grain boundaries or in fluid inclusions. Bulk rock N contents correlate with K_2O ($N/K_2O = 19.3 \pm 2.0$). Using N/K_2O ratios and the average K_2O of altered oceanic crust, the flux of N subducted in oceanic crust is estimated to be $0.6 - 2.4 \times 10^{11}$ g/yr, which is consistent with but at the lower end of previous estimates. The data were also used to investigate the behaviour of N during fluid-rock interaction. Open system fluid-rock interaction modelling was used to model the evolution of N, B and Li contents during fluid-rock interaction in phengite from a garnet-phengite quartzite. By comparison to data for B and Li, the phengite-fluid partition coefficient for N was estimated to be 0.1–1.5. Separately, the growth of paragonite during fluid-rock interaction in a blueschist was shown to sequester N from phengite and limit bulk N loss to the fluid. The stability of white mica during fluid-rock interaction is therefore critical in controlling the behaviour of N. Nitrogen addition from sediment-derived fluids appears to be an important process in subduction zone rocks. Mafic crust can act as a sink for this N if white mica is stable. This work provides the first natural constraints on the fluid-mineral partitioning behaviour of N at subduction zone conditions and emphasises the complexity of N mobility within subduction zones, with redistribution between different phases and lithologies being important.

1. Introduction

The Earth's atmosphere is presently composed of 78% nitrogen and is essential for the habitability of the planet. There is considerable debate over the long-term evolution of the mass of N in the atmosphere (e.g. Mallik et al., 2018; Som et al., 2016; Wordsworth, 2016; Barry and Hilton, 2016; Busigny et al., 2011; Marty et al., 2013; Som et al., 2012; Berner, 2006; Avice et al., 2018) and it is therefore necessary to quantify the flux of N between the surface and deep-seated reservoirs, primarily the mantle. Subduction zones are the primary locations where N from the Earth's surface is returned to the mantle, and therefore studies which explore the behaviour of N during subduction are of importance to resolving the long-term N cycle. Previous studies of N in subduction-related rocks have focused on whole rock analyses, with a particular focus on N isotopic work (e.g. Epstein et al., 2021; Halama et al., 2010, 2014; Bebout et al., 2013; Busigny et al., 2011, 2003a; Halama et al., 2017). Suites of subducted metasediments have shown little N loss up to 90 km depth in cold subduction zones (Busigny et al., 2003a; Bebout et al., 2013), but substantial losses in warm subduction zones (Bebout and Fogel, 1992; Haendel et al., 1986; Mingram and Bräuer, 2001), with differing implications for the recycling of N over Earth's history. Basalts and gabbros representing oceanic crust (~1–30 µg/g N) have lower N contents than sediments (~100–2000 µg/g N) but the mass of subducted oceanic crust is an order of magnitude higher than of sediments. Considering average values for oceanic crust and sediment N concentrations, their contributions to the subducted N flux are comparable, although oceanic crust is less well constrained (Halama et al., 2010; Busigny et al., 2011; Li et al., 2007). Overall uncertainty in the global N recycling flux is on the order of 50–100% (Johnson and Goldblatt, 2015) due to the variable N contents of subducted lithologies and the lack of understanding of the processes controlling N recycling.

Nitrogen in rocks is primarily hosted as ammonium (NH_4^+), which substitutes for potassium and, to a lesser extent, sodium and calcium (Honma and Itihara, 1981). Micas are the dominant host of K in metasediments, and correlations between bulk K and N contents have been used to confirm that white micas are the main host for N (e.g. Bebout et al., 2013; Busigny et al., 2003a). High N contents of up to 1700 µg/g have been measured in micas from metasediments (Busigny et al., 2003b, 2004; Sadofsky and Bebout, 2000). For metabasic rocks that contain white mica,

correlated bulk N, Cs and Ba concentrations also suggested that N resides in the mica (Halama et al., 2010). However, a weak correlation of N with CaO + Na_2O in mica-free metabasic rocks may suggest that in these lithologies, N is hosted in Ca- and Na-bearing minerals (Busigny et al., 2011).

Nitrogen is regarded as a moderately fluid-mobile element. Several studies on rocks that have undergone extensive fluid-rock interaction have shown up to 60% loss of bulk N in metasomatised rocks compared to the country rock, in response to white mica dissolution or recrystallization during fluid-rock interaction (Halama et al., 2017; Epstein et al., 2021). Experimental data on fluid-mineral partition coefficients for N at subduction zone pressure-temperature conditions are sparse and values are not consistent between studies (Table 3, Pöter et al. (2004); Förster et al. (2019); Jackson et al. (2021); Li et al. (2015)). There is agreement between these studies that increasing pressure leads to NH_4^+ becoming more compatible in both phengite and biotite, compared to an aqueous fluid, because NH_4^+ is thermodynamically favoured over N_2 at higher pressures (Förster et al., 2019; Pöter et al., 2004; Jackson et al., 2021). The effect of temperature is smaller but increasing temperature leads to NH_4^+ becoming more compatible in phengite, compared to an aqueous fluid (Förster et al., 2019; Pöter et al., 2004). and less compatible in biotite (Förster et al., 2019; Jackson et al., 2021). The reasons for this are not fully understood. NH_4^+ is overall more compatible in biotite than muscovite over a wide range of P-T conditions, with values for $D_{NH_4^+}^{biotite-muscovite}$ from 1.5–4.2 (Sadofsky and Bebout, 2000; Busigny et al., 2004; Duit et al., 1986; Honma and Itihara, 1981; Pöter et al., 2004; Förster et al., 2019).

In situ data can provide new constraints on the partitioning of N between different minerals, reveal heterogeneities or zoning, and can be combined with thermodynamic and geochemical modelling to understand the behaviour of N during metamorphism and fluid-rock interaction. Previous *in situ* analyses of N contents were limited to a small number measurements of large white mica and biotite grains in metasediments by Fourier transform infrared spectroscopy with a 100 µm beam size (Busigny et al., 2003b,a, 2004). Few studies have compared N contents of minerals to other major or trace elements, or to textural features of the samples. *In situ* analyses of other fluid-mobile elements (e.g. B, F, Cl, LILE) in subduction-related samples have been successful in

constraining the inter-mineral partitioning behaviour of these elements, understanding their behaviour during metamorphic reactions and fluid-rock interaction, and constraining the amount of recycling of these elements into the mantle during subduction (e.g. Marschall et al., 2006; Urann et al., 2020; Halama et al., 2020; Debret et al., 2016; Bebout et al., 2007; De Hoog et al., 2014; Clarke et al., 2020). In this study we aim to: 1) explore the residency of N in different minerals in a suite of high pressure rocks representing formerly subducted oceanic crust; 2) combine *in situ* measurements of N concentrations with other trace and major elements to explore the behaviour of N during metamorphic fluid-rock interaction. Improved D values and mineral residency of N will allow more detailed modeling of N behaviour during subduction and eventually more accurate models of the long-term global N cycle in deep time.

2. Geological background and sample descriptions

2.1. Lago di Cignana, Italy

At Lago di Cignana, NW Italy, meta-ophiolites of the Zermatt-Saas Zone (ZSZ) are tectonically juxtaposed with a coesite- and diamond-bearing UHP metamorphic unit, the Lago di Cignana Unit (LCU) (Groppo et al., 2009). The LCU comprises eclogites, alongside metasediments including impure marbles and quartzites, and calcschists. Peak metamorphism of the LCU ocurred at ~600 °C, 2.7–3.2 GPa (Groppo et al., 2009; Reinecke, 1998), and was dated to 44 Ma by zircon U-Pb (Rubatto et al., 1998). The ZSZ comprises mantle serpentinites and eclogitic gabbros, which experienced a similar P-T-t history to the LCU (Groppo et al., 2009). REE patterns of eclogites from both the LCU and ZSZ indicate a MORB protolith (Halama et al., 2010; Dal Piaz et al., 1981).

The samples from Lago di Cignana have been described previously (Halama et al., 2020) but a brief description is reproduced here.

LC-3 is a garnet-phengite-quartzite (metachert) containing garnet, phengite and quartz as major phases, and accessory amphibole, biotite, rutile and opaques (Figure 1b). Garnet is euhedral, 100–500 μm in diameter and zoned, with Mn and Mg-enriched cores and Fe and Ca-enriched rims. Phengite occurs as 300–1500 μm flakes, which are preferentially aligned to define a weak foliation.

LC-1b is an eclogite containing garnet, omphacite, blue amphibole, epidote, paragonite and quartz. Paragonite occurs as needles, which are sometimes associated with rhombic pseudomorphs after lawsonite, formed during early retrograde decompression (Groppo et al., 2009).

LC-2a is a metagabbro. Omphacite, phengite, epidote, albite and chlorite are major phases, with accessory amphibole, titanite and rutile. This sample has been interpreted as showing pervasive retrogression into the greenschist-facies from a former high-pressure assemblage.

2.2. Raspas Complex, Ecuador

The Raspas Complex in southwest Ecuador exposes an high pressure terrane representing formerly subducted oceanic lithosphere (Arculus et al., 1999; Feininger, 1980). It includes eclogites and blueschists of the Raspas Formation, which occur alongside garnet-chloritoid-kyanite metapelites. All three lithologies record similar peak pressure-temperature conditions of 550–600 °C, 1.5–2 GPa (John et al., 2010; Gabriele et al., 2003). The age of metamorphism was dated to ~130 Ma, using Lu-Hf methods (John et al., 2010). Lithological differences between the blueschists and eclogites are ascribed to differences in bulk composition, with the blueschists being enriched in K_2O and Al_2O_3, and depleted in CaO, MgO and FeO. Geochemical analysis of the eclogites suggests that their protoliths were typical mid-ocean-ridge-basalts (MORB), with LREE-depleted REE patterns. Blueschists show LREE-enrichment, which has been interpreted as evidence of a seamount-type protolith (John et al., 2010).The samples from the Raspas Complex have not been described individually, but descriptions of each lithology are given in (John et al., 2010).

SEC16-1 is a blueschist containing garnet, Na-amphibole, phengite, paragonite, epidote, apatite, and calcium carbonate, with accessory chlorite (Figure 1a). Garnets (500–1500 μm) preserve an original euhedral outline but are sometimes corroded at the rims. A strong foliation is defined by preferential alignment of Na-amphibole, epidote, phengite and paragonite in the matrix. Epidote occurs also as elongate inclusions in garnet, which are aligned with the external foliation. Some apatite grains are elongate and aligned with the foliation. Chlorite occurs along fractures in garnet and at corroded rims.

SEC44-1 is an eclogite containing garnet, omphacite, phengite and quartz as major phases, and

accessory Na-amphibole, rutile and apatite. Subhedral to euhedral garnets (100–600 μm) cluster in garnet-rich (up to 50 %) layers up to 3 mm thick. The matrix consists of subhedral omphacite and rutile, randomly oriented phengite flakes, which are often rectangular, and interstitial quartz. Intergrowths of lobate quartz with Na-amphibole occur in low abundance, usually in proximity to garnet.

SEC47-1 is an eclogite containing garnet, omphacite, phengite, quartz, Na-amphibole and epidote as major phases, with accessory rutile (Figure 1c). Subhedral to euhedral garnet (50–400 μm) occurs in garnet-rich (up to 80 %) layers up to 4 mm thick. Preferential alignment of epidote, Na-amphibole, omphacite and phengite define a weak foliation, which is sub-parallel to the garnet layering. Quartz and rutile also occur in the matrix.

2.3. Jenner, California

Eclogite and blueschist blocks at Jenner, California, occur as part of the Franciscan Complex, a subducted-related melange complex in NW California. Samples were collected just north of the mouth of the Russian River about 1.5 km west of Jenner. These blocks occur loose on the beach, or within a sandstone-shale-rich matrix, which is interpreted a a recent landslide deposit (Raymond, 2017). The presence of Mg-rich metasomatic rinds, and geochemical signatures within the blocks, have been used to infer a former serpentinite melange host (Errico et al., 2013). Enrichment in large ion lithophile elements (LILE) and low ϵ_{Nd} and δ^7Li values in some blocks has been used to infer an additional sediment-derived fluid source (Sorensen et al., 1997; Penniston-Dorland et al., 2010). Peak metamorphic assemblages in eclogite and blueschist facies are identified in the least retrograded samples and record conditions of ~450–500 °C, 1–1.5 GPa (Krogh et al., 1994). Prograde to peak garnet growth was dated to c. 158 Ma using Lu-Hf methods (Anczkiewicz et al., 2004). Many samples are retrograded to a lower temperature assemblage (~400 °C, 1 GPa), along a counterclockwise P-T path, which is attributed to secular cooling of the subduction zone. Whole rock major element and immobile trace element compositions are similar to MORB (Penniston-Dorland et al., 2010; Sorensen et al., 1997).

JEN12-03 is a blueschist containing garnet, Na-amphibole, omphacite, phengite, titanite, chlo-

rite and quartz, with accessory iron oxides (Figure 1d). Three textural domains are identified. Rare omphacite-rich domains suggest a former eclogite facies assemblage. Large domains comprise a matrix of glaucophane, titanite, phengite, quartz and minor chlorite, with garnet occurring as porphyroblasts (up to 700 μm diameter). Garnets preserve an original euhedral outline but are corroded around the rims. A third domain is dominated by phengite flakes and fine grained chlorite. In all domains phengite occurs mostly as randomly oriented laths. Around 5 % of the phengite comprises rectangular to rhomboid grains, which are zoned in back scattered electron images.

JEN12-07 is a blueschist containing garnet, Na-amphibole, phengite, epidote and titanite, with accessory Fe-sulphides, apatite, quartz and chlorite. The matrix consists of aligned Na-amphibole, epidote, titanite and phengite, which define a foliation. Phengite also occurs as large (up to 500 µm) randomly oriented laths. Garnet occurs as 1–2.5 mm porphyroblasts with inclusions of Na-amphibole, epidote, titanite, quartz and chlorite, which preserve a foliation that is rotated relative to the external foliation.

JEN12-09 is an eclogite containing garnet, omphacite, phengite, epidote and titanite, with accessory chlorite, rutile, and quartz. The matrix consists of omphacite, phengite, epidote and titanite. Garnet occurs as 0.5–3 mm subhedral to euhedral porphyroblasts, containing inlcusions of omphacite, phengite, quartz and rutile. Chlorite occurs only on the rims of garnets. Phengite also occurs as up to 500 µm long grains in a 2 mm thick vein.

[Figure 1 about here.]

3. Analytical methods

3.1. Major element contents

Mineral compositions of some samples (see supplementary material) were determined using a Cameca SX100 electron microprobe equipped with 5 wavelength dispersive spectrometers (WDS) at the Department of Earth Sciences, University of Cambridge, UK. Acceleration voltage was 20 kV, beam current was 20 nA and beam diameter was 5 μm. On-peak counting times (seconds) for elements were as follows (background time in brackets): K 10 (5), Na 10 (5), Mg 30 (15), Si 10

(5), Al 30 (15), Fe 40 (20), Ca 20 (10), Ti 60 (30), Mn 90 (45). A variety of synthetic and natural standards were used for calibration and a PAP matrix correction was applied. Other samples were analysed using a JEOL JXA 8900R electron microprobe at the University of Kiel, Germany. Elements were measured 15 s on peak and 7 s on background with an acceleration voltage of 15 kV, beam current of 15 na and beam diameter of 5 μm. Natural standards were used for calibration and a CITZAF matrix correction was applied. EPMA spots were located as close as possible to the corresponding SIMS spots.

3.2. Nitrogen, volatile and trace element contents

Nitrogen contents of minerals were determined *in situ* by Secondary Ion Mass Spectroscopy (SIMS) at the Edinburgh Ion Microprobe Facility using a Cameca 7f-GEO with Hyperion source. Standard polished thin sections were cut to 25 mm rounds and gold-coated prior to loading into high vacuum (ca. 3×10^{-9} mbar). The sample surface was sputtered with a focused $^{16}O^-$ beam with a 18 nA beam current and an impact energy of 13.5 keV. Spot size was about 15 µm. One spot was analysed per grain, except where core and rim spots were analysed and reported separately. Prior to each analysis the analytical area was pre-sputtered for 120 s using a 15 µm beam raster to avoid background contamination. An effective field aperture of 20 µm was used to further reduce N backgrounds to <0.4 µg/g. Positive secondary ions sputtered from the sample were accelerated into a mass spectrometer and counted with an electron multiplier. An energy window of 50±20 V was applied to the secondary ion beam to reduce potential matrix effects. A mass resolution of 2000 (M/ΔM) was used to avoid interferences of $^{28}Si^{2+}$ and $^{12}CH_2{}^+$ on the $^{14}N^+$ signal, as well as $^7Li^{28}Si$ and $^{19}F^{16}O$ on ^{35}Cl. The mass calibration was updated at the start of each analysis using an automated peak centering routine on the ^{30}Si peak. The following isotopes were measured (total counting times per analysis in seconds in brackets): ^7Li (18), ^{11}B (30), $^{28}Si^{2+}$ (12), ^{14}N (60), ^{19}F (30), ^{26}Mg (12), ^{30}Si (12), ^{35}Cl (60). The ^{30}Si signal was used for internal standardisation using known SiO_2 contents measured by EPMA. As the wrong peak for ^{35}Cl was selected during the initial run, all analytical spots were repeated in a separate routine measuring ^{26}Mg, ^{30}Si and ^{35}Cl only, with other analytical parameters kept identical to the original run. Phengite mica 80-3

(71±19 µg/g N) and muscovite LMMN (186±11 µg/g N) were used for calibration of the N contents (Busigny et al., 2003b, 2004), St8.1.A9 basaltic glass for Cl (Lesne et al., 2011), Fba-5 basaltic glass for F (Guggino and Hervig, 2011), and GSD1-G basaltic glass for remaining elements (Jochum et al., 2005), the results of which are presented in the electronic supplement. ^{14}N count rates were low, equalling to a relative ion yield (RIY) compared to Si of ca. 0.002, which is why this element is not commonly measured, but signals were high enough to give acceptable counting statistics with the analytical conditions used. For example, for standard LMMN#2 (186 µg/g N), the ^{14}N count rate was ca. 35 count per second, for a total of 2100 counts for the whole analysis (60s for ^{14}N) and a standard deviation of 2.2% based on counting statistics. This is nearly identical to the 1s uncertainty based on the 6 repeat cycles for each analyses (internal precision), which was 2.4%, indicating that analytical uncertainty was dominated by counting statistics. Repeatability (external precision) of this standard was 4.3% (n=16, see Supplementary Table), so about double the internal precision, which is probably mostly related to slight heterogeneity of the standard and/or instrumental factors. 1s uncertainties presented in the figures is based on the propagated uncertainty of the measurements (internal precision) and the uncertainty of the slope of the calibration line (Figure 2). The measurement of molecular species such as ^{14}N^{16}O or ^{28}Si^{14}N was explored in the course of this study, but did not yield any advantage, as with the positive secondary ion beam used in our setup the yield of these species was lower than the ^{14}N signal. This contrasts results in negative ion mode, where an advantage was observed (Füri et al., 2018), resulting in lower detection limits, but considering our ^{14}N count rates were sufficient for the material under investigation, we preferred to be able to analyse other fluid-mobile elements at the same time as N. The two LMMN grains gave slightly different averages (187±22 and 153±7 µg/g, respectively, with n=20), the first grain containing areas with higher N contents (Figure 2). MgO contents (0.8 wt%) also showed about 10% variation, indicating some heterogeneity in this material (Figure 2). Multiple repeats of the Phe80-3 standard showed 13% variation (1s) in N content, which suggests some heterogeneity in this material as well, as it is much higher than the rsd for individual analyses (3%) and repeatibility of LMMN grain #2 (4%). Thus, the overall added uncertainty due to calibration uncertainty is ca. 15% Furthermore, we obtained a value of 17±0.4 µg/g N (n=2) on muscovite ms98973, for which no

N data has been published. Basaltic glasses GSD1-G and BCR2-G both showed concentrations of about 1.5±0.5 µg/g N, which is only slightly higher than what we measured for quartz (0.4 µg/g). As it is possible that these materials contain small amounts of N, no background correction was applied. Muscovite ms98973 (Dyar et al., 2001) was intended to be used as a secondary standard to detect potential matrix effects between basaltic glass and white mica, but we found that our concentrations for B (23-35 µg/g) and particularly Cl (31±13 µg/g) are very far from published values (180 and 700 µg/g, respectively; Dyar et al. (2001)), as well as highly heterogeneous. Fluorine was more homogeneous and our value of 12840 ± 45 µg/g is in reasonable agreement with the published value of 16800 µg/g Dyar et al. (2001). We also analysed two micas from Martin et al. (2015), namely JJE01-X-3 mica and MVE02-8-5 mica to evaluate their use as potential N standards. However, although N contents were high, unfortunately they were also extremely heterogeneous for N, Li and B (see electronic supplement).

[Figure 2 about here.]

4. Results

4.1. Major element mineral chemistry and N, B, Li concentrations in white mica

4.1.1. Lago di Cignana

Garnet-phengite quartzite sample LC-3 contains phengite with Si contents from 6.85–7.00 p.f.u. and Na/(Na+K) from 0.02–0.06 (Figure 3). There is a strong negative correlation between Si p.f.u. and Na/(Na+K). Nitrogen contents occupy a narrow range from 10–21 µg/g, whilst B contents vary widely (85–329 µg/g). Lithium contents vary from 39–62 µg/g. Despite the wide range in B contents, there is no clear trend in [N] versus [B]. Lithium contents show an overall negative correlation with [B], and positive correlation with [N] (Figure 7).

Metagabbro sample LC-2a contains two populations of phengite with different major element chemistry (Figure 3). Six grains had Si contents from 6.67–6.77 p.f.u. and Na/(Na+K) = 0.10-0.12. Two grains had higher Si contents (6.84–7.03) and Na/(Na+K) = 0.04–0.12. The low Si population

has [N] from 66–123 µg/g, [B] from 25-36 µg/g and [Li] from 55–64 µg/g. The high Si population has lower [N] (20–24 µg/g), higher [B] (48–49 µg/g) and lower [Li] (41–47 µg/g).

Eclogite sample LC-1b contains paragonite with a narrow range of Si contents (6.06–6.10 p.f.u.) and Na/(Na+K) = 0.94–0.97 (Figure 3). There is a negative correlation between Si p.f.u. and Na/(Na+K). Nitrogen contents vary from 15–47 µg/g, [B] from 13-24 µg/g and [Li] from 5-11 µg/g. There are no correlations between major and trace element concentrations.

4.1.2. Raspas

Eclogite sample SEC44-1 contains phengite with Si content ranging from 6.49–6.79 p.f.u., and Na/(Na+K) from 0.11–0.14 (Figure 3). Phengite grains are not zoned in major element chemistry. Nitrogen contents range from 147–244 µg/g and are not correlated with variations in major element chemistry. Boron contents range from 38–81 µg/g and Li contents from 19–48 µg/g. There is a positive correlation between [N] and [B] with average [N]/[B] ~3.2 (Figure 4).

Eclogite sample SEC47-1 contains phengite with a narrow range of Si contents from 6.51–6.60 p.f.u., and Na/(Na+K) from 0.12–0.15 (Figure 3). Phengite grains are not zoned in major element chemistry. Nitrogen contents range from 37–83 µg/g, so are considerably lower than in sample SEC44-1. Boron contents vary from 50–77 µg/g and Li contents from 38–49 µg/g. Phengite grains show no significant intra-grain variation in [Li], [B] or [N]. There are no correlations between major and trace element concentrations.

Blueschist sample SEC16-1 contains phengite as well as paragonite. Phengite has Si contents from 6.64–6.80 p.f.u. and Na/(Na+K) from 0.06–0.14 (Figure 3). There is a negative correlation between Si content and Na/(Na+K). Phengite grains are not zoned in major element chemistry. N contents range from 117–243 µg/g, B contents from 30–92 µg/g and Li contents from 31–43 µg/g. There is a positive correlation between Si p.f.u. and [N], and Si p.f.u. and [B], and a negative correlation between Si p.f.u. and [Li]. Paragonite has Si = 5.98–6.00 p.f.u. and Na/(Na+K) = 0.92–0.96. Paragonite N contents range from 31–78 µg/g, [B] from 112–139 µg/g, and [Li] from 24–28 µg/g. One exceptional grain has higher Si p.f.u. and lower Na/(Na+K) than other paragonites, with Si = 6.11 p.f.u. and Na/(Na+K) = 0.76, but unexceptional trace element contents. There are

no correlations between major and trace element concentrations in paragonite.

4.1.3. Jenner

Sample JEN12-03 contains phengite with a large range of Si contents from 6.61–7.00 p.f.u. Most grains have Na/(Na+K) from 0.01–0.03 and show no correlation between Na/(Na+K) and Si p.f.u. (Figure 3). Three low Si grains have much higher Na/(Na+K) from 0.09–0.11 and show a negative correlation between Na/(Na+K) and Si p.f.u.. Nitrogen contents range from 108–270 µg/g, [B] from 42–96 µg/g and [Li] from 13–33 µg/g. There are no correlations between trace and major element concentrations.

Sample JEN12-07 contains phengite with a large range of Si contents from 6.66–7.06 p.f.u. and Na/(Na+K) = 0.02–0.09 (Figure 3). There is a negative correlation between Si p.f.u. and Na/(Na+K). Nitrogen contents vary from 155–320 µg/g and are uncorrelated with Si p.f.u. Boron contents vary from 33–61 µg/g and [Li] from 6–38 µg/g. There is a positive correlation between [B] and [N] with average [N]/[B] ~4.5 (Figure 4).

Sample JEN12-09 contains phengite with a large range of Si contents from 6.50–6.88 p.f.u., Na/(Na+K) from 0.03–0.11, and a negative correlation between Si p.f.u. and Na/(Na+K) (Figure 3). Nitrogen contents vary from 22–127 µg/g, [B] from 29–64 µg/g, and [Li] from 16–42 µg/g. There are no correlations between trace and major element concentrations.

[Figure 3 about here.]

[Figure 4 about here.]

4.2. N, B, Li concentrations in other minerals

Clinopyroxene, amphibole, epidote, titanite and garnet contain <5 µg/g N and B in all samples (see supplementary data). Garnet, epidote and titanite also contain <5 µg/g Li. Clinopyroxene and amphibole are significant hosts of Li varying from 46–142 µg/g in clinopyroxene, and 6–71 µg/g in amphibole. The N content of chlorite is variable between different samples. Chlorite which occurs in cracks and on the rims of garnet contains no detectable N, K or Na (JEN12-07, JEN12-09, SEC16-1, LC-2a). Chlorite which occurs in the matrix of sample JEN12-03 contains 10-83 µg/g N

and minor amounts of K (up to 0.32 wt%) and Na (up to 0.13 wt%). Coexisting phengite contains 108–270 µg/g N. Chlorite in all samples contains <5 µg/g B, and 29–140 µg/g Li but neither varies systematically with textural setting like N.

4.3. Bulk nitrogen contents

Bulk N contents of each sample were calculated to assess the variability of N contents in different protoliths (Table 1). For each sample, we combine the mean N concentration in each N-bearing phase with the modal abundance of that phase, and use a weighted average to calculate the bulk N concentration. The standard errors on mean mineral N concentrations are larger than the analytical uncertainty for all samples except LC-3, which indicates that variation in N concentrations is due to heterogeneity between grains, rather than analytical uncertainty. Mineral modes were estimated by point counting 500 points on representative back scattered electron or optical photomicrographs of each sample, using the software JMicroVision. Absolute uncertainties on mineral modes are calculated as $\sqrt{x}/x$, where x is the number of points. Bulk N contents range from 1.2–71 µg/g. Standard errors on mineral modes and N concentrations were propagated to calculate the uncertainty in bulk N contents.

[Table 1 about here.]

5. Discussion

5.1. Residency of nitrogen and implications for global N recycling

Nitrogen typically occurs as NH_4^+ in crustal rocks, where it substitutes for K^+ in K-bearing minerals such as micas, and to a lesser extent for Na^+ and Ca^{2+} in minerals such as plagioclase (Honma and Itihara, 1981). White mica is the dominant K-bearing phase in most high pressure metabasaltic and metapelitic rocks up to ~9.5 GPa, 750–1000°C (Poli and Schmidt, 2002; Domanik and Holloway, 1996). Previous studies have used correlations between bulk K_2O and N contents to identify white micas as the main host for N (e.g. Bebout et al., 2013; Busigny et al., 2003a) in these rocks. Halama et al. (2010) reported bulk N concentrations for the three Raspas samples in

this study. These values are consistent with our estimated bulk concentrations based on mineral modes (Table 1), which confirms that most N is hosted within the analysed minerals and not along grain boundaries or in fluid inclusions. Most samples contain a single white mica phase (phengite or paragonite), which is the dominant N-bearing phase in the sample. Sample SEC16-1 contains coexisting phengite (117–243 µg/g N) and paragonite (31–118 µg/g N), where N is preferentially partitioned into phengite. This is consistent with the large ionic radius of NH_4^+ (1.67 Å), which is closer to that of K^+ (1.64 Å) than Na^+ (1.39 Å) (Shannon, 1976; Sidey, 2016), and with previous data on the nitrogen partitioning between Na- and K-bearing minerals (Honma and Itihara, 1981). Nitrogen content of white micas is uncorrelated with Na/(Na+K) in most samples, which suggests that small variations in white mica Na/(Na+K) ratio do not exert a strong control on N partitioning behaviour.

[Table 2 about here.]

Our data suggest that white mica hosts >90% of the total N in all but two samples (LC-1b and JEN12-03). Omphacite, glaucophane/barroisite and epidote contain <5 µg/g N in all samples. Omphacite and/or glaucophane are the next most significant N hosts after mica due to their large modal abundance in most samples. Calculated inter-mineral partition coefficients for B and Li (Table 2) are similar to previously published values (Marschall et al., 2006), which indicates that our values represent equilibrium partitioning and that our samples therefore can be used to investigate N partitioning. Partitioning values for N are variable between samples, due to the high N variability in phengite and the low N concentration in other minerals, but broadly indicate that N partitions strongly into phengite compared to other phases. Bulk K content controls white mica mode in metabasic rocks, and since N strongly partitions into white mica over other phases, the K content will exert a strong control on the N budget of subducted oceanic crust. Figure 5 shows that reconstructed bulk K and N contents for mafic samples fall on a positive trend, with average N (µg/g)/K_2O (wt%) = 19.3 ± 2.0. The metachert sample LC-3 plots as an outlier. N/K_2O for subducted mafic rocks is an order of magnitude lower than for metasedimentary rocks (N/K_2O ~200, Busigny et al. (2003a)). Our samples are representative of the basaltic upper oceanic crust, which

has undergone hydrothermal alteration on the seafloor and subsequently been subducted. Using N/K_2O we can estimate the flux of N subducted in upper oceanic crust from the K_2O content and the mass of crust subducted each year (2×10^{16} g/yr, Peacock (1990)). If we assume all basaltic crust has a MORB-like K_2O content (0.16 wt% K_2O, Gale et al. (2013)), we calculate a flux of $6.2 \pm 0.6 \times 10^{10}$ g/yr using our average N/K_2O value of 19.3 ± 2.0. For average altered oceanic crust (AOC, 0.62 wt% K_2O, Kelley et al. (2018)) we calculate $2.4 \pm 0.2 \times 10^{11}$ g/yr. Busigny et al. (2011) calculated a N flux of 1.3×10^{11} g/yr for upper oceanic crust, based on the average N content of metabasalts, which is similar to our value assuming AOC but larger than our value assuming MORB-like crust. All our estimates are somewhat smaller than the flux attributed to subducted sediments (7.4×10^{11} g/yr, Busigny et al. (2003a)).

[Figure 5 about here.]

The only non-mica mineral with significant N is chlorite, for which N contents vary with textural setting. Chlorite forming rims around garnet contains very low [N] (typically <5 µg/g). This is consistent with it forming from retrograde breakdown of garnet, which contains <1 µg/g N. Chlorite which occurs in the matrix alongside N-rich phengite contains 10-83 µg/g N (sample JEN12-03). Chlorite from JEN12-03 also contains minor amounts of K + Na (Figure 6). Incorporation of minor K and Na in chlorite crystals by interlayering of chlorite and K-bearing phyllosilicates at the nanometre scale has been investigated in diagenesis and sub-greenschist facies metamorphism of mudstones and volcaniclastic sediments (Lee et al., 1984; Ahn et al., 1988). It is possible that this mechanism is partially responsible for incorporation of K, Na and N in our chlorites, but N/K_2O is much higher in chlorite than in co-existing phengite (chl: 370, phe: 18), which suggests excess N in the chlorite structure itself. Chlorite is structurally similar to the K and Na-bearing micas, with both minerals containing large interlayer cation sites. In micas these are filled by K^+ and Na^+ cations, whereas in chlorite they are vacant. A possible substitution reaction for N incorporation into chlorite is $NH_3\,(\text{fluid}) + OH^- \longrightarrow {NH_4}^+ + {O^{2-}}$, where ${NH_4}^+$ is incorporated in the vacant interlayer sites.

[Figure 6 about here.]

Chlorite is common in greenschist facies rocks across a wide range of bulk compositions and therefore could potentially play an important role in subduction zone N cycling. However, it has received little previous attention as a possible host for N. Low-grade pelitic schists from the Erzgebirge massif displayed weak correlations between either chlorite or white mica mode and bulk N content, but a strong correlation between chlorite + white mica mode and bulk N content (Mingram and Bräuer, 2001), which supports chlorite being an important host for N. Chlorite also occurs in chlorite harzburgites, formed during serpentinite dehydration. Serpentinites typically have bulk N concentrations <5 µg/g (Halama et al., 2014; Philippot et al., 2007), but one chlorite harzburgite studied by Halama et al. (2014) has elevated N contents (~20 µg/g), which may be consistent with a role for chlorite as a host of N. More research is required to investigate the importance of chlorite as a host for N in different lithologies and the mechanism of N incorporation in chlorite.

5.2. Fluid rock interaction: a simple system

Sample LC-3 (Lago di Cignana garnet-phengite quartzite) was part of a previous study by Halama et al. (2020), who showed a strong positive correlation of B concentration and B isotopic composition, which was interpreted as resulting from addition of isotopically heavy B during peak metamorphic fluid-rock interaction with a serpentinite-derived fluid. We extend the fluid-rock interaction modelling approach of Halama et al. (2020) to include [Li] and [N] data and estimate the phengite-fluid partition coefficient for N. We modified the equation of Nabelek (1987) for open system fluid-rock interaction to replace the concentration of an element in the rock, with the concentration in phengite, multiplied by the modal abundance of phengite:

$$C^f_{phe} = DC_w - (DC_w - C^i_{phe})\ e^{-n/Dx_{phe}}$$

C^f_{phe} is the final concentration of the trace element in the phengite, C^i_{phe} is the initial concentration in the phengite, C_w is the concentration in the fluid, n is the fluid-rock ratio (by weight), x_{phe} is the modal abundance of phengite (33%), and D is the phengite-fluid partition coefficient. For B we use a partition coefficent of 0.7 (Marschall et al., 2006). We used an initial B concentration in the phengite of 50 µg/g and concentration in the fluid of 1000 µg/g, based on the preferred interpreta-

tion of addition of B from a serpentinite-derived, B-rich fluid (Halama et al., 2020). Marschall et al. (2006) reported a subsolidus partition coefficient for Li of 0.05, although higher values of 1 have been reported for suprasolidus experiments (Adam et al., 2014). We evaluate two different scenarios here to model the Li and B data and will subsequently use these constraints to model the combined [N]-[B] and [N]-[Li] data. For $D_{Li}^{phe-fl} = 0.05$, the [B]-[Li] data can be fitted using a Li concentration in the fluid of 800–1000 µg/g, and initial Li concentration in the phengite of 60–120 µg/g (Figure 7). For larger values of $D_{Li}^{phe-fl} = 0.5 - 1$, the [B]-[Li] data can be fitted with $[Li]_w = 0 - 20$ g/g and $[Li]_{phe}^{i} \approx 65$ g/g. Serpentinites typically contain <10 µg/g Li (Deschamps et al., 2012; Kodolányi et al., 2012; Lafay et al., 2013; Vils et al., 2008), and fluid inclusions representing serpentinite dehydration fluids also have <10 µg/g Li in both experiments and natural samples (Spandler et al., 2014; Scambelluri et al., 2004). Serpentinite-derived fluids are therefore expected to have low Li contents and the second scenario, with a value of $D_{Li}^{phe-fl} = 0.5 - 1$ is preferred. To model the [N]-[Li] data we therefore use $D_{Li}^{phe-fl} = 0.5$, $[Li]_w = 0$ g/g and $[Li]_{phe}^{i} = 65$ g/g, which allows the maximum range of D_{N}^{phe-fl} values that are consistent with the data.

To model the N data we consider a variety of theoretical scenarios and evaluate which are consistent with our data and independent constraints on fluid compositions. The [N]-[Li] data display a positive slope, which can be fitted with $[N]_w = 0$ g/g, $D_{N}^{phe-fl} = 0.5 - 1.5$ and $[N]_{phe}^{i} = 17 - 20$ g/g (Figure 7). These parameters also fit the [N]-[B] data. $D_{N}^{phe-fl} > 1.5$ is not consistent with the slope of the [N]-[Li] array for any range of other parameters. There is a trade-off between D and the concentration in the fluid, such that smaller values of D_{N}^{phe-fl} are consistent with the data if the fluid contains nitrogen (e.g. $D_{N}^{phe-fl} = 0.2$, $[N]_w = 50$ g/g). There are no data available on the N contents of fluids derived from serpentinite breakdown, but bulk serpentinites contain <15 µg/g N, and typically <5 µg/g N (Halama et al., 2014; Philippot et al., 2007). The major pulse of fluid release in serpentinites occurs during antigorite breakdown at 600–650 °C, which coincides with the P-T conditions inferred for fluid-rock interaction in this sample (Halama et al., 2020). The amount of fluid release is 6–13 wt%, depending on the serpentinite composition (Padrón-Navarta et al., 2013; Ulmer and Trommsdorff, 1995). Fluid release occurs over a narrow temperature interval so all fluid is likely to be pooled. Chlorite harzburgites produced from antigorite breakdown show a

similar range of N contents to serpentinites (Halama et al., 2014), which suggests that the amount of N released during antigorite breakdown is relatively small. Based on these constraints we suggest that N contents in serpentinite-derived fluids are likely <100 µg/g, and may be much lower. Using this N concentration in the fluid, a lower bound of $D_N^{phe-fl} = 0.1$ is the minimum value of D_N^{phe-fl} which is consistent with the [N]-[Li] and [N]-[B] data. For a lower value of 10 µg/g N in the fluid, the data are fit by $D_N^{phe-fl} = 0.3$.

With $D_N^{phe-fl} = 0.1 - 1.5$ all the data can be explained by fluid-rock ratios of up to 0.1, which is similar to the values of 0.1–0.13 obtained from B isotope modelling (Halama et al., 2020). Note these values have been rescaled from the Halama paper because the effect of the modal abundance of phengite on modifying the bulk rock equations was not accounted for. A value of $D_N^{phe-fl} = 0.1 - 1.5$ is therefore considered the most consistent with our data and fluid composition constraints.

[Figure 7 about here.]

The reconstructed bulk N content for this garnet-phengite quartzite (sample LC-3) is 5 µg/g (Table 1). Siliceous ooze and chert, which are considered the likely protoliths, contain 18–78 µg/g bulk N in samples from the Western Pacific (Sadofsky and Bebout, 2004). If these values are taken as representative then this suggests that N was lost during subduction, consistent with the conclusions from our fluid-rock interaction modelling.

Reported subsolidus values for D_N^{phe-fl} range from 0.01 to ~10, depending on the experimental conditions (Table 3). Pöter et al. (2004) reported $D_{NH_4^+}^{muscovite-fluid} \approx 0.13$ at 0.4 GPa and $D_{NH_4^+}^{mu-fl} \approx 0.20$ at 1.5 GPa in the temperature range 400–600 °C. More recent experiments have focused on the partitioning behaviour at higher temperatures, during melting, but have produced substantially differing results in different experimental bulk compositions. Förster et al. (2019) report $D_{NH_4^+}^{phengite-fluid} \approx 10$ at 2 GPa, 750 °C (subsolidus) and 0.5–1 at 3 GPa, 800–850 °C (suprasolidus) during reaction of a metapelitic melt with dunite. Jackson et al. (2021) report $D_{NH_4^+}^{biotite-fluid}$=0.01–0.4 at 0.2–2.3 GPa, 725–925 °C during reaction of silicate minerals with hydrous fluids. NH_4^+ has also previously been assumed to behave similarly to Rb^+ (e.g. Mallik et al., 2018; Busigny et al., 2003a), which has a similar ionic radius (NH_4^+: 1.67 Å, Rb^+: 1.72 Å), and a D_{Rb}^{phe-fl} value of ~4–10

(Adam et al., 2014; Melzer and Wunder, 2000).

Our value of $D_N^{phe-fl} = 0.1 - 1.5$ overlaps with the suprasolidus values of Förster et al. (2019). However, it is inconsistent with a single subsolidus value ($D_N^{phe-fl} = 10$) of Förster et al. (2019). and with the values of 4–10, based on the assumption that NH_4^+ behaves like Rb^+. Jackson et al. (2021) provide small values for $D_N^{biotite-fl}$ (0.01–0.4), which are mostly inconsistent with our value for D_N^{phe-fl}, when considering the consistent $D_N^{bi-phe} \approx 3$ reported by all studies. The subsolidus values of Pöter et al. (2004) ($D_N^{phe-fl} = 0.12 - -0.2$) fall at the bottom end of the range of values which are consistent with our data. The experimental data are either from similar temperatures but lower pressures to the Cignana case study (Pöter et al., 2004), or similar pressures but higher temperatures (Förster et al., 2019; Jackson et al., 2021). Extrapolation of the P-T effects reported by the Jackson study does not match our value for D_N^{phe-fl}, and therefore differences in P-T conditions are less likely to be the main factor for the discrepancy between our value and their work. Experimental and natural values for D_N^{phe-bi} are relatively consistent between multiple studies at different P-T conditions, whereas experimental values for D_N^{phe-fl} vary widely (Table 3), which suggests that variation may be a result of fluid-related factors. The difficulty of preserving N contents of experimental fluids during quenching may be a source of variation in the experimental results (e.g. Chen et al., 2019). Nitrogen is present as NH_4^+ in both biotite and phengite, whereas N speciation in fluid varies between N_2, NH_3 and NH_4^+, depending on P, T, pH and fO_2 (Mikhail and Sverjensky, 2014; Mikhail et al., 2017) and therefore differences in fluid pH and fO_2 between experiments, and between experiments and our samples, are also possible reasons for the discrepancy.

[Table 3 about here.]

5.3. Fluid-rock interaction: growth of new phases

Sample SEC16-1 (Raspas blueschist) contains phengite as well as paragonite. As both minerals are significant hosts for N and B, phengite compositions cannot be considered in isolation. Phengites show a decrease in [N] and [B] with decreasing Si p.f.u., an increase in [Li], as well as a increase in Na/(Na+K) (i.e. its paragonite component) whereas paragonite shows unsystematic variation in these elements (Figure 3).

We performed equilibrium phase diagram modelling in order to understand the mineralogical evolution of this sample and link this to the trace element behaviour. Calculations were performed using the Theriak-Domino software (de Capitani and Brown, 1987; de Capitani and Petrakakis, 2010) and the NCKFMASHTO + CO_2 system using an H_2O-CO_2 fluid in excess and the Holland and Powell (2011) thermodynamic database. The solution models used were: amphibole, clinopyroxene, white mica (Green et al., 2016); garnet, biotite, chlorite (White et al., 2014); epidote (Holland and Powell, 2011).

We calculated P-X(CO_2) and T-X(CO_2) equilibrium phase diagrams with variable X(CO_2) from 0 to 0.025, using the bulk composition for this sample reported in John et al. (2010) and an average MORB value of $X_{Fe^{3+}} = 0.16$ (Cottrell and Kelley, 2011). The effect of varying $X_{Fe^{3+}}$ from 0.05–0.25 moved field boundaries by only <1 kbar for all phases except epidote and therefore $X_{Fe^{3+}} = 0.16$ is considered suitable for this sample.

The observed assemblage occupies a field ranging from 1.5–1.9 GPa, 520–570 °C and X(CO_2) from 0.010–0.022 (Figure 8). This field is bounded by the disappearance of paragonite as X(CO_2) decreases, and the disappearance of garnet and epidote as X(CO_2) increases. John et al. (2010) previously calculated peak P-T conditions for the Raspas complex using conventional thermobarometry on garnet-omphacite-phengite assemblages. Peak P-T conditions of eclogites were 1.6–2.0 GPa and 550–650 °C. Garnet-omphacite-phengite domains in blueschists recorded slightly lower peak pressures of 1.4–1.6 GPa and similar temperatures. According to our modelling, omphacite is only stable under these conditions at lower values of X(CO_2) than are required to stabilise the observed blueschist assemblage, which has 16% paragonite. As mentioned above, the sample contains carbonate, and addition of CO_2 to the system stabilises paragonite. As X(CO_2) increases across the observed assemblage field, the paragonite mode increases from 0 to 25%, and glaucophane mode decreases from 40 to 15% due to the (unbalanced) reaction glaucophane + CO_2 $\longrightarrow$ paragonite + (Fe,Mg,Ca) carbonate. The high paragonite mode observed in the sample can therefore be explained as a result of infiltration of a carbonate-bearing fluid.

As X(CO_2) increases across the peak assemblage field, phengite Na/(Na+K) increases and Si content decreases. Phengite mode remains fairly constant, decreasing slightly from 16 to 14%. A

range of phengite Si contents are observed in different phengite grains. These are interpreted as representing partial recrystallisation of phengite during interaction with a carbonate-bearing fluid, with the new domains having lower Si p.f.u. and higher Na p.f.u.. Trace element redistribution from other phases into phengite supports our interpretation. For example, the Li contents in phengite, which correlate with decreasing Si p.f.u., can be interpreted to reflect incorporation of Li from glaucophane breakdown, since glaucophane has high Li contents (132–169 µg/g). Although the preservation of variable phengite Si contents implies that full equilibrium was not reached during fluid-rock interaction (i.e. the reactant phases were not totally consumed), the assemblage, major and trace element data support the conclusion that interaction with a CO_2-bearing fluid occurred, likely during early retrograde metamorphism.

[Figure 8 about here.]

Decrease in phengite N content in SEC16-1 also correlates with decreasing Si content and increasing Na/(Na+K). This can be explained by the phengite recrystallisation discussed above. During paragonite growth, partial re-equilibration of phengite with the growing paragonite results in transfer of N from phengite to paragonite. Taking the phengite with the highest Si content to represent the initial phengite composition prior to fluid-rock interaction, we use the N content of this phengite (232 µg/g) to calculate the initial bulk N concentration of the sample. To calculate the final bulk N concentration we use the average N concentrations of all phengite and paragonite grains measured (190 and 53 µg/g respectively). The observed phengite and paragonite modes are around 16%. Using the method described in Section 4.3 we calculate the bulk N contents before and after fluid-rock interaction. The final bulk N content is 39 µg/g. For the conservative assumption that the phengite mode does not change during fluid-rock interaction, the initial bulk N is 37 µg/g. Accounting for the modelled decrease in phengite mode from 16 to 14%, the initial bulk is 42 µg/g. The decrease in N concentration seen in phengite in this sample can therefore be explained by redistribution of N between growing and dissolving phases during fluid-rock interaction, without any significant external input or loss of N from the rock. The uncertainty on the bulk [N] values was estimated to be ~15–20% by combining uncertainties on the mineral N concentrations and

mineral modes. This conclusion is similar to Halama et al. (2017), who showed that the retention of N during fluid-rock interaction is strongly controlled by the stability or breakdown of white mica. A similar reaction (albite + CO_2 $\longrightarrow$ paragonite + aragonite) observed in calcschists from the Western Alps was associated with 60% loss of N from the bulk rock, with volumetric fluid-rock ratios of 3–4 (Epstein et al., 2021). The difference in N behaviour compared to our study may be explained by a lower fluid-rock ratio, or a different fluid composition. If we assume that the $X(CO_2)$ values which stabilise the observed assemblage (Figure 8) are representative of the fluid, and that all the CO_2 in the fluid was converted to carbonate minerals, we can estimate the minimum amount of fluid required to generate the modal abundance of carbonate observed. Using $X(CO_2)$=0.01–0.022 and a carbonate mode of 3–5 vol% gives a fluid-rock ratio of 0.2–0.9, which is indeed lower than for the Epstein study.

Phengite and paragonite are also the main B-bearing phases, so the same model can be applied to B as with N. The decrease in B contents with decreasing Si contents can be explained by redistribution of B into paragonite. The calculated final bulk B concentration is 28 µg/g, compared to an initial concentration of 15-17 µg/g depending on the estimate of the phengite mode. This suggests that in contrast with N, B has been added to the rock during fluid-rock interaction. This may explain why there is more scatter in the correlation of [B] with Si p.f.u., compared to [N], as individual grains have equilibrated to differing degrees with a B-rich fluid (Konrad-Schmolke and Halama, 2014; Halama et al., 2020).

5.4. Fluid-rock interaction in other samples

Calculated bulk N concentrations in Cignana mafic rocks (samples LC-2a, LC-1b) are very low. Sample LC-1b (1.2 µg/g N) falls within the range of N contents observed in fresh MORB, which is generally <2 µg/g (Li et al., 2007; Busigny et al., 2005; Erzinger et al., 1996). Sample LC-2a has slightly higher N contents (3.6 µg/g), which may reflect a more hydrothermally altered protolith (Busigny et al., 2005; Li et al., 2007), or addition of minor N during subduction.

Sample LC-2a preserves variability in phengite major and trace element chemistry. The main population has constant Si p.f.u. but variable N contents (39–123 µg/g). There are two grains with

higher, variable Si content, lower N (20–24 µg/g) and Li contents, and higher B content. The Si contents of these grains overlap with those from sample LC-3, which were interpreted to record peak metamorphism. Halama et al. (2020) previously interpreted B isotope data from LC-2a to suggest that B was lost during retrograde fluid-rock interaction. The observed lower B contents and lower Si contents in our analyses are consistent with this interpretation, where the low Si grains formed during retrograde recrystallization and the high Si grains preserve peak conditions. The elevated N and Li contents in low Si grains suggest that small amounts of N and Li were added during retrograde fluid-rock interaction.

Previous studies on eclogites and blueschists from Jenner have suggested a complex metamorphic history involving interaction with both sediment-derived (Sorensen et al., 1997; Penniston-Dorland et al., 2010) and serpentinite-derived fluids (Errico et al., 2013). Jenner samples show high bulk N contents (13–71 µg/g) compared to the range of both fresh MORB (< 2 µg/g) and altered oceanic crust (1–30 µg/g, Li et al. (2007); Busigny et al. (2005)). The N concentrations in individual phengite grains are similar to those from Raspas, but the Jenner samples contain higher phengite modes, resulting in higher bulk N contents. High phengite mode is consistent with the bulk enrichment in K and other large ion lithophile elements documented by Sorensen et al. (1997) and attributed to interaction with a sediment-derived fluid. High N contents are also consistent with a sediment-derived fluid, since subducted sediments can have N contents up to 2000 µg/g (e.g. Sadofsky and Bebout, 2004; Li and Bebout, 2005). The positive correlation of N and B contents in phengite in samples JEN12-03 and JEN12-07 is also consistent with a sediment derived fluid, since sediments can also contain high B contents (e.g. Romer et al., 2014; Bebout et al., 2013; De Hoog and Savov, 2018). Negative correlation of [N] and [Li] in JEN12-07 and JEN12-09 suggests that these sediment-derived fluids may be Li-poor.

These samples demonstrate that addition of N during metamorphism appears to be a common process in subduction-related mafic rocks, in agreement with recent work which found that N addition can occur as early as blueschist facies (Li et al., 2021). These fluids are most likely sourced from dehydrating metasediments, as these are rich in N. Addition of N can be associated with either addition or loss of Li and B, which suggests that these fluids can be heterogeneous in their Li and

B contents, possibly reflecting heterogeneity in the sediments themselves. Addition of N is seen in phengite with high Si contents, which implies that it occurred during deep subduction and is not a late-stage retrograde overprint. The presence of N and other fluid-mobile elements in sediment-derived fluids at depths of up to ~90 km (in the case of Cignana, see our modelling in Section 5.2) implies that these elements are at least partially retained to that depth, and can be mobilised and redistributed there, rather than being completely lost during shallow dehydration reactions. This emphasises the importance of understanding volatile element transfer between lithologies during subduction, not just the effects of prograde devolatilisation, and shows that mafic rocks may act as sinks for N and other volatiles during subduction-related metasomatism, if accompanied by growth of mica.

6. Conclusions

This study demonstrates the viability of *in situ* analyses of N in silicate minerals using SIMS. The data collected from a range of formerly subducted rocks show that N is dominantly hosted in white micas, compared to phases such as omphacite or Na-amphibole. Chlorite may have an additional role as a N host but more data are required to explore its role in a wider variety of localities and lithologies. Reconstructed bulk N contents based on mineral modes and N concentrations agree with bulk N contents measured by combustion, which confirms that most N is hosted in the major rock-forming minerals. Using the N/K_2O ratio in white micas, and the K-content of the subducted slab, we estimate the subducted flux of N in oceanic crust to be $0.6 - 2.4 \times 10^{11}$ g/yr, which is similar to or slightly smaller than previous estimates. A case study of fluid-rock interaction in a mineralogically simple garnet-phengite quartzite shows moderate N loss during fluid-rock interaction. Using open system fluid-rock interaction equations we show that N is a moderately fluid-mobile element under the P-T-X conditions experienced by this sample ($D_N^{phe-fl} = 0.1 - 1.5$). A second fluid-rock interaction case study shows the importance of white mica stability in controlling the N budget of rocks. White mica growth during fluid-rock interaction can sequester N and prevent significant bulk N loss. Our work provides constraints on the inter-mineral partitioning of N at subduction zone conditions and provides the first natural constraints on the fluid-mineral

partitioning of N at these conditions. We emphasise the complexity of element mobility within subduction zones, with redistribution between different phases and lithologies being important, in addition to simple loss of volatiles during dehydration.

7. Acknowledgements

We thank M. Konrad-Schmolke for expert guidance at Jenner, T. John for assistance with Raspas samples, D. Wilde for help with sample preparation and I. Buisman for electron probe analyses. We also thank S. Mikhail, L. Li and an anonymous reviewer for comments which improved this manuscript. This work was supported by a NERC Doctoral Training Partnership grant (NE/S007407/1) and a NERC Ion Microprobe Facility grant (IMF709/0520).

References

Adam, J., Locmelis, M., Afonso, J.C., Rushmer, T., Fiorentini, M.L., 2014. The capacity of hydrous fluids to transport and fractionate incompatible elements and metals within the Earth's mantle. Geochemistry, Geophysics, Geosystems 15, 2241–2253. doi:https://doi.org/10.1002/2013GC005199.

Ahn, J.H., Peacor, D.R., Coombs, D.S., 1988. Formation mechanisms of illite, chlorite and mixed-layer illite-chlorite in Triassic volcanogenic sediments from the Southland Syncline, New Zealand. Contributions to Mineralogy and Petrology 99, 82–89. doi:10.1007/BF00399368.

Anczkiewicz, R., Platt, J.P., Thirlwall, M.F., Wakabayashi, J., 2004. Franciscan subduction off to a slow start: evidence from high-precision Lu–Hf garnet ages on high grade-blocks. Earth and Planetary Science Letters 225, 147–161. doi:10.1016/j.epsl.2004.06.003.

Arculus, R.J., Lapierre, H., Jaillard, , 1999. Geochemical window into subduction and accretion processes: Raspas metamorphic complex, Ecuador. Geology 27, 547–550. doi:10.1130/0091-7613(1999)027<0547:GWISAA>2.3.CO;2.

675 Avice, G., Marty, B., Burgess, R., Hofmann, A., Philippot, P., Zahnle, K., Zakharov, D., 2018.
676 Evolution of atmospheric xenon and other noble gases inferred from Archean to Paleoproterozoic
677 rocks. Geochimica et Cosmochimica Acta 232, 82–100. doi:10.1016/j.gca.2018.04.018.

678 Barry, P., Hilton, D.R., 2016. Release of subducted sedimentary nitrogen throughout Earth's
679 mantle. Geochemical Perspectives Letters 2.

680 Bebout, G.E., Agard, P., Kobayashi, K., Moriguti, T., Nakamura, E., 2013. Devolatilization history
681 and trace element mobility in deeply subducted sedimentary rocks: Evidence from Western Alps
682 HP/UHP suites. Chemical Geology 342, 1–20. doi:10.1016/j.chemgeo.2013.01.009.

683 Bebout, G.E., Bebout, A.E., Graham, C.M., 2007. Cycling of B, Li, and LILE (K, Cs, Rb, Ba, Sr)
684 into subduction zones: SIMS evidence from micas in high-P/T metasedimentary rocks. Chemical
685 Geology 239, 284–304. doi:10.1016/j.chemgeo.2006.10.016.

686 Bebout, G.E., Fogel, M.L., 1992. Nitrogen-isotope compositions of metasedimentary rocks in the
687 Catalina Schist, California: Implications for metamorphic devolatilization history. Geochimica
688 et Cosmochimica Acta 56, 2839–2849. doi:10.1016/0016-7037(92)90363-N.

689 Berner, R.A., 2006. Geological nitrogen cycle and atmospheric N2 over Phanerozoic time. Geology
690 34, 413–415. doi:10.1130/G22470.1.

691 Busigny, V., Cartigny, P., Philippot, P., 2011. Nitrogen isotopes in ophiolitic metagabbros: A
692 re-evaluation of modern nitrogen fluxes in subduction zones and implication for the early Earth
693 atmosphere. Geochimica et Cosmochimica Acta 75, 7502–7521. doi:10.1016/j.gca.2011.09.
694 049.

695 Busigny, V., Cartigny, P., Philippot, P., Ader, M., Javoy, M., 2003a. Massive recycling of nitrogen
696 and other fluid-mobile elements (K, Rb, Cs, H) in a cold slab environment: evidence from HP to
697 UHP oceanic metasediments of the Schistes Lustrés nappe (western Alps, Europe). Earth and
698 Planetary Science Letters 215, 27–42. doi:10.1016/S0012-821X(03)00453-9.

699 Busigny, V., Cartigny, P., Philippot, P., Javoy, M., 2003b. Ammonium quantification in muscovite
700 by infrared spectroscopy. Chemical Geology 198, 21–31. doi:10.1016/S0009-2541(02)00420-5.

701 Busigny, V., Cartigny, P., Philippot, P., Javoy, M., 2004. Quantitative analysis of ammonium
702 in biotite using infrared spectroscopy. American Mineralogist 89, 1625–1630. doi:10.2138/
703 am-2004-11-1206.

704 Busigny, V., Laverne, C., Bonifacie, M., 2005. Nitrogen content and isotopic composition of oceanic
705 crust at a superfast spreading ridge: A profile in altered basalts from ODP Site 1256, Leg 206.
706 Geochemistry, Geophysics, Geosystems 6. doi:https://doi.org/10.1029/2005GC001020.

707 de Capitani, C., Brown, T.H., 1987. The computation of chemical equilibrium in complex systems
708 containing non-ideal solutions. Geochimica et Cosmochimica Acta 51, 2639–2652. doi:10.1016/
709 0016-7037(87)90145-1.

710 de Capitani, C., Petrakakis, K., 2010. The computation of equilibrium assemblage diagrams with
711 Theriak/Domino software. American Mineralogist 95, 1006–1016. doi:10.2138/am.2010.3354.

712 Chen, Q., Zhang, Z., Wang, Z., Li, W.C., Gao, X.Y., Ni, H., 2019. In situ Raman spectroscopic
713 study of nitrogen speciation in aqueous fluids under pressure. Chemical Geology 506, 51–57.
714 doi:10.1016/j.chemgeo.2018.12.016.

715 Clarke, E., De Hoog, J.C.M., Kirstein, L., Harvey, J., Debret, B., 2020. Metamorphic olivine records
716 external fluid infiltration during serpentinite dehydration. Geochemical Perspectives Letters 16,
717 25–29. doi:10.7185/geochemlet.2039.

718 Cottrell, E., Kelley, K.A., 2011. The oxidation state of Fe in MORB glasses and the oxygen fugacity
719 of the upper mantle. Earth and Planetary Science Letters 305, 270–282. doi:10.1016/j.epsl.
720 2011.03.014.

721 Dal Piaz, G.V., Venturelli, G., Spadea, P., Di Battistini, G., 1981. Geochemical features of
722 metabasalts and metagabbros from the Piemonte ophiolite nappe, Italian Western Alps. Geo-

chemical features of metabasalts and metagabbros from the Piemonte ophiolite nappe, Italian Western Alps 142, 248–269.

De Hoog, J.C.M., Hattori, K., Jung, H., 2014. Titanium- and water-rich metamorphic olivine in high-pressure serpentinites from the Voltri Massif (Ligurian Alps, Italy): evidence for deep subduction of high-field strength and fluid-mobile elements. Contributions to Mineralogy and Petrology 167. doi:10.1007/s00410-014-0990-x.

De Hoog, J.C.M., Savov, I.P., 2018. Boron Isotopes as a Tracer of Subduction Zone Processes, in: Marschall, H., Foster, G. (Eds.), Boron Isotopes: The Fifth Element, Cham. Advances in Isotope Geochemistry, pp. 217–247. doi:10.1007/978-3-319-64666-4_9.

Debret, B., Koga, K.T., Cattani, F., Nicollet, C., Van den Bleeken, G., Schwartz, S., 2016. Volatile (Li, B, F and Cl) mobility during amphibole breakdown in subduction zones. Lithos 244, 165–181. doi:10.1016/j.lithos.2015.12.004.

Deschamps, F., Godard, M., Guillot, S., Chauvel, C., Andreani, M., Hattori, K., Wunder, B., France, L., 2012. Behavior of fluid-mobile elements in serpentines from abyssal to subduction environments: Examples from Cuba and Dominican Republic. Chemical Geology 312-313, 93–117. doi:10.1016/j.chemgeo.2012.04.009.

Domanik, K.J., Holloway, J.R., 1996. The stability and composition of phengitic muscovite and associated phases from 5.5 to 11 GPa: Implications for deeply subducted sediments. Geochimica et Cosmochimica Acta 60, 4133–4150. doi:10.1016/S0016-7037(96)00241-4.

Duit, W., Jansen, J.B.H., Breemen, A.v., Bos, A., 1986. Ammonium micas in metamorphic rocks as exemplified by Dome de l'Agout (France). American Journal of Science 286, 702–732. doi:10.2475/ajs.286.9.702.

Dyar, M.D., Wiedenbeck, M., Robertson, D., Cross, L.R., Delaney, J.S., Ferguson, K., Francis, C.A., Grew, E.S., Guidotti, C.V., Hervig, R.L., Hughes, J.M., Husler, J., Leeman, W., McGuire, A.V., Rhede, D., Rothe, H., Paul, R.L., Richards, I., Yates, M., 2001. Reference Minerals for

748 the Microanalysis of Light Elements. Geostandards Newsletter 25, 441–463. doi:10.1111/j.
749 1751-908X.2001.tb00616.x.

750 Epstein, G.S., Bebout, G.E., Angiboust, S., 2021. Fluid and mass transfer along transient sub-
751 duction interfaces in a deep paleo-accretionary wedge (Western Alps). Chemical Geology 559,
752 119920. doi:10.1016/j.chemgeo.2020.119920.

753 Errico, J., Barnes, J., Strickland, A., Valley, J., 2013. Oxygen isotope zoning in garnets from
754 Franciscan eclogite blocks: evidence for rock-buffered fluid interaction in the mantle wedge.
755 Contributions to Mineralogy & Petrology 166, 1161–1176. doi:10.1007/s00410-013-0915-0.

756 Erzinger, J., Bach, W., Alt, J.C., Kinoshita, H., Stokking, L.B., Michael, P.J., 1996. Downhole
757 variation of molecular nitrogen in DSDP/ODP Hole 504B: preliminary results. Proceedings of the
758 Ocean Drilling Program : Scientific Results 148, 3–8. doi:10.2973/odp.proc.sr.148.156.1996.

759 Feininger, T., 1980. Eclogite and Related High-Pressure Regional Metamorphic Rocks from the
760 Andes of Ecuador. Journal of Petrology 21, 107–140. doi:10.1093/petrology/21.1.107.

761 Förster, M.W., Foley, S.F., Alard, O., Buhre, S., 2019. Partitioning of nitrogen during melting and
762 recycling in subduction zones and the evolution of atmospheric nitrogen. Chemical Geology 525,
763 334–342. doi:10.1016/j.chemgeo.2019.07.042.

764 Füri, E., Deloule, E., Dalou, C., 2018. Nitrogen abundance and isotope analysis of silicate glasses
765 by secondary ionization mass spectrometry. Chemical Geology 493, 327–337. doi:10.1016/j.
766 chemgeo.2018.06.008.

767 Gabriele, P., Ballèvre, M., Jaillard, E., Hernandez, J., 2003. Garnet-chloritoid-kyanite metapelites
768 from the Raspas Complex (SW Ecuador) a key eclogite-facies assemblage. European Journal of
769 Mineralogy 15, 977–989. doi:10.1127/0935-1221/2003/0015-0977.

770 Gale, A., Dalton, C.A., Langmuir, C.H., Su, Y., Schilling, J.G., 2013. The mean composition of
771 ocean ridge basalts. Geochemistry, Geophysics, Geosystems 14, 489–518. doi:https://doi.org/
772 10.1029/2012GC004334.

773 Green, E.C.R., White, R.W., Diener, J.F.A., Powell, R., Holland, T.J.B., Palin, R.M., 2016. Ac-
774 tivity–composition relations for the calculation of partial melting equilibria in metabasic rocks.
775 Journal of Metamorphic Geology 34, 845–869. doi:10.1111/jmg.12211.

776 Groppo, C., Beltrando, M., Compagnoni, R., 2009. The P–T path of the ultra-high pressure
777 Lago Di Cignana and adjoining high-pressure meta-ophiolitic units: insights into the evolution
778 of the subducting Tethyan slab. Journal of Metamorphic Geology 27, 207–231. doi:10.1111/j.
779 1525-1314.2009.00814.x.

780 Guggino, S.N., Hervig, R.L., 2011. Synthesis and Characterization of Five New F-bearing Basalt
781 Reference Materials (Fba Glasses): Quantifying the Fluorine Content of the Basaltic Glass Stan-
782 dards BCR-2G, BHVO-2G. GSA-1G, GSC-1G, GSD-1G, GSE-1G, ML3B-G, KL2-G, and ALV-
783 519-4. AGU Fall Meeting Abstracts 31, V31C–2535.

784 Haendel, D., Mühle, K., Nitzsche, H.M., Stiehl, G., Wand, U., 1986. Isotopic variations of the fixed
785 nitrogen in metamorphic rocks. Geochimica et Cosmochimica Acta 50, 749–758. doi:10.1016/
786 0016-7037(86)90351-0.

787 Halama, R., Bebout, G.E., John, T., Scambelluri, M., 2014. Nitrogen recycling in subducted mantle
788 rocks and implications for the global nitrogen cycle. International Journal of Earth Sciences 103,
789 2081–2099. doi:10.1007/s00531-012-0782-3.

790 Halama, R., Bebout, G.E., John, T., Schenk, V., 2010. Nitrogen recycling in subducted oceanic
791 lithosphere: The record in high- and ultrahigh-pressure metabasaltic rocks. Geochimica et Cos-
792 mochimica Acta 74, 1636–1652. doi:10.1016/j.gca.2009.12.003.

793 Halama, R., Bebout, G.E., Marschall, H.R., John, T., 2017. Fluid-induced breakdown of white
794 mica controls nitrogen transfer during fluid–rock interaction in subduction zones. International
795 Geology Review 59, 702–720. doi:10.1080/00206814.2016.1233834.

796 Halama, R., Konrad-Schmolke, M., De Hoog, J.C.M., 2020. Boron isotope record of peak meta-
797 morphic ultrahigh-pressure and retrograde fluid–rock interaction in white mica (Lago di Cig-

798 nana, Western Alps). Contributions to Mineralogy and Petrology 175, 20. doi:10.1007/
799 s00410-020-1661-8.

800 Holland, T.J.B., Powell, R., 2011. An improved and extended internally consistent thermodynamic
801 dataset for phases of petrological interest, involving a new equation of state for solids. Journal
802 of Metamorphic Geology 29, 333–383. doi:10.1111/j.1525-1314.2010.00923.x.

803 Honma, H., Itihara, Y., 1981. Distribution of ammonium in minerals of metamorphic and granitic
804 rocks. Geochimica et Cosmochimica Acta 45, 983–988. doi:10.1016/0016-7037(81)90122-8.

805 Jackson, C.R.M., Cottrell, E., Andrews, B., 2021. Warm and oxidizing slabs limit ingassing
806 efficiency of nitrogen to the mantle. Earth and Planetary Science Letters 553, 116615.
807 doi:10.1016/j.epsl.2020.116615.

808 Jochum, K.P., Willbold, M., Raczek, I., Stoll, B., Herwig, K., 2005. Chemical Characterisation
809 of the USGS Reference Glasses GSA-1G, GSC-1G, GSD-1G, GSE-1G, BCR-2G, BHVO-2G and
810 BIR-1G Using EPMA, ID-TIMS, ID-ICP-MS and LA-ICP-MS. Geostandards and Geoanalytical
811 Research 29, 285–302. doi:https://doi.org/10.1111/j.1751-908X.2005.tb00901.x.

812 John, T., Scherer, E.E., Schenk, V., Herms, P., Halama, R., Garbe-Schönberg, D., 2010. Subducted
813 seamounts in an eclogite-facies ophiolite sequence: the Andean Raspas Complex, SW Ecuador.
814 Contributions to Mineralogy and Petrology 159, 265–284. doi:10.1007/s00410-009-0427-0.

815 Johnson, B., Goldblatt, C., 2015. The nitrogen budget of Earth. Earth-Science Reviews 148,
816 150–173. doi:10.1016/j.earscirev.2015.05.006.

817 Kelley, K.A., Plank, T., Ludden, J., Staudigel, H., 2018. Composition of altered oceanic crust at
818 ODP Sites 801 and 1149. Geochemistry, Geophysics, Geosystems doi:10.1029/2002GC000435@
819 10.1002/(ISSN)1525-2027.INPUT1.

820 Kodolányi, J., Pettke, T., Spandler, C., Kamber, B.S., Gméling, K., 2012. Geochemistry of Ocean
821 Floor and Fore-arc Serpentinites: Constraints on the Ultramafic Input to Subduction Zones.
822 Journal of Petrology 53, 235–270. doi:10.1093/petrology/egr058.

Konrad-Schmolke, M., Halama, R., 2014. Combined thermodynamic–geochemical modeling in metamorphic geology: Boron as tracer of fluid–rock interaction. Lithos 208-209, 393–414. doi:10.1016/j.lithos.2014.09.021.

Krogh, E.J., Oh, C.W., Liou, J.C., 1994. Polyphase and anticlockwise P-T evolution for Franciscan eclogites and blueschists from Jenner, California, USA. Journal of Metamorphic Geology 12, 121–134. doi:10.1111/j.1525-1314.1994.tb00008.x.

Lafay, R., Deschamps, F., Schwartz, S., Guillot, S., Godard, M., Debret, B., Nicollet, C., 2013. High-pressure serpentinites, a trap-and-release system controlled by metamorphic conditions: Example from the Piedmont zone of the western Alps. Chemical Geology 343, 38–54. doi:10.1016/j.chemgeo.2013.02.008.

Lee, J.H., Peacor, D.R., Lewis, D.D., Wintsch, R.P., 1984. Chlorite-illite/muscovite interlayered and interstratified crystals: A TEM/STEM study. Contributions to Mineralogy and Petrology 88, 372–385. doi:10.1007/BF00376762.

Lesne, P., Kohn, S.C., Blundy, J., Witham, F., Botcharnikov, R.E., Behrens, H., 2011. Experimental Simulation of Closed-System Degassing in the System Basalt–H2O–CO2–S–Cl. Journal of Petrology 52, 1737–1762. doi:10.1093/petrology/egr027.

Li, K., Li, G.Y., Du, Y.F., Han, W., Zhang, J., Chen, L.H., Zhou, J.B., Li, L., 2021. Intraslab remobilization of nitrogen during early subduction facilitates deep nitrogen recycling: Insights from the blueschists in the Heilongjiang Complex in NE China. Chemical Geology 583, 120474. doi:10.1016/j.chemgeo.2021.120474.

Li, L., Bebout, G.E., 2005. Carbon and nitrogen geochemistry of sediments in the Central American convergent margin: Insights regarding subduction input fluxes, diagenesis, and paleoproductivity. Journal of Geophysical Research: Solid Earth 110. doi:10.1029/2004JB003276.

Li, L., Bebout, G.E., Idleman, B.D., 2007. Nitrogen concentration and 15N of altered oceanic crust obtained on ODP Legs 129 and 185: Insights into alteration-related nitrogen enrichment and the

nitrogen subduction budget. Geochimica et Cosmochimica Acta 71, 2344–2360. doi:10.1016/j.gca.2007.02.001.

Li, Y., Huang, R., Wiedenbeck, M., Keppler, H., 2015. Nitrogen distribution between aqueous fluids and silicate melts. Earth and Planetary Science Letters 411, 218–228. doi:10.1016/j.epsl.2014.11.050.

Mallik, A., Li, Y., Wiedenbeck, M., 2018. Nitrogen evolution within the Earth's atmosphere–mantle system assessed by recycling in subduction zones. Earth and Planetary Science Letters 482, 556–566. doi:10.1016/j.epsl.2017.11.045.

Marschall, H.R., Altherr, R., Ludwig, T., Kalt, A., Gméling, K., Kasztovszky, Z., 2006. Partitioning and budget of Li, Be and B in high-pressure metamorphic rocks. Geochimica et Cosmochimica Acta 70, 4750–4769. doi:10.1016/j.gca.2006.07.006.

Martin, C., Ponzevera, E., Harlow, G., 2015. In situ lithium and boron isotope determinations in mica, pyroxene, and serpentine by LA-MC-ICP-MS. Chemical Geology 412, 107–116. doi:10.1016/j.chemgeo.2015.07.022.

Marty, B., Zimmermann, L., Pujol, M., Burgess, R., Philippot, P., 2013. Nitrogen Isotopic Composition and Density of the Archean Atmosphere. Science 342, 101–104. doi:10.1126/science.1240971.

Melzer, S., Wunder, B., 2000. Island-arc basalt alkali ratios: Constraints from phengite-fluid partitioning experiments. Geology 28, 583–586. doi:10.1130/0091-7613(2000)28<583:IBARCF>2.0.CO;2.

Mikhail, S., Barry, P.H., Sverjensky, D.A., 2017. The relationship between mantle pH and the deep nitrogen cycle. Geochimica et Cosmochimica Acta 209, 149–160. doi:10.1016/j.gca.2017.04.007.

Mikhail, S., Sverjensky, D.A., 2014. Nitrogen speciation in upper mantle fluids and the origin of Earth's nitrogen-rich atmosphere. Nature Geoscience 7, 816–819. doi:10.1038/ngeo2271.

873 Mingram, B., Bräuer, K., 2001. Ammonium concentration and nitrogen isotope composition in
874 metasedimentary rocks from different tectonometamorphic units of the European Variscan Belt.
875 Geochimica et Cosmochimica Acta 65, 273–287. doi:10.1016/S0016-7037(00)00517-2.

876 Moine, B., Guillot, C., Gibert, F., 1994. Controls of the composition of nitrogen-rich fluids origi-
877 nating from reaction with graphite and ammonium-bearing biotite. Geochimica et Cosmochimica
878 Acta 58, 5503–5523. doi:10.1016/0016-7037(94)90246-1.

879 Nabelek, P.I., 1987. General equations for modeling fluid/rock interaction using trace elements
880 and isotopes. Geochimica et Cosmochimica Acta 51, 1765–1769. doi:10.1016/0016-7037(87)
881 90354-1.

882 Padrón-Navarta, J.A., Sánchez-Vizcaíno, V.L., Hermann, J., Connolly, J.A.D., Garrido, C.J.,
883 Gómez-Pugnaire, M.T., Marchesi, C., 2013. Tschermak's substitution in antigorite and conse-
884 quences for phase relations and water liberation in high-grade serpentinites. Lithos 178, 186–196.
885 doi:10.1016/j.lithos.2013.02.001.

886 Peacock, S.A., 1990. Fluid Processes in Subduction Zones. Science 248, 329–337. doi:10.1126/
887 science.248.4953.329.

888 Penniston-Dorland, S.C., Sorensen, S.S., Ash, R.D., Khadke, S.V., 2010. Lithium isotopes as a
889 tracer of fluids in a subduction zone mélange: Franciscan Complex, CA. Earth and Planetary
890 Science Letters 292, 181–190. doi:10.1016/j.epsl.2010.01.034.

891 Philippot, P., Busigny, V., Scambelluri, M., Cartigny, P., 2007. Oxygen and nitrogen isotopes as
892 tracers of fluid activities in serpentinites and metasediments during subduction. Mineralogy and
893 Petrology 91, 11–24. doi:10.1007/s00710-007-0183-7.

894 Poli, S., Schmidt, M.W., 2002. Petrology of Subducted Slabs. Annual Review of Earth and
895 Planetary Sciences 30, 207–235. doi:10.1146/annurev.earth.30.091201.140550.

896 Pöter, B., Gottschalk, M., Heinrich, W., 2004. Experimental determination of the ammonium

partitioning among muscovite, K-feldspar, and aqueous chloride solutions. Lithos 74, 67–90. doi:10.1016/j.lithos.2004.01.002.

Raymond, L.A., 2017. A metasomatic setting, the Russian River Arch, and gravitational emplacement in the history of eclogites at the classic eclogite locality of Jenner, California, USA. International Geology Review 59, 577–598. doi:10.1080/00206814.2016.1213143.

Reinecke, T., 1998. Prograde high- to ultrahigh-pressure metamorphism and exhumation of oceanic sediments at Lago di Cignana, Zermatt-Saas Zone, western Alps. Lithos 42, 147–189. doi:10.1016/S0024-4937(97)00041-8.

Romer, R.L., Meixner, A., Hahne, K., 2014. Lithium and boron isotopic composition of sedimentary rocks — The role of source history and depositional environment: A 250Ma record from the Cadomian orogeny to the Variscan orogeny. Gondwana Research 26, 1093–1110. doi:10.1016/j.gr.2013.08.015.

Rubatto, D., Gebauer, D., Fanning, M., 1998. Jurassic formation and Eocene subduction of the Zermatt–Saas-Fee ophiolites: implications for the geodynamic evolution of the Central and Western Alps. Contributions to Mineralogy and Petrology 132, 269–287. doi:10.1007/s004100050421.

Sadofsky, S.J., Bebout, G.E., 2000. Ammonium partitioning and nitrogen-isotope fractionation among coexisting micas during high-temperature fluid-rock interactions: examples from the New England Appalachians. Geochimica et Cosmochimica Acta 64, 2835–2849. doi:10.1016/S0016-7037(00)00393-8.

Sadofsky, S.J., Bebout, G.E., 2004. Nitrogen geochemistry of subducting sediments: New results from the Izu-Bonin-Mariana margin and insights regarding global nitrogen subduction. Geochemistry, Geophysics, Geosystems 5. doi:10.1029/2003GC000543.

Scambelluri, M., Müntener, O., Ottolini, L., Pettke, T.T., Vannucci, R., 2004. The fate of B, Cl and Li in the subducted oceanic mantle and in the antigorite breakdown fluids. Earth and Planetary Science Letters 222, 217–234. doi:10.1016/j.epsl.2004.02.012.

922 Shannon, R.D., 1976. Revised effective ionic radii and systematic studies of interatomic distances
923 in halides and chalcogenides. Acta Crystallographica Section A: Crystal Physics, Diffraction,
924 Theoretical and General Crystallography 32, 751–767. doi:10.1107/S0567739476001551.

925 Sidey, V., 2016. On the effective ionic radii for ammonium. Acta Crystallographica Section B: Struc-
926 tural Science, Crystal Engineering and Materials 72, 626–633. doi:10.1107/S2052520616008064.

927 Som, S.M., Buick, R., Hagadorn, J.W., Blake, T.S., Perreault, J.M., Harnmeijer, J.P., Catling,
928 D.C., 2016. Earth's air pressure 2.7 billion years ago constrained to less than half of modern
929 levels. Nature Geoscience 9, 448–451. doi:10.1038/ngeo2713.

930 Som, S.M., Catling, D.C., Harnmeijer, J.P., Polivka, P.M., Buick, R., 2012. Air density 2.7 billion
931 years ago limited to less than twice modern levels by fossil raindrop imprints. Nature 484, 359–
932 362. doi:10.1038/nature10890.

933 Sorensen, Grossman, J.N., Perfit, M.R., 1997. Phengite-hosted LILE Enrichment in Eclogite and
934 Related Rocks: Implications for Fluid-Mediated Mass Transfer in Subduction Zones and Arc
935 Magma Genesis. Journal of Petrology 38, 3–34. doi:10.1093/petroj/38.1.3.

936 Spandler, C., Pettke, T., Hermann, J., 2014. Experimental study of trace element release during
937 ultrahigh-pressure serpentinite dehydration. Earth and Planetary Science Letters 391, 296–306.
938 doi:10.1016/j.epsl.2014.02.010.

939 Ulmer, P., Trommsdorff, V., 1995. Serpentine Stability to Mantle Depths and Subduction-Related
940 Magmatism. Science 268, 858–861. doi:10.1126/science.268.5212.858.

941 Urann, B.M., Roux, V.L., John, T., Beaudoin, G.M., Barnes, J.D., 2020. The distribution and abun-
942 dance of halogens in eclogites: An in situ SIMS perspective of the Raspas Complex (Ecuador).
943 American Mineralogist 105, 307–318. doi:10.2138/am-2020-6994.

944 Vils, F., Pelletier, L., Kalt, A., Müntener, O., Ludwig, T., 2008. The Lithium, Boron and Beryllium
945 content of serpentinized peridotites from ODP Leg 209 (Sites 1272A and 1274A): Implications

946 for lithium and boron budgets of oceanic lithosphere. Geochimica et Cosmochimica Acta 72,
947 5475–5504. doi:10.1016/j.gca.2008.08.005.

948 White, R.W., Powell, R., Holland, T.J.B., Johnson, T.E., Green, E.C.R., 2014. New mineral
949 activity–composition relations for thermodynamic calculations in metapelitic systems. Journal
950 of Metamorphic Geology 32, 261–286. doi:10.1111/jmg.12071.

951 Wordsworth, R.D., 2016. Atmospheric nitrogen evolution on Earth and Venus. Earth and Planetary
952 Science Letters 447, 103–111. doi:10.1016/j.epsl.2016.04.002.

List of Figures

1 Sample photomicrographs and BSE images 41
2 SIMS calibration of N contents 42
3 Major and trace element data 43
4 B-N data 44
5 Bulk K_2O and N contents 45
6 N-K-Na data for chlorite 46
7 Fluid rock interaction modelling of phengite N-B-Li data from garnet-phengite quartzite (LC-3) 47
8 Equilibrium phase diagrams for sample SEC16-1 48

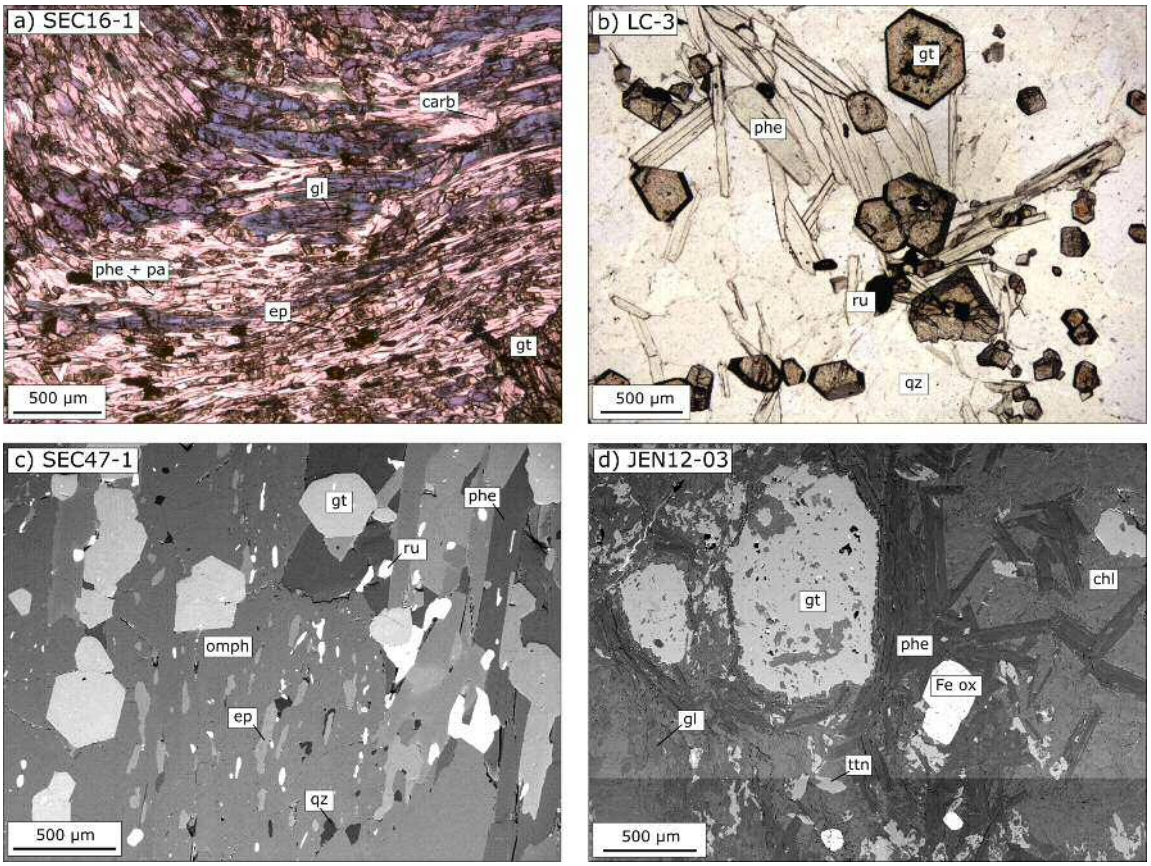

Figure 1: (a) Representative photomicrograph in plane polarised light of blueschist SEC16-1. (b) Representative photomicrograph in plane polarised light of garnet-phengite quartzite LC-3. (c) Representative back scattered electron image of eclogite SEC47-1. (d) Representative back scattered electron image of blueschist JEN12-03. Phe = phengite, pa= paragonite, gt = garnet, gl = glaucophane, ep = epidote, qz = quartz, ttn = titanite, chl = chlorite, omph = omphacite, Fe ox = iron oxide.

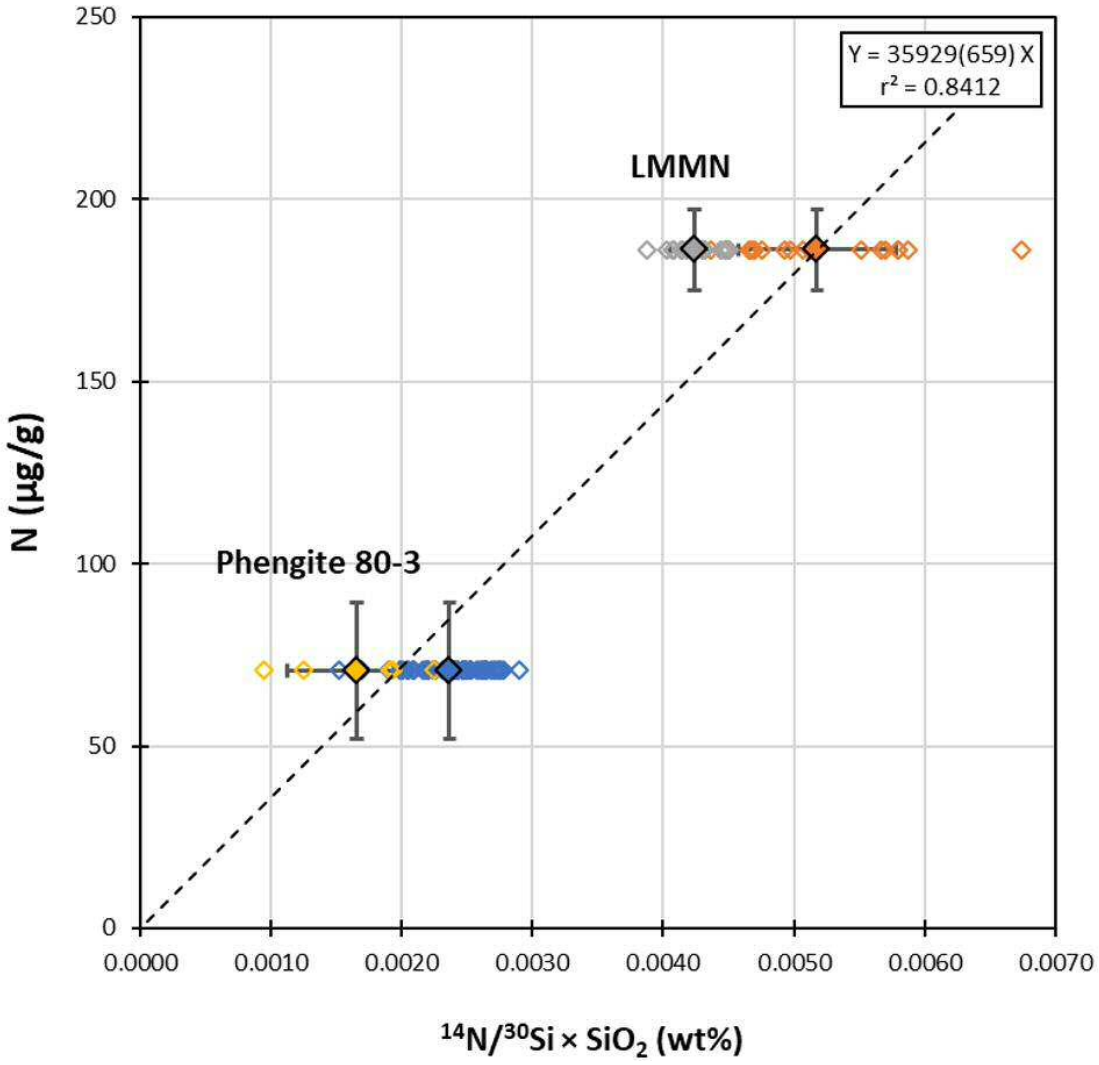

Figure 2: SIMS calibration of N concentrations based on two white mica standards (Phe80-3 and LMMN Busigny et al. (2003b, 2004)). All indiviudal analytical spots (n=70) are indicated as well as averages with 1s uncertainties. The slope of the calibration slope is indicated, along with the 1s uncertainty in brackets.

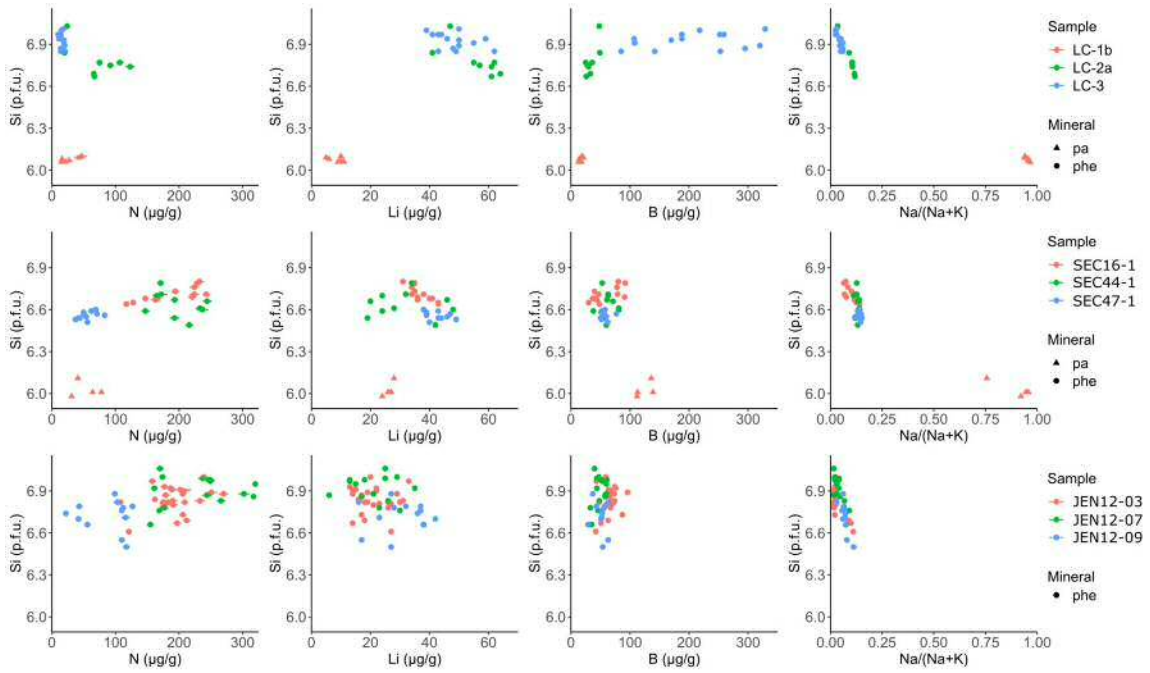

Figure 3: N, Li, B, Na/Na+K data vs Si p.f.u. for phengite and paragonite from each locality (top: Cignana, middle Raspas, bottom Jenner). 1s error bars are plotted. Where error bars are not shown, they are smaller than the size of the symbol.

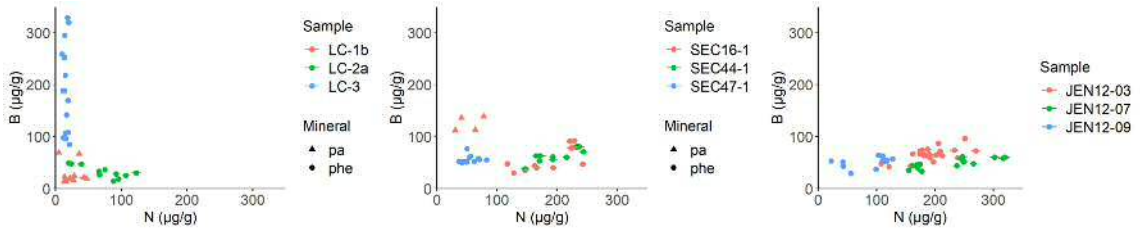

Figure 4: N vs B for phengite and paragonite from each locality (left: Cignana, middle Raspas, right Jenner). 1s error bars are plotted. Where error bars are not shown they are smaller than the size of the symbol.

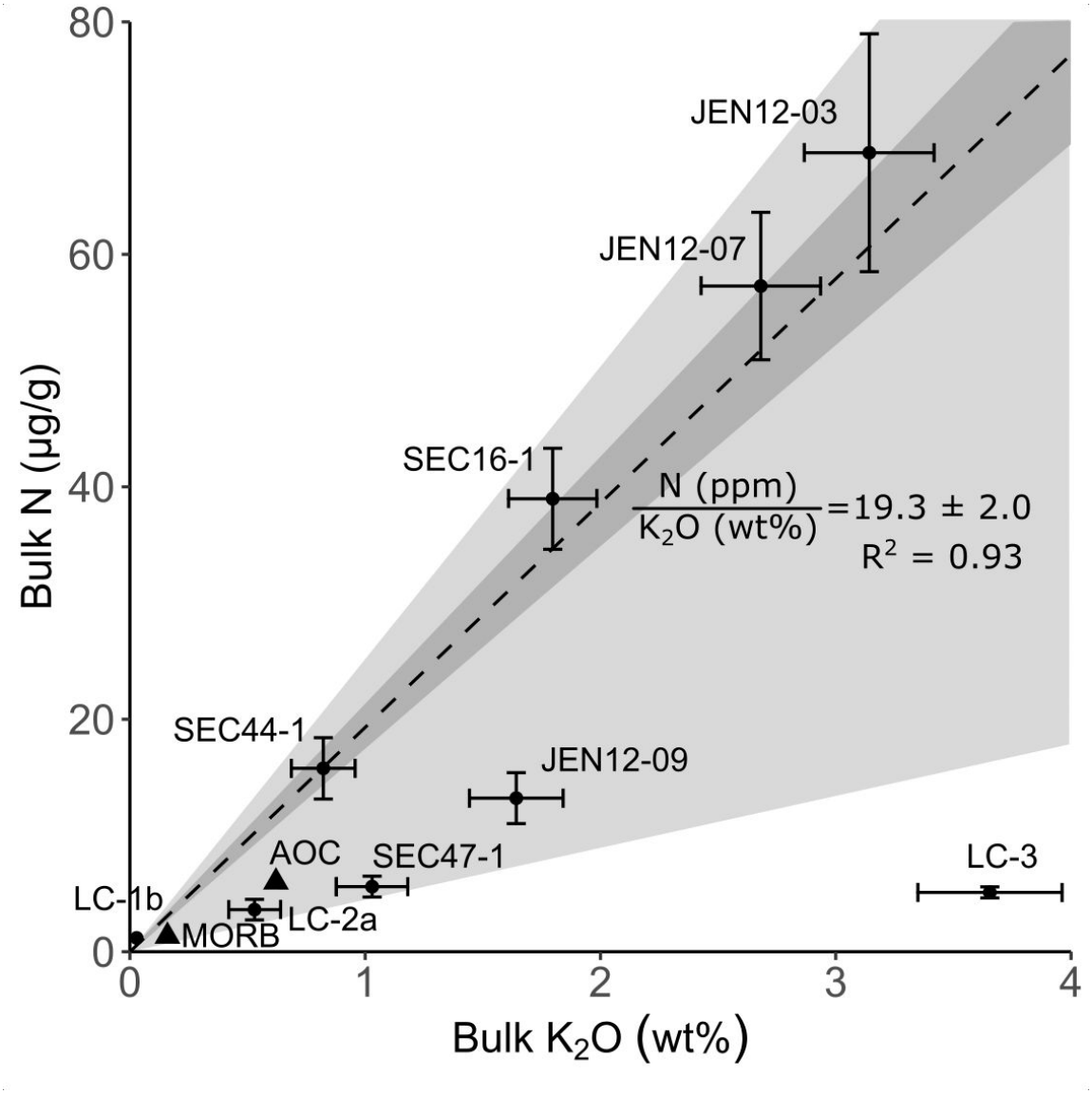

Figure 5: Calculated bulk K_2O and N contents for each sample. Average values for MORB and AOC (black triangles) are shown for comparison (Johnson and Goldblatt, 2015; Gale et al., 2013; Kelley et al., 2018). The average N/K_2O (excluding sample LC-3) is plotted as a dashed line with 1s uncertainty (dark grey). Upper and lower bounds are plotted in light grey.

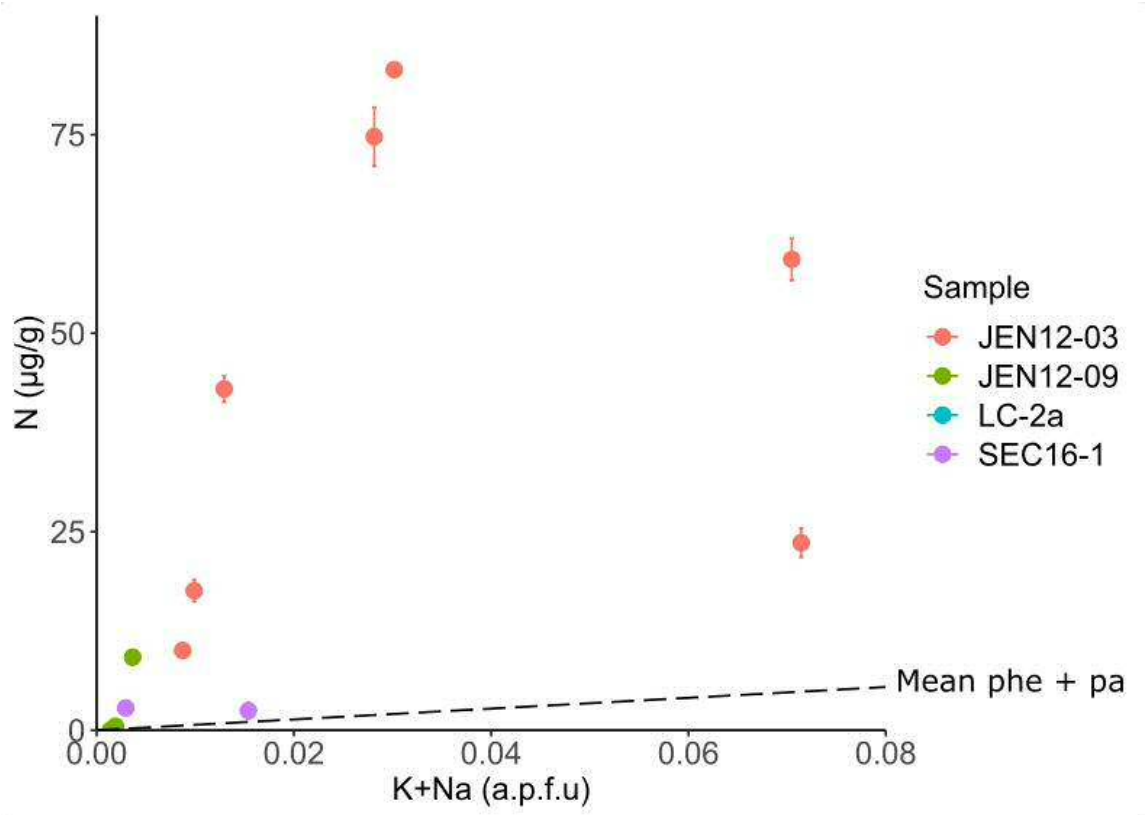

Figure 6: N versus K+Na plot for chlorite. Chlorites from sample JEN12-03 occur in the matrix alongside phengite, and have elevated K+Na and N contents. Chlorites from other samples occur as rims on garnets and contain little N, K or Na. A line showing the mean value for N/(K+Na) in phengite and paragonite is shown for comparison.

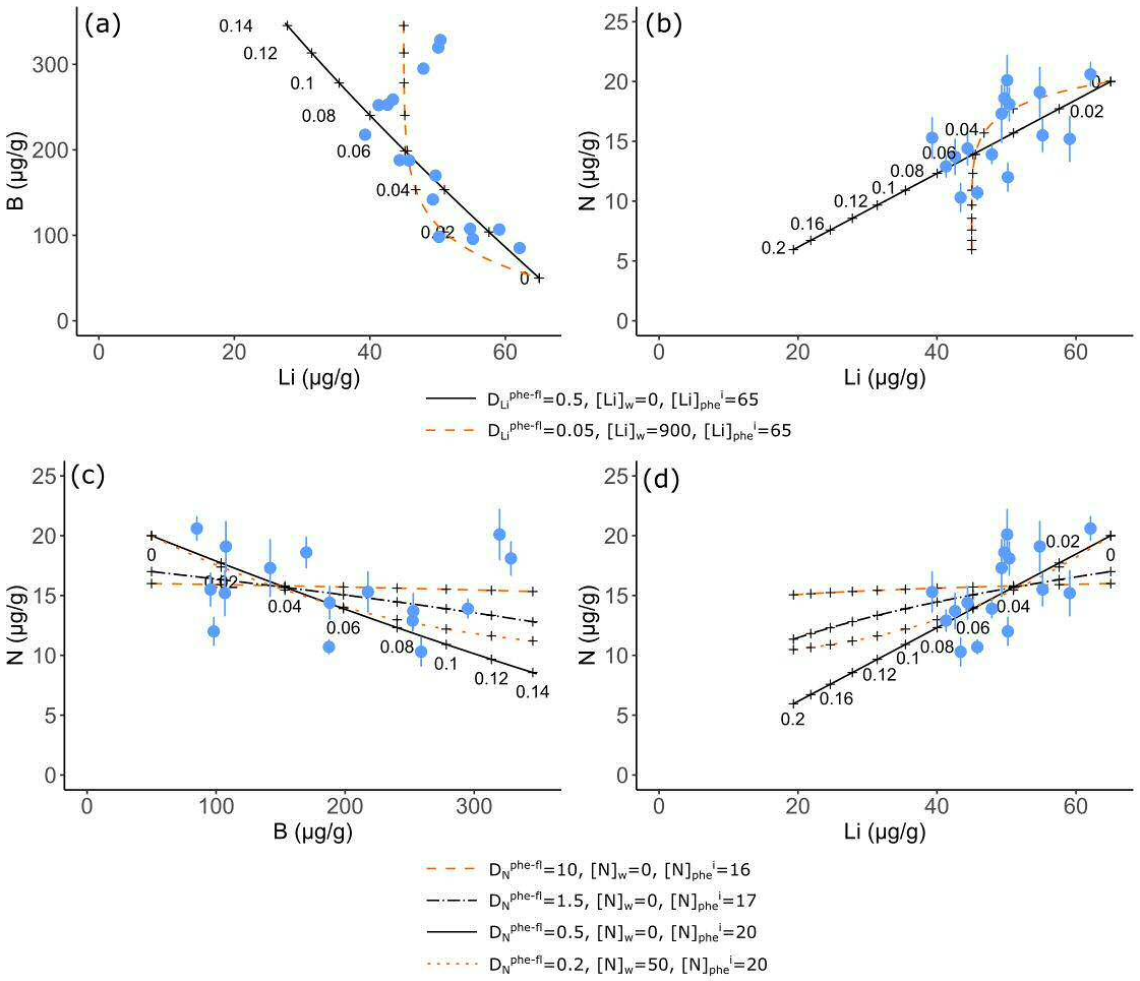

Figure 7: Fluid rock interaction modelling of phengite N-B-Li data from garnet-phengite quartzite (LC-3). Blue points are the measured data, and black lines show model outcomes for a range of different input parameters. 1s error bars are shown for N data. Error bars for B and Li are smaller than the size of the symbols. Boron input parameters were constrained from previous work (Halama et al., 2020). The top panel (a,b) shows two end member scenarios for Li modelling. The bottom panel (c,d) shows endmember scenarios for N modelling ($D_N = 10$ and $D_N = 0.2$) and two intermediate scenarios. See text for detailed explanation of modelling parameters (section 5.2).

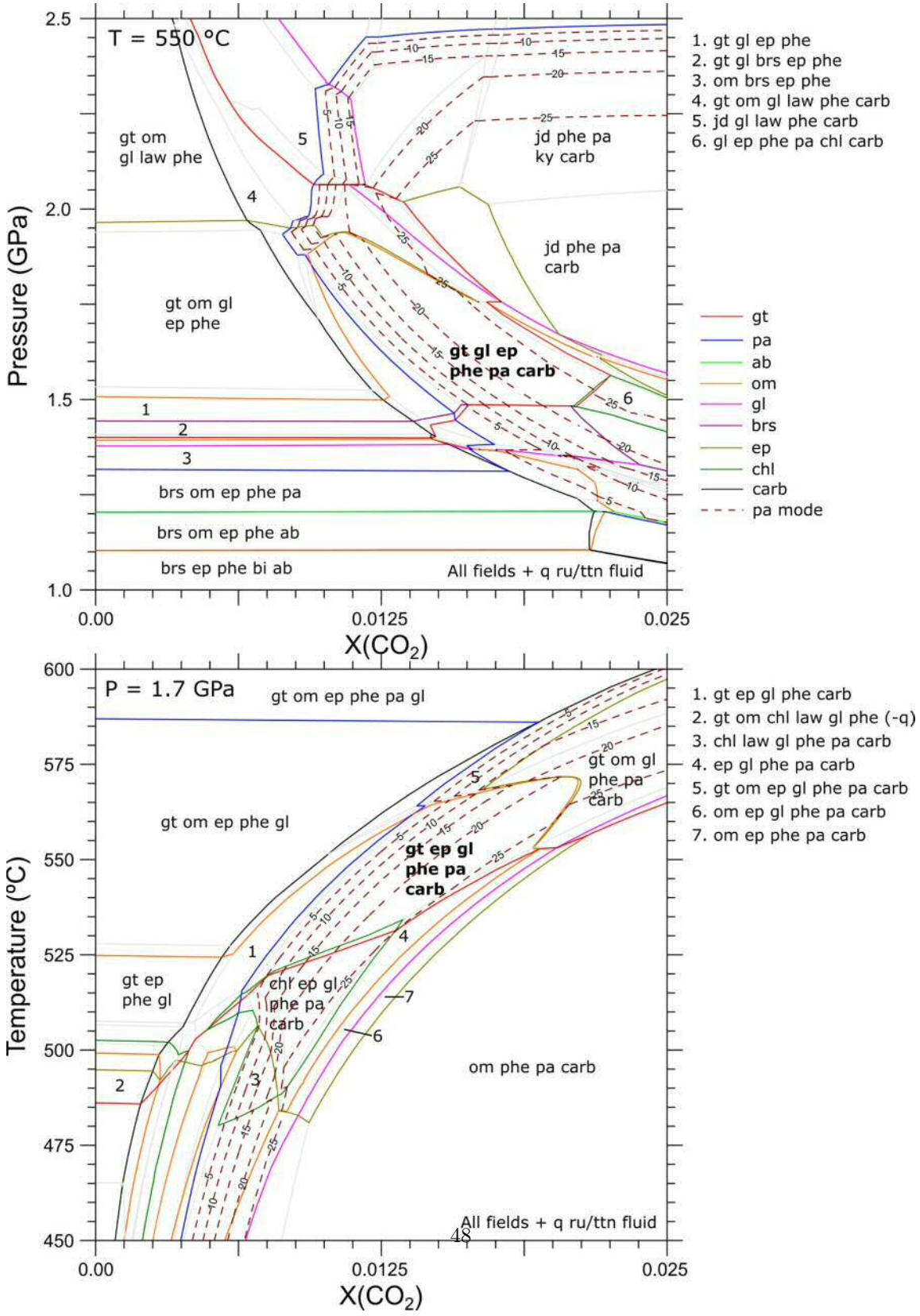

Figure 8: P-X(CO_2) and T-X(CO_2) equilibrium phase diagrams for sample SEC16-1. The observed assemblage is indicated in bold font. Gt = garnet, om = omphacite, jd = jadeite, gl = glaucophane (*sensu lato*), barroisite (*s.l.*), ep = epidote, phe = phengite, pa = paragonite, chl = chlorite, carb = carbonate, ab = albite, bi = biotite, law = lawsonite, ru = rutile, ttn = titanite.

List of Tables

1 Mineral modes and N concentrations, and calculated bulk N concentrations 50
2 Inter-mineral partition coefficients for Li, B and N 51
3 Experimental N partitioning data 52

Sample	LC-3	LC-2a	LC-1b	SEC16-1	SEC44-1
Lithology	Gt-phe quartzite	Metagabbro	Eclogite	Blueschist	Eclogite
Phe mode (vol%)	33	5		16	8
Phe N (µg/g)	10–21 (16)	20–123 (72)		117–243 (190)	147–234 (203)
Pa mode			5	16	
Pa N			5.5–47 (24)	31–78 (54)	
Chl mode		<1		<1	
Chl N		1.2–4.9 (3.6)		1.0–2.8 (2.1)	
Calculated bulk N	5.1	3.6	1.2	39	16
1s	±0.5	±0.9	±0.3	±4	±3
Measured bulk N				46	10
Sample	SEC47-1	JEN12-03	JEN12-07	JEN12-09	
Lithology	Eclogite	Blueschist	Blueschist	Eclogite	
Phe mode (vol%)	10	30	25	15	
Phe N (µg/g)	37–118 (61)	108–270 (193)	155–320 (229)	22–127 (88)	
Pa mode					
Pa N					
Chl mode		30		<1	
Chl N		10–83 (45)		0.0–9.2 (2.9)	
Calculated bulk N	5.6	71	57	13	
1s	±0.9	±10	±6	±2	
Measured bulk N	7.2				

Table 1: Mineral modes and N concentrations, and calculated bulk N contents for the nine samples in this study. N contents are given as a range followed by the mean in brackets. Three samples have measured bulk N contents (Halama et al., 2010), which are consistent with the calculated results. The procedure for calculating 1s uncertainties is described in Section 4.3 and the full data set is provided in the electronic supplement.

	Li	B	N	n
SEC44-1				
Phe	19–48 (32)	38–81 (63)	147–244 (197)	10
Cpx	94–110 (104)	2.3–3.3 (2.9)	1.8–3.0 (2.4)	4
$D^{phe/cpx}$	0.31	22	81	
SEC47-1				
Phe	38–83 (46)	50–100 (61)	37–118 (61)	11
Cpx	142	3.0	3.0	1
Ep			1–2 (1.1)	2
$D^{phe/cpx}$	0.32	18	22	
$D^{phe/ep}$			55	
SEC16-1				
Phe	31–46 (37)	30–92 (59)	117–243 (190)	14
Pa	24–28 (26)	93–139 (119)	31–118 (66)	4
Gl	132–169 (151)	3.9–4.9 (4.4)	3.9–4.4 (4.1)	2
$D^{phe/pa}$	1.5	0.49	2.9	
$D^{phe/gl}$	0.25	13	46	
JEN12-09				
Phe	16–42 (30)	29–64 (51)	22–127 (88)	12
Cpx	46–55 (51)	1.2–1.3 (1.3)	1.5–1.9 (1.7)	2
$D^{phe/cpx}$	0.60	41	52	

Table 2: Inter-mineral partition coefficients for Li, B and N. Mineral compositions are given in µg/g as a range with a mean value in brackets. The number of analyses (n) is also listed. Partition coefficients are calculated from the mean values.

	P (GPa)	T (°C)	$D^{\text{phe}-\text{fl}}$	$D^{\text{bi}-\text{fl}}$	$D^{\text{bi}-\text{phe}}$
Förster et al. (2019)	2	750	10		
Förster et al. (2019) *	3	800–1000	0.5–1.1	0.2–1.6	1.5–3.1
Pöter et al. (2004)	0.4	400–600	0.12–0.15		3.5
Pöter et al. (2004)	1.5	400–600	0.19–0.20		
Jackson et al. (2021) *	0.2–2.3	725–925		0.01–0.4	
Moine et al. (1994)	0.2	550		~0.5	
Honma and Itihara (1981) **	~ 0.4	~ 700			1.5–3.1
Duit et al. (1986) **	~ 0.5	500–700			2.2–4.2
Busigny et al. (2004) **					2.6–3.3

Table 3: Summary of available partitioning data for nitrogen between aqueous fluid and micas (phengite and biotite). Most data are from subsolidus experiments but data indicated with a * are from suprasolidus experiments. Some natural data on biotite-phengite partitioning are also included (**).

Figure 2

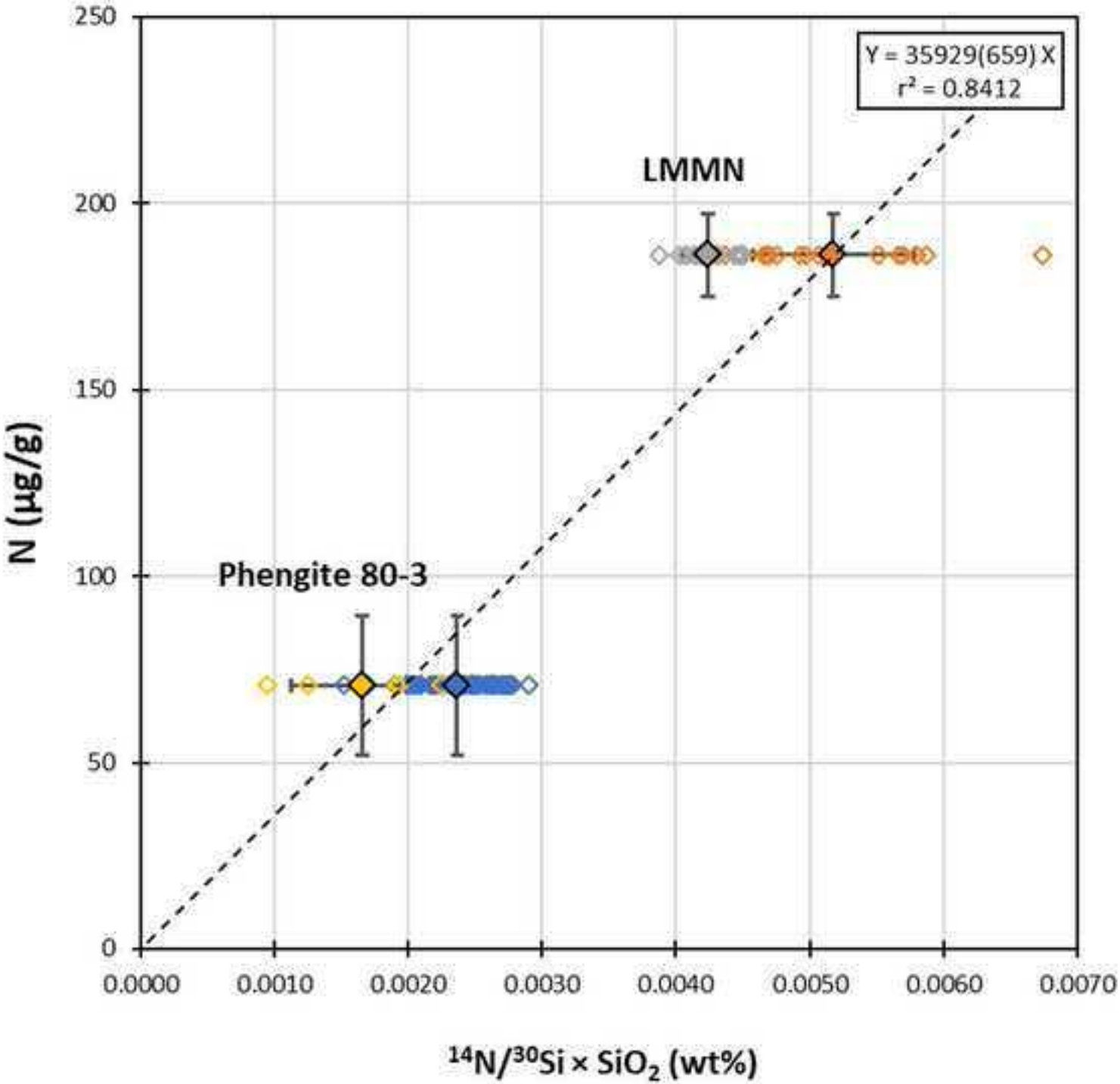

Figure 3

Click here to access/download;Figure;Fig3.jpg

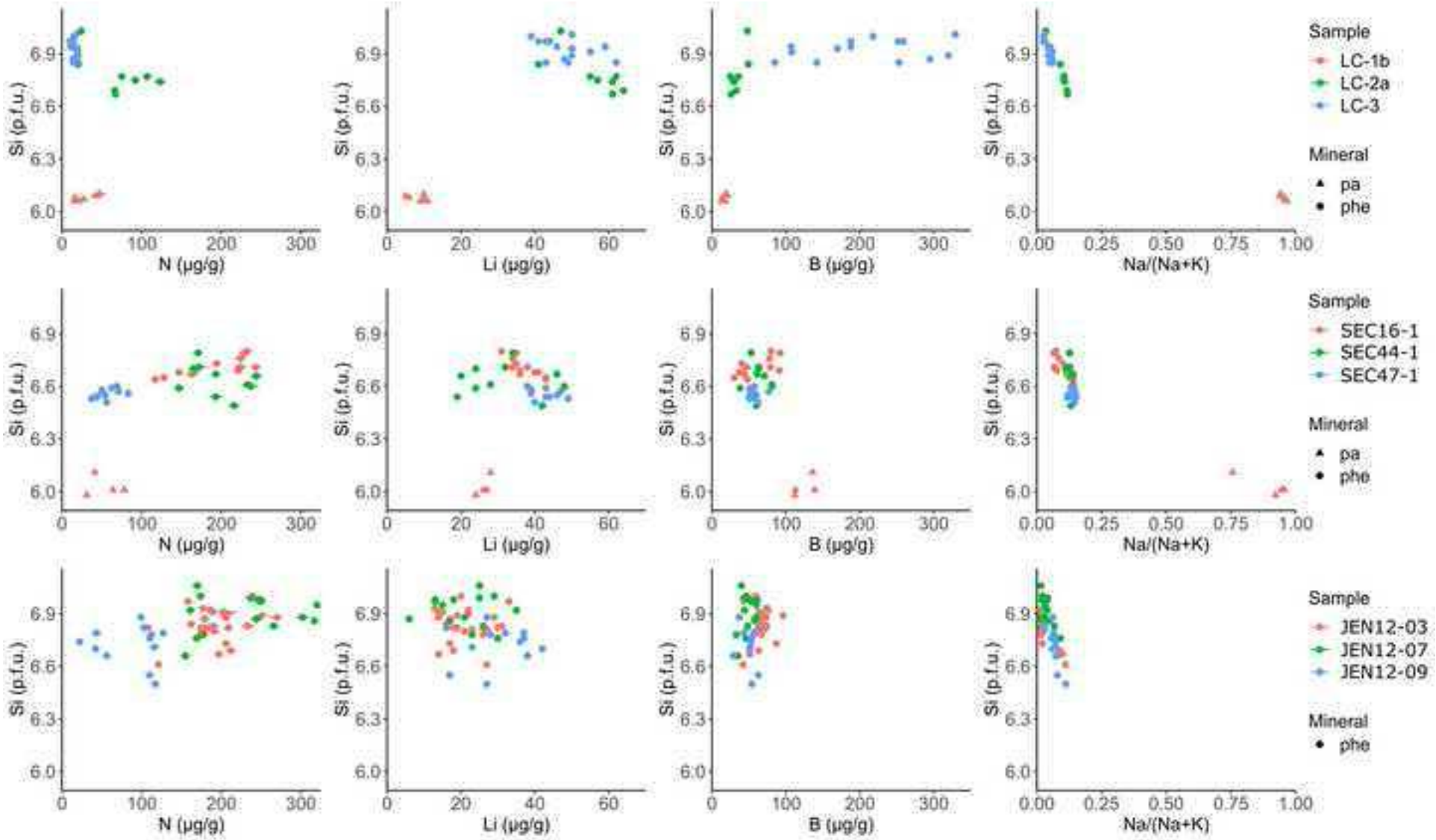

Figure 1

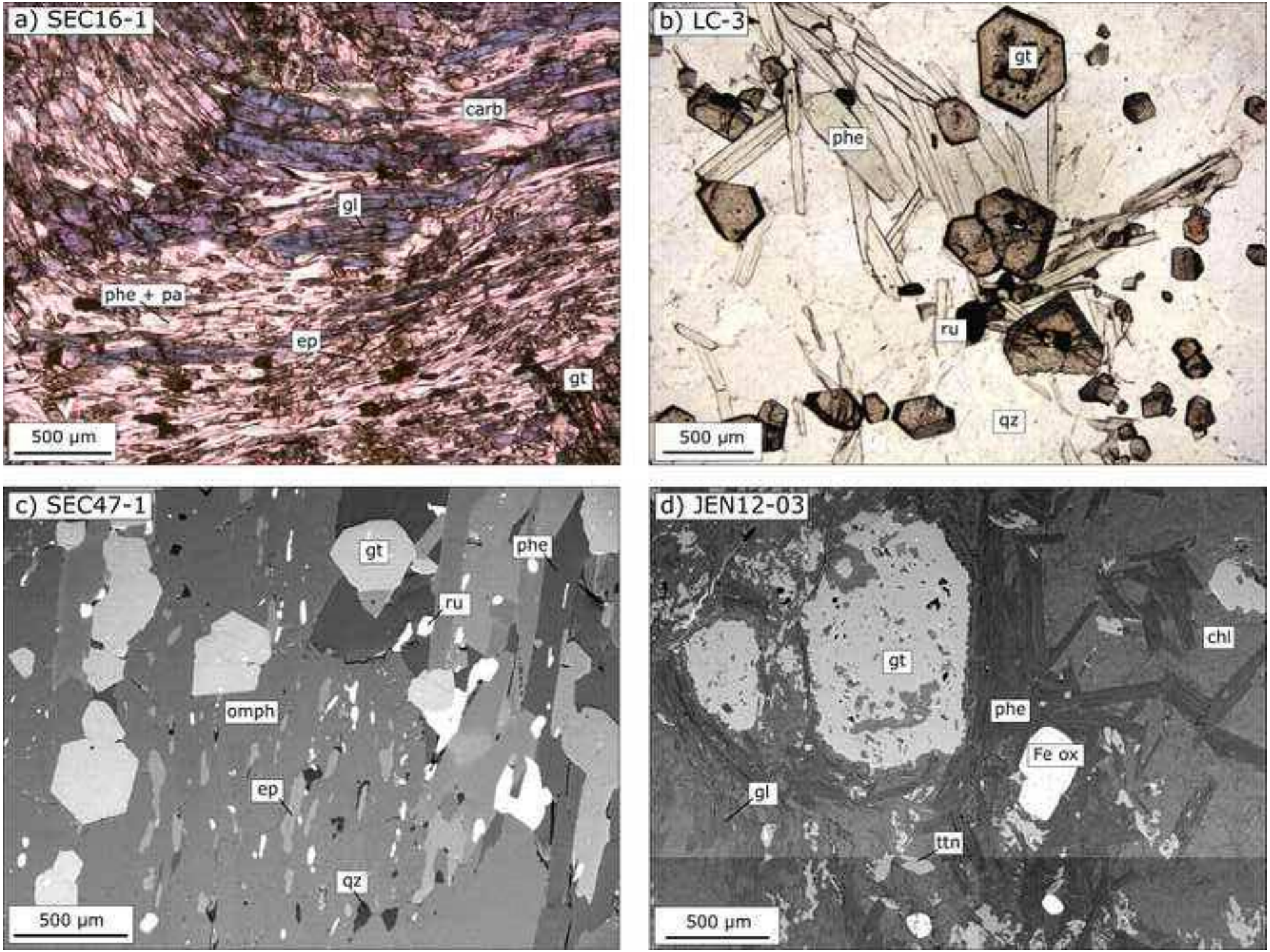

Figure 5

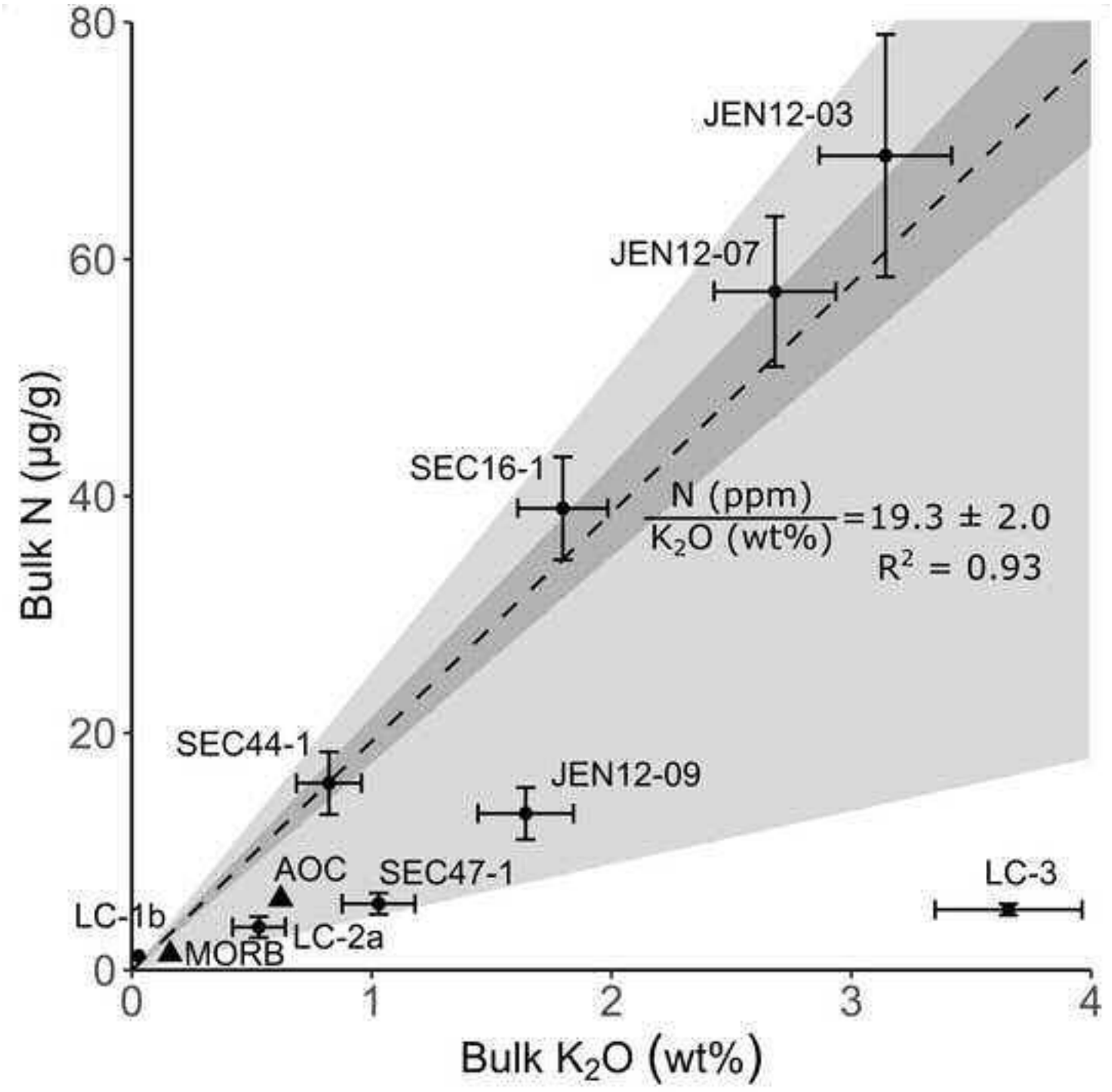

Figure 6

Click here to access/download;Figure;Fig6.jpg

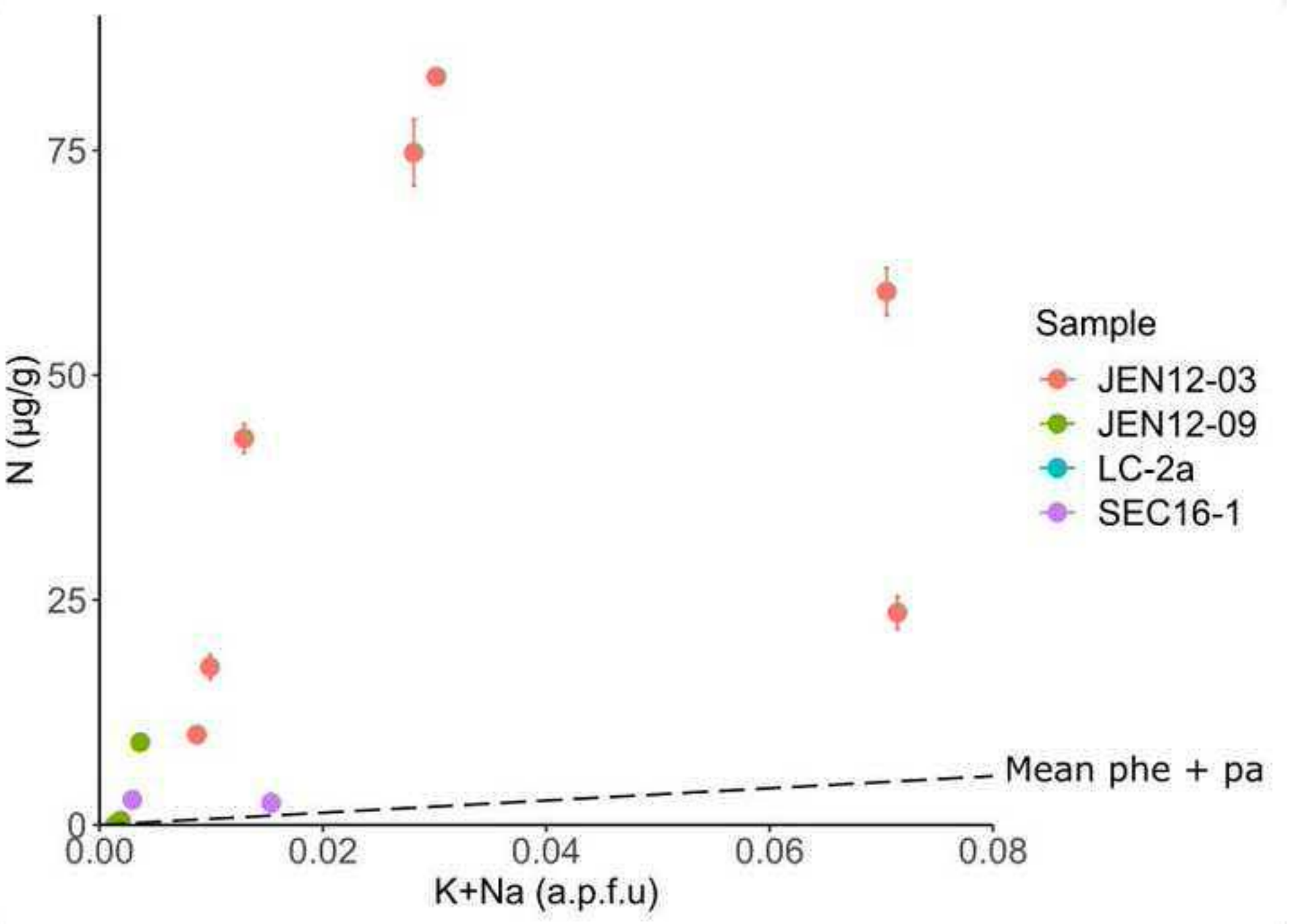

Figure 8

Click here to access/download;Figure;Fig8.jpg

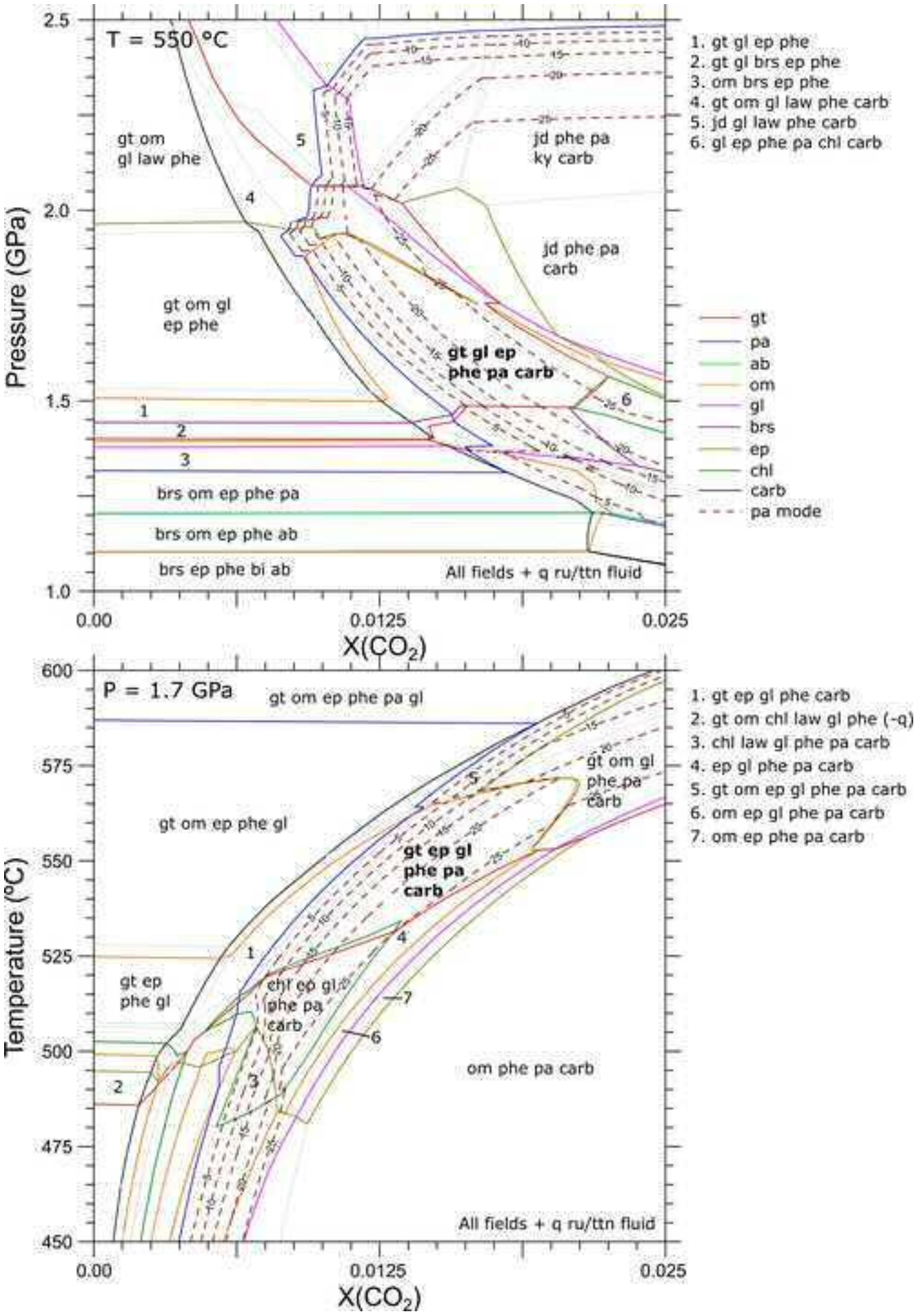

Figure 4

Click here to access/download;Figure;Fig4.jpg

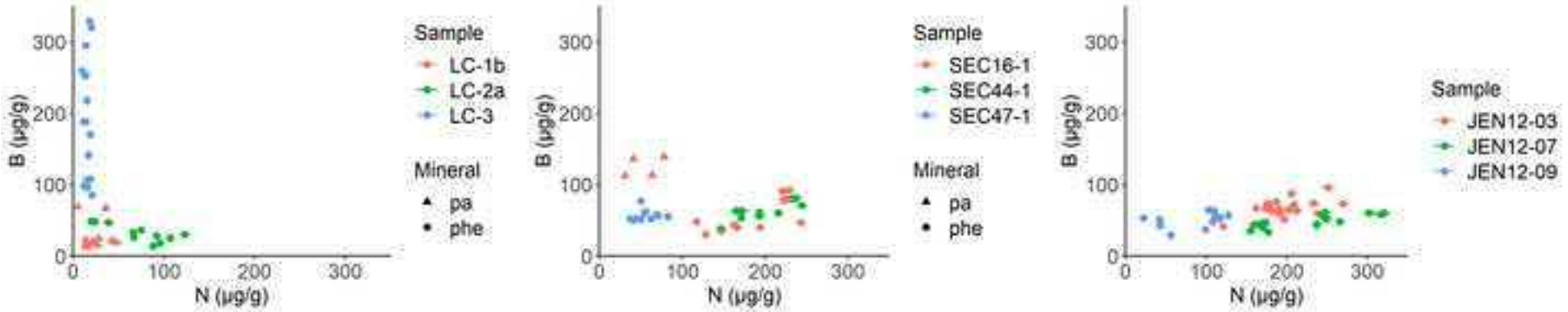

Figure 7

Click here to access/download;Figure;Fig7.jpg